TABLE OF CONTENTS

ABBREVIATIONS

Fe	Iron
Co	Cobalt
Ni	Nickel
Au	Gold
BE	Binding Energy
Cu	Copper
CVD	Chemical vapour deposition
d	Diameter of 1-D material
D	Diameter of nanoparticle
HRTEM	High resolution transmission electron microscope
1-D	One-dimensional
OMBE	Organic molecular beam epitaxy
l	Length of 1-D material
L	Lateral spacing between nanoparticles
PS	Polystyrene
P2VP	Poly-2-Vinyl-Pyridine
sccm	standard cubic centimetres per minute
SEM	Scanning electron microscope
Si	Silicon
SiO_x	Silicon oxide
SiNW	Silicon nanowire
SiNT	Silicon nanotube
T*	Critical temperature at which growth ceases
TEM	Transmission electron microscope
TDS	Thermal desorption spectroscopy
UPS	Ultraviolet photoelectron spectroscopy
XPS	X-ray photoelectron spectroscopy
W	Kinetic energy
XRD	X-ray diffraction
Zn	Zinc

1 Introduction

1.1 Motivation

The evolution of nanotechnology has led to the improvement of device performance based on the unique properties materials such as nanoparticles, quantum dots, nanowires and nanotubes manifest as thier dimensions deminish [1-6]. Silicon (Si) has been well credited for in its role as the fundamental component in integrated circuits and consequently in the microelectronic revolution over the last century. Knowledge on its properties is well established and its electronic properties can by modified via doping processes [7]. This has fascilitated the engeneering of Si properties.

One interesting manifestation, of Si one-dimensional materials (1-D), is the transition of the band structure from an inderect to a direct band gap at critical diameters of ~ 20 nm. This phenomenon, has led to the establishment of a Si laser [8]. Alongside its attractive optoelectronic properties, Si has shown to posses potential applicability in field emission [9], solar cells [10] and as a biomaterial, due to its noncytotoxic nature [11].

In order to exploit these properties, a great deal of effort has been invested by researchers to synthesise Si nanoscale materials such as silicon nanowires and nanotubes. Several approaches to readily synthesisze Si 1-D materials have included catalyst-free and catalyst-mediated routes with silicon precursor materials in solution [12, 13] as well as in the vapour phase [14, 15]. Despite encouraging advances, some common problems still prevail:

- Selective synthesis of Si 1-D materials at low temperatures ($T < 400°C$) still proves challenging. Even though reasonably low temperature Si 1-D synthesis has been achieved through plasma enhanced chemical vapour deposition (PECVD), the side deposition of source material is not efficently controlled [16]. Hence, the process is not selective enough.

- Appropriate control over Si 1-D diameter tuning is still lacking. Catalyst-free synthesis of Si 1-D structures enables the study Si 1-D material intrinsic properties [17]. However, this technique usually falls short of adequate control over Si 1-D structure diameter. For this reason, catalyst-mediated routes are taken as an alternative in order to dictate Si 1-D material size from the nanoparticles [18]. The problem usually encountered with catalyst-mediated Si 1-D growth is that the growth process is very much dependent on the thermal properties of the nanoparticle catalyst, as well as the substrate on which the nanoparticles are placed.
- Appropriate control over seed layer (catalyst nanoparticles) properties is lacking. The synthesis of Si 1-D structures typically occurs via breakdown of thin films (e.g. gold) by the aid of annealing processes in order to obtain droplets, which in turn catalytically promote seed growth [14]. These annealing steps involve high temperatures, which render the growth process uneconomical. Also, the annealing of thin films results in a broad size distribution of nanoparticles, hence size control is lost. For this reason, the transfer of this technology from expensive crystalline, to cheap amorphous substrates such as glass remains problematic. Alternative routes are therefore being sought to make Si 1-D synthesis cheaper. In this light, McAlpine *et al.* illustrated the intergration of Si 1-D structures, initially grown at high temperatures on crystalline substrates onto glass and plastic substrates through a solution-based assembly technique [19, 20]. This approach unfortunately, does not provide a remedy for applications such as field emission, which demand vertically, aligned Si 1-D structures. Even though Si 1-D structures have been integrated onto glass and plastic substrates, the issue of selective Si 1-D low synthesis temperatures remains unsettled.

A remedy to the situation is to use nanoparticles whose thermal properties differ from those of the bulk material of the same element. This way, annealing steps can be discarded. It is known that the melting point of gold (Au) nanoparticles decreases as the nanoparticles become smaller [21, 22]. This implies, working with small Au nanoparticles can lower synthesis temperatures considerably. In addition, the catalytic properties of Au nanoparticles are enhanced on oxide substrates [23]. This is contrary to the situation with bulk

Au films which show less catalytic activity (with respect to Si 1-D growth) on oxide surfaces. However, if nanoparticles are not well anchored on a substrate, their migration on the surface during the growth process could lead to Ostwald ripening and a subsequent alteration in their size [24]. Hence, a proper lithographic technique must be chosen, which is capable of producing small size nanoparticle structures, which are mechanically stable on a surface (i.e. do not migrate) and last but not least, inexpensive.

A crucial factor in the fabrication of functional nanostructures is the defined placement and connection of nanometre-sized objects in periodic or aperiodic arrangements on surfaces with, different chemical composition, electrical and optical properties. Periodic and aperiodic microstructures are prepared by lithographic techniques which include photolithography and electron-beam (é-beam) lithography and are the most frequently used techniques for structuring substrates. Variations of these techniques, such as the use of short wavelength light sources, e.g. deep UV or X-ray, and chemical modification of polymer resistive materials allow researchers to reduce structure dimensions to a sub-micrometre scale [25, 26]. Structures as small as a few nanometres are produced nowadays by é-beam lithography and with photolithography down to 50 nm. Photo lithography is usually applied to insulating substrates such as glass. However, the cost of apparatus is considerably high if one aims for 50 nm resolution. É-beam lithography offers the magnitude of structure required (< 50 nm), but it is a it time-costly, expensive, and usually limited to small surface areas and conductive substrates such as silicon wafers. There however exist a few illustrations of é-beam lithography applied to insulating substrates [27-30]. Other lithographic techniques include micro-contact printing, which is capable of structuring solid substrate interfaces with resolutions down to 50 nm. Smaller dimensions are harder to achieve because the contact stability of the stamp with the substratehas to be controlled [31].

The use of macromolecules or structures associated from macromolecules are of special interest in this respect since these allow for bridging the length scale between a few and 200 nm, which link nanostructures to structure sizes available from photo- or e-beam lithography. Self-assembly of block copolymers or mixtures of homopolymers form complex surface structures with nanoscale features. The self-assembled pattern depends on enthalpic and steric interactions between polymer chains, as well as on the interactions of the polymer chains with the solid interface [32-36]. These interactions are tunable by molecular parameters, which makes it a valuable tool for surface patterning.

Pure self-assembly techniques provide some means to control feature size, to orders as low as a few nanometres and are practically applicable since the resulting structures are pre-programmed in the molecular structure or colloidal properties. In principle, this technique allows for immense flexibility in terms of the architecture of atom assembly and resulting functionalities. The feature sizes range between 1 and 50 nm. However, self assembly may not cover requirements regarding aperiodic structures or dimensions that exceed 50 nm in terms of feature size and separation distance [37-39]. To overcome such hurdles, two different length scales are matched i.e., the pattern from self assembly of block copolymer micelles (< 100nm) and é-beam writing (> 50 nm). This allows very small numbers of nanometer-sized nanoparticles to be grouped in even aperiodic arrangements [40]. Also, these groups can be separated by length scales that are not accessible by pure self-assembly techniques.

The success of this technique in improving surface functionality has been extensively illustrated in previous studies [41]. The nanoparticles prepared by micelle nanolithography have also proven to be well anchored to substrates, giving them reasonably good mechanical stability. This factor has been exploited in force measurements performed on substrates patterned with Au nanoparticles prepared by micelle nanolithography [42].

Micelle nanolithography is an inexpensive technique, capable of preparing well defined small diameter nanoparticles in a quasi hexagonal manner which, are anchored to the underlying substrate [43]. In addition, this technique is applicable to large surface areas and is not constrained by the curvature of the surface used [44]. These are the preliminary conditions nanoparticles should fulfil as building blocks for a Si 1-D growth process.

1.2 Objective

This work aims at tunning the properties of Au nanoparticles in order to achieve low temperature growth. Also, nanoparticle/ substrate interactions are to be exploited to tune Si 1-D material structure via substrate induced stress which is expected to influence diffusion processes at the nanoparticle.

Since nanoparticle size plays a great role in controlling the diameter and subsequent properties of a Si 1-D structure, adequate size control must be achieved. In this work, the micelle nanolithography technique is used to obtain substrate-anchored nanoparticles with controlled size and local site density on Si, SiOx/Si and borosilicate glass substrates. By this, nanoparticle migration is inhibited due to substrate anchorage and good control over Si 1-D material diameter is achieved.

The performance of a material very much relies on the synthetic route chosen to develop it. Therefore, the enhancement of the catalytic properties of Au nanoparticles is necessary. For this, a directed administration of impurity via nanoparticle treatment in different plasma atmospheres is achieved. This is analogous to the doping mechanism used to alter the properties of materials such as semiconductors. The consequence of the nanoparticle doping process is an enhancement in Au nanoparticle activity, which enables Si 1-D growth at temperatures as low as 320°C.

Strong nanoparticle –substrate interaction is exploited to control the structure of Si 1-D materials. This idea is based on the presence of a substrate-induced stress due to lattice mismatch between the nanoparticle and the substrate. Also differences in thermal expansivity of the substrate material and nanoparticle lead to enhanced stress effects which influence diffusion processes at the Au nanoparticle site. This subsequently determines whether a Si nanowire or nanotube is grown.

2 Physical Background of Experimental Basics

This chapter gives an overview on certain basic properties (physical and chemical), of the materials studied in this work and how these properties vary with size miniature. Furthermore, fundamentals on the physical background of the techniques implemented are discussed.

2.1 The different 'Faces' of a Material

Graphite and diamond are different allotropic forms of carbon (C) with distinctive structures and bonding characteristics. Consequently, they grossly differ in chemical and physical properties. Last century, nanomaterials such as fullerenes (C_{60}, C_{70}, etc) and carbon nanotubes (CNTs - regarded as rolled up graphene sheets cylindrical in shape with single- or multiple walls) - were discovered and added to the family of carbon allotropes. These in themselves also demonstrate amazing properties [45], which strikingly differ from those known so far on graphite and diamond even though they stem from the same element.

All this in itself implies that one can not confidently claim complete knowledge of the properties of an element or material. In other words, a material such as gold, is not necessarily gold, nor is silicon necessarily silicon as we so far know it to be. This is because the bonding in a small metal or semiconductor cluster differs from that in the bulk. Also, an atom at the surface of a chunk of material is different from an atom of the same element inside the chunk. Likewise, is an atom at the smooth surface of a reasonably sized single crystal different from an atom at the surface of a small cluster of the same element. Not to be neglected, are the effects imposed by the material(s) present in the vicinity of a small cluster e.g. the support beneath or around the nanoparticle or a few atoms of an alien element which dope the cluster. It is only during the last few decades of the 21st century, that experimental methods became available to enable the synthesis of nanomaterials in a controlled and reproducible manner in order to facilitate the direct observation of individual clusters and probe their properties.

2.2 Basic Properties of Gold & Silicon

2.2.1 Gold (Au)

Gold (Au) has an atomic number of 79 i.e. each gold atom has 79 protons in its nucleus. The atomic mass of the gold atom is 196.967 and the atomic radius is 0.1442 nm. The arrangement of outer electrons around the gold nucleus is based on 14 4*f* shell electrons, 10 5*d* shell electrons and a single 6*s* shell electron (electronic configuration: [Xe] $4f^{14}$ $5d^{10}$ $6s^{1}$). The arrangement of these electrons is related to gold's characteristic yellow colour. The colour of a metal is based on transitions of electrons between energy bands. The conditions for the intense absorption of light at the wavelengths necessary to produce the typical gold colour are fulfilled by a transition from the *d* band to unoccupied positions in the conduction band.

Au is known to be the most noble of all metals with a face centered cubic structure (figure 2.2-1). It is the least reactive metal towards atoms or molecules at the interface in a gas or liquid phase. Its inertness as concerns reactivity with molecules such as H_2 and O_2 has been attributed to repulsion between the orbitals of the adsorbate and the filled *d* states of Au [46].

However, the inert nature of Au does not reflect a general inability to form chemical bonds. Au forms very stable alloys with several other metals. The melting point of pure Au is 1064°C, although when alloyed with other elements such as silver or copper the gold alloy will melt over a range of temperatures.

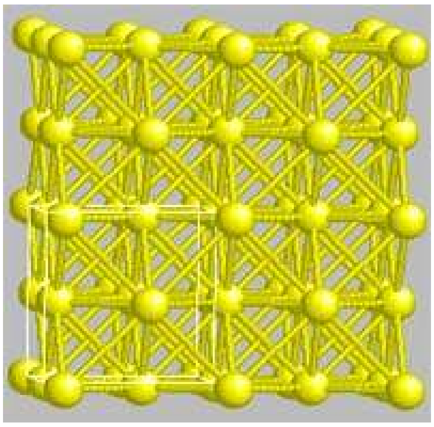

Figure 2.2-1: Crystal structure [47] of Au is cubic close-packed. The structure is a cube with an additional atom in the middle of each cube face. Each gold atom has 12 nearest neighbours. Alternatively, the structure can be thought of as stacking layers of close-packed spheres.

2.2.2 Silicon (Si)

Silicon (Si) makes up 25.7% of the earth's crust by weight, and is the second most abundant element, exceeded only by oxygen. It has an atomic number of 14, an atomic mass of 28.0855 and an atomic radius is 0.1776 nm. The arrangement of outer electrons around the Si nucleus is based on two 3*s* shell electrons and two 3*p* shell electrons (electronic configuration: [Ne] $3s^2$ $3p^2$). Si has a gray color and a metallic luster which increases with the size of the crystal. It is similar to glass in that it is rather strong, very brittle, and prone to chipping.

Si is a tetravalent metalloid and is less reactive than its chemical analog carbon. Si crystallizes in the same pattern as diamond, in a structure which Ashcroft and Mermin call “two interpenetrating face-centered cubic" primitive lattices (figure 2.2-2). Even though it is a relatively inert element, Si still reacts with halogens and dilute alkalis but most acids do not affect it.

Si can form alloys with metals such as aluminum. The melting point of pure Si is 1410°C. At certain temperatures, Si is able to form a eutectic mixture with Au. This is a mixture of two (or more) phases at a composition that has the lowest melting point, and where the phases simultaneously crystallize from molten solution at this temperature. The proper ratios of phases to obtain a eutectic are identified by the eutectic point on a binary phase diagram.

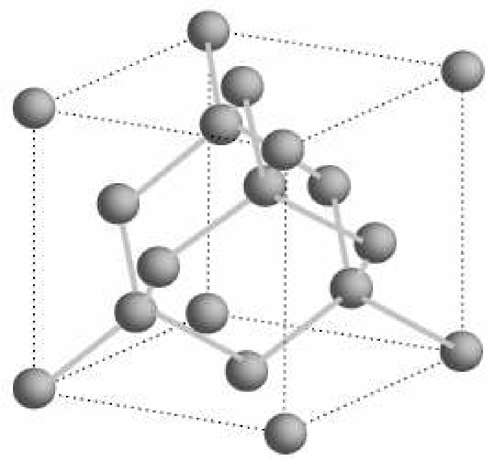

Figure 2.2-2: Crystal structure of silicon [48]. This crystalline form is called the "diamond lattice". The lines between silicon atoms in the lattice illustration indicate nearest-neighbour bonds. The cube side for silicon is 0.543 nm.

2.2.3 The Au-Si Phase Diagram

A phase diagram is a graphical representation of the regions and boundaries of existence for different phases, as states of aggregation belonging to a given physico-chemical system, in dependence of two or more thermodynamic quantities, e.g. temperature, pressure, concentration. Figure 2.2-3 shows a phase diagram representative of the Au-Si alloy system. A Au-Si alloy with 19.5 % atomic Si and 80.5 % Au melts at T=363°C, while pure Au and pure Si are solid up to 1063°C and 1412°C respectively (figure 2.2-3). The Au-Si phase diagram is of the simple eutectic type; dominated by a low temperature eutectic point at 363 ± 2 °C. At temperatures above the eutectic temperature the Au-Si alloy particle transforms into a liquid droplet with a composition, which apparently corresponds to the silicon rich branch of the Au-Si phase diagram.

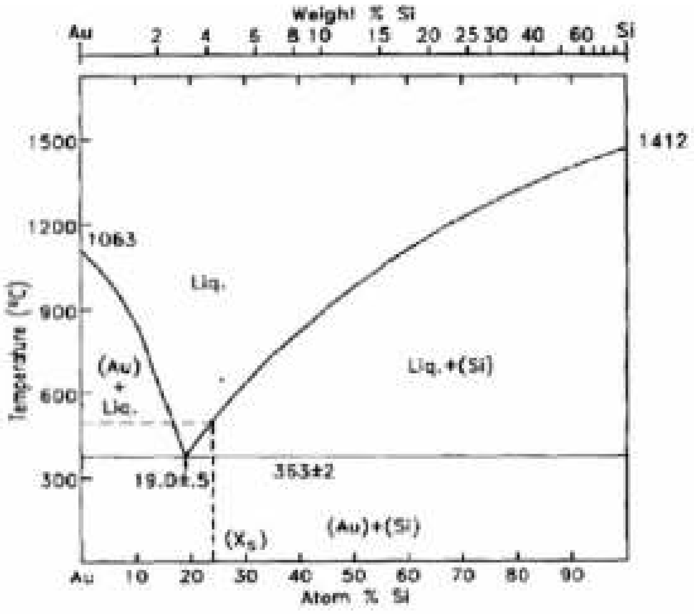

Figure 2.2-3: Phase diagram of Au-Si eutectic alloy[49].

2.3 Size Effects in Nanocrystals

Size, is a parameter that is currently being exploited to remarkably tune the chemical, and physical properties of materials. This is tremendously boosting the potential of contemporary technology especially in domains where device miniature is highly demanded. There are basically two types of size effects [50, 51]:

- Surface effects, which are smoothly scalable and are related to the fraction of atoms at the surface of a material.
- Quantum effects, which show discontinuous behaviour due to completion of shells in systems with delocalised electrons.

The threshold dimensions for the manifestation of these size effects vary for different materials.

2.3.1 Surface Effects

The surface of a sphere, A, scales with the square of its radius, r i.e. $A = \pi r^2$, while the volume, V, scales with r^3 (i.e. $V = \frac{4}{3}\pi r^3$). The total number of atoms, N, in this sphere, will scale linearly with its volume. The fraction of atoms at the surface (dispersion), F, scales with the surface area divided by volume, i.e. with the inverse radius (equation 2.3-1) and hence, also with $N^{-1/3}$. The same relation holds for long cylinders of radius, r, and for thin plates of thickness, d. Atoms at the surface have fewer direct neighbours than atoms in the bulk of a material.

$$F = \frac{A}{V} = \frac{3\pi r^2}{4\pi r^3} = \frac{3}{4} r^{-1}$$ **Equation 2.3-1**

This implies that particles with a large fraction of atoms at the surface have a low mean coordination number (the number of nearest neighbours). So F and the mean coordination number obey the same scaling law and are equivalent measures of surface effects [50].

Looking at things from the point of view of cohesive energy (bond energy per atom), the atoms in the interior of a cluster are more highly coordinated, form more bonds, and therefore are more stable than those at the surface of the cluster. In cubic crystals for example, the corner atoms are the least saturated ones, followed by the edge, the in-plane surface, and then the atoms in the interior. As a result, the corner atoms normally exhibit the highest affinity to form bonds or adsorbate molecules, followed by the edge, and in-plane surface atoms. This fact is of uttermost importance in the catalytic activity of clusters. In addition, the low coordination number of edge and in particular, corner atoms, leads to them having a low stabilisation and so are often missing on single crystals even in thermodynamic equilibrium.

A further consequence of the low stabilisation of atoms or molecules at the surface is lower melting point of surface layers. This has been known dating as far back as 1871 when W. Thomson descried the melting point as a factor, which scales inversely with the radius of a particle - the Gibbs-Thomson equation (equation 2.3-2):

$$\frac{T_m - T_m^*}{T_m^*} = \frac{\Delta T_m}{T_m^*} = -\frac{2V_m(l)\gamma_{sl}}{\Delta H_m r}$$ **Equation 2.3-2**

Where T_m, is the melting point of the cluster with radius, r, T_m^*, the melting point of the bulk material, $V_m(l)$, the molar volume of the liquid, γ_{sl}, the interfacial tension between the solid and the liquid surface layer, and ΔH_m, the bulk latent heat of melting.

Phase transitions are collective phenomena. With a low number of atoms in a cluster, a phase transition is less well defined i.e., no longer sharp. Small clusters behave more like molecules rather than bulk matter. Hence, rather than referring to a solid-liquid transition as phase change, it may be more apt to speak of different structural isomers which coexist over a range of temperatures [52]. For example, part of a cluster may be solid while another part exhibits liquid-like dynamic behaviour. At a given temperature, the solid-like regime may fluctuate in position and size. When phases are no longer well defined, the Gibbs phase rule loses its meaning [52].

2.3.2 Quantum Effects

The dependence of spatial arrangement of electron levels is termed a quantum size effect. Excitons have an average physical separation between the electron and hole, referred to as the exciton Bohr radius. This physical distance is different for each material. In bulk, the dimensions of a crystal are much larger than the exciton Bohr Radius, allowing the exciton to extend to its natural limit. However, if the size of a material becomes small enough that it approaches the size of the material's exciton Bohr radius, then the electron energy levels can no longer be treated as continuous - they must be treated as discrete, meaning that there is a small and finite separation between energy levels. This situation of discrete energy levels is called quantum confinement, and under these conditions, the material properties cease to resemble those of the bulk.

2.3.3 Size Effects in Au

Basic properties of bulk Au have previously been described in section 2.2.1. As the size of Au diminishes, the impact of dimension manifests itself in several ways. With downscaling, the equilibrium structure of Au changes to an icosahedral symmetry [50]. The melting point of Au nanoparticles is also observed to drop by approximately 727°C with a transition from the compact metal that melts at 1064.4°C to 2 nm nanoparticles [53].

In terms of chemical reactivity, Au possesses a high ionization potential and accordingly has poor affinity towards molecules. Surface science investigations have proven that no dissociative adsorption of H_2 and O_2 takes place over smooth surfaces of Au at temperatures below 200°C, indicating that Au is catalytically inactive for hydrogenation and oxidation. Contrary to this, size-dependent low temperature activity of Au nanoparticles in hydrogenation and oxidation reactions has been demonstrated [54, 55].

The electronic and optical properties of Au nanoparticles also demonstrate distinctive alterations with downscaling. Optical absorption properties also vary with changes in size**.** For example, 10 nm Au nanoparticles absorb green light and appear red. Au in its bulk state is a nonmagnetic material. However, Au nanoparticles with diameters ranging between 2 – 3 nm exhibit considerable magnetism. A transition from metallic to semiconductor or even insulator properties has been predicted to arise when Au nanoparticle diameter is, $d \leq 2$ nm [50].

2.3.4 Size Effects in Si

Bulk Si oxidizes in air to give SiO_x. This also occurs after a Si surface is exposed to air post an etching process. Small Si nanostructures possess an amorphous SiO_2 sheath after they have been synthesised. However, they have been found to be resistant to re-oxidation after the oxide sheath has been removed by a wet chemical etch process.

Bulk Si can adopt several crystallographic orientations. On the other hand, the crystallographic orientations of Si nanostructures show distinct size dependency [56, 57]. The crystals typically adopt <111> orientations when their diameters are greater than 40 nm and <110> orientations when their diameters are below 40 nm.

The band gap of Si is known to be of the order of 1.1 eV. This band gap is found to widen with decrease in dimension with values of ~ 3 eV at diameters of ~ 1 nm [58]. Bulk Si is also known to be an indirect band gap semiconductor i.e. it requires that photon emission and absorption processes involve a momentum balancing phonon (lattice vibration). However, with downscaling, Si becomes a direct band gap semiconductor due to quantum confinement effects at critical diameter of 20 nm. As a result, Si becomes a light emitting material. Considering the dominant role Si plays in contemporary electronic devices, this constitutes a great advantage in that this material has better compatibility when integrated into circuits.

2.4 Synthesis of Nanomaterials

2.4.1 Synthesis of Nanoparticles

A nanoparticle is defined as a microscopic structure with at least one dimension less than 100 nm. Nanoparticles are effectively a bridge between bulk materials and atomic or molecular structures.

Nanoparticles may be synthesized through several routes e.g. cryochemical synthesis, physical methods such as low temperature plasma, molecular beams, gas evaporation, cathode sputtering, electroexplosion, laser induced electrodeposition, mechanical methods such as ball milling [59], and self assembly methods like micelle nanolithography [60]. Of all these, emphasis shall be laid on the micelle nanolithography technique which has been employed in this work. As the name implies, this technique makes use of micelles, which are aggregates of surfactant molecules dispersed in a liquid colloid.

2.4.1.1 Micellization

The process of forming micelles is known as micellization. A typical micelle in aqueous solution forms an aggregate with the hydrophilic "head" regions in contact with surrounding solvent, sequestering the hydrophobic tail regions in the micelle center. Micelles are often globular and roughly spherical in shape, but ellipsoids, cylinders, and bilayers are also possible. The shape and size of a micelle is a function of the molecular geometry of its surfactant molecules and solution conditions such as surfactant concentration, temperature, pH, and ionic strength.

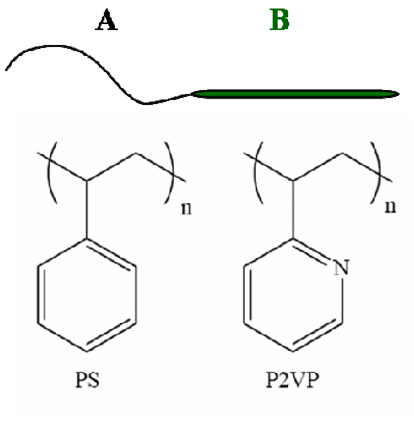

Figure 2.4-1: **Schematic illustration of a diblock copolymer with distinct hydrophobic (PS) and hydrophilic part (P2VP).**

In a nonpolar solvent, it is the exposure of the hydrophilic head groups to the surrounding bulk solvent that is energetically unfavorable. In this case, the hydrophilic groups are sequestered in the micelle core and the hydrophobic groups remain solvent-exposed on the surface of the micelle. These reverse micelles are extremely difficult to form from surfactants with charged head groups, since hydrophilic sequestration would create highly unfavorable electrostatic interactions. Figure 2.4-2 is a schematic illustration of a micelle (A) with its hydrophilic head (poly-2-vinyl pyridine: P2VP) on the outside and a reverse micelle with its hydrophilic head on the inside (B).

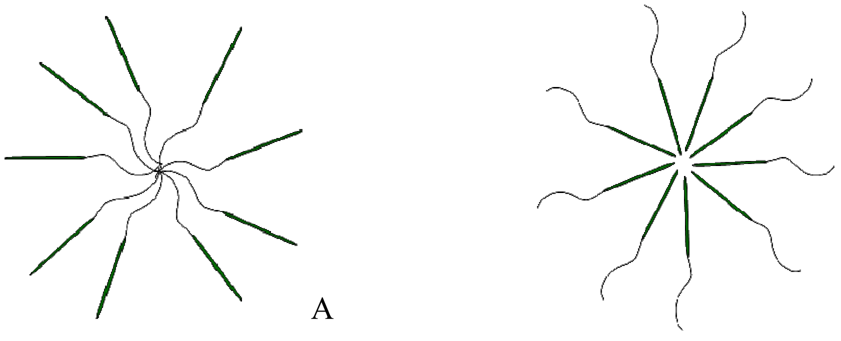

Figure 2.4-2: **Schematic representations of, (A) a micelle and, (B) a reverse micelle with the polar components on the outside and inside respectively.**

2.4.1.2 Micelle Nanolithography

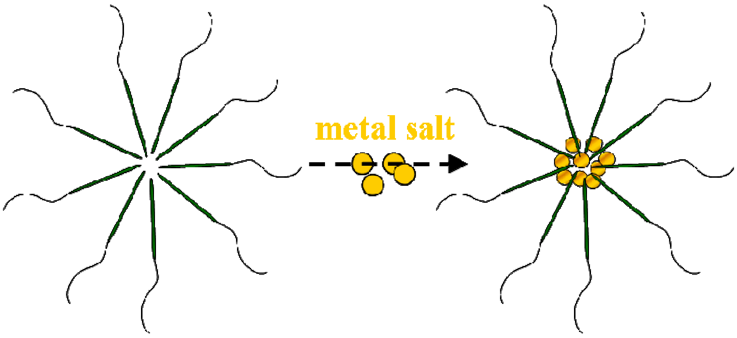

Figure 2.4-3: Schematic illustration of a reverse micelle loading mechanism. The metal salt selectively dissolutes into the polar micelle core.

As earlier mentioned, micelle nanolithography is a self-assembly technique which utilizes the aggregation of diblock copolymers into micelles. Micelle formation occurs when the diblock copolymer is dissolved in a solvent, which is selective for one of the blocks. If the blocks that form the core of the micelle or the dispersed domains are polar and able to interact with a transition metal compound, the latter can be selectively incorporated within the micelles or the domains [61]. The micelle core-shell structure forms a nano-reactor that permits the selective dissolution of metal precursor salts into the polar core or the generation of mono-dispersed metal nanoparticle in each core after an additional chemical reduction step [61]. An appropriate, clean substrate is then immersed into and retracted from a solution containing metal loaded micelles at a reasonable speed in order to coat the surface with a monolayer of micelles. The solution on the surface is evaporated in air and a surface with a regular mono- micelle film is formed on the substrate. A preceeding plasma treatment (H_2 or O_2) of the surface selectively etches away the organic part of the film leaving behind the inorganic nanoparticles. Figure 2.4-4 and figure 2.4-5 are schematic illustrations of the Au nanoparticle preparation, indicating the surface coating process and the subsequent plasma treatment performed to etch the organic components of the metal-loaded micelle system.

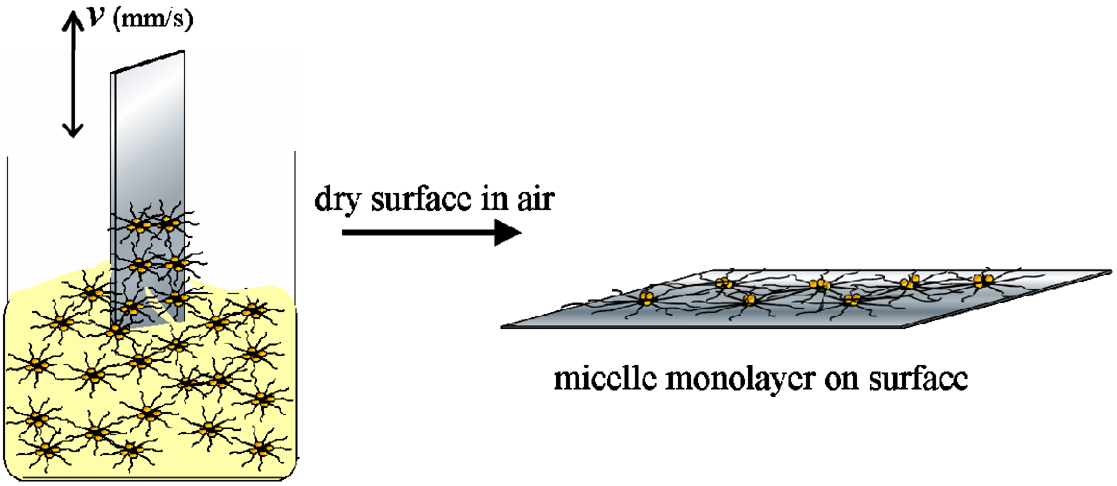

Figure 2.4-4: **Schematic illustration of metal-loaded micelles in solution. A monolayer of micelles is brought to a surface by dipping the surface in a solution of micelles as a specific speed.**

The diameter of the micelles is controlled by the molecular weight of the block copolymers, the interactions between the polymer blocks and the interaction between the blocks with the solvent. The particle size is predominantly controlled by the amount of metal precursor added to the micelle solution. Thus, nanometer-sized particles are embedded in a 10 –100 nm thick shell of polymer. The size of the resultant nanoparticles is controlled by the amount of salt introduced into the unloaded micelle solution, while the length of the polymer chain controls the distance between the nanoparticles [43].

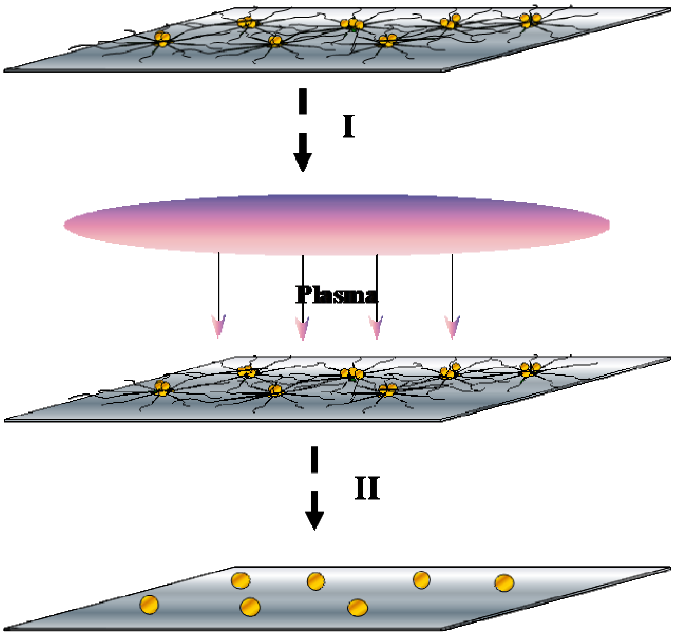

Figure 2.4-5: **Schematic illustration of a Au nanoparticle preparation process: I. treatment of loaded micelles in a plasma to etch away the organic component. II. Resultant Au nanoparticles in the same initial order as the micelles on the surface after the plasma etch procedure**

2.4.2 One-dimensional (1-D) Material Synthesis

2.4.2.1 Chemical Vapour Deposition (CVD)

Figure 2.4-6 shows the schematic representation of CVD 1-D material growth from nanoparticles on a substrate. The substrate coated with nanoparticles is heated to the desired reaction temperature and usually maintained at this temperature. The feed gas, which contains precursor molecules of the desired material, is then introduced into the growth chamber. The molecules are split locally at the nanoparticle or thermally, if the temperature in the chamber is high enough, to dissociate the molecular bonds. Nucleation between the nanoparticles and the precursor molecules results in a nanoparticle alloy, which when supersaturated, leads to precipitation of the adsorbed material. Upon precipitation, the material crystallizes and forms a 1-D structure. Growth may occur with the nanoparticle seeded at the base (root growth) or at the tip (tip growth) of the 1-D structure. The nanoparticle seed controls the diameter of the resulting 1-D structure, as well as its position on a substrate. Dictating the diameter of 1-D structures via nanoparticles allows for better control over their properties (e.g. mechanical, optical, and electrical) and permits exploitation of size driven phenomena that occur in the material in question. As a result, controlling 1-D material localization on a substrate enhances directed surface functionality.

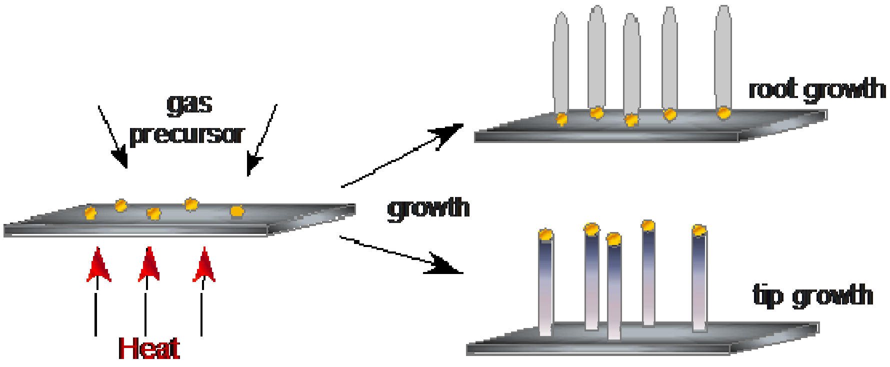

Figure 2.4-6: Schematic illustration of 1-D material growth in a chemical vapour deposition process. A nanoparticle-coated substrate is heated and exposed to a precursor gas. Precursor gas diffusion and subsequent precipitation leads to 1-D material formation. The location of the nanoparticle with respect to the 1-D structure is a reflection of the nanoparticle-substrate interaction.

.

2.5 Electron microscopy

2.5.1 Fundamentals

Electron microscopy requires a source to illuminate a sample with an electron beam. A heat filament can produce electrons, by field emission or a combination of both. The key parameters of the electron source are the virtual source size, the brightness, and the energy spread of the emitted electrons. The source size (and shape) determines the resolution, the brightness is equivalent to the intensity of the beam and a large energy spread causes chromatic aberrations at the lenses. The resolution of an electron microscope is determined by the *deBroglie wavelength* of the electrons, λ_{dB}, which is defined as shown in equation 2.5-1, where h is the Planck constant, m, the electron mass and $W = eV$ is the kinetic energy given by the electron charge, e, and the voltage, V, which is used to accelerate the electrons. Hence, the resolution of an electron microscope strongly depends on the values for V. The beam of electrons formed by the electron source is accelerated toward the specimen using a positive electrical potential. Magnetic lenses and metal apertures are used to define the electron beam and magnify the image. The lenses work electromagnetically: specially designed magnets, which focus the electron beam onto the sample, deflect the electrons. The focal lengths of the lenses are tuneable via the current, which is used to drive the magnets. The lenses can be classified as condensers, objectives and projectors.

$$\lambda_{dB} = \frac{h}{\sqrt{2mW}} = \frac{h}{\sqrt{2meV}}$$

Equation 2.5-1

Specimen examination employing electron microscopy can yield information such as the topography, morphology, elemental composition and crystallographic nature of the material under investigation.

2.5.2 Scanning Electron Microscopy (SEM)

The SEM works in reflection mode: An electron beam (usually with energy of 1 KeV – 20 KeV) is focused on the sample surface to a size of approximately 1 nm – 10 nm. Spatial information can be achieved by scanning the focus on the sample. This is done by a scanning (or deflecting) coil, which is put in the optics of the microscope.

2.5.2.1 Interaction of Electrons with Thick Specimen

When an electron beam collides with the specimen, several processes occur. The most relevant of these include:

2.5.2.1.1 Elastic Backscattering

This occurs when an incident electron collides with an atom in the specimen, which is nearly normal to the incident's path. The incident electron is then scattered "backward" 180 degrees. The backscattered electron leaves the sample without any alterations in their energy, W:

$$W_i = W_f \quad \textbf{Equation 2.5-2}$$

Where W_i, and W_f are the initial and final energy of the electrons respectively. The production of backscattered electrons varies directly with the specimen's atomic number. These differing production rates cause elements with a higher atomic number to appear brighter than lower atomic number elements. This interaction is utilized to differentiate parts of the specimen that have different average atomic number.

2.5.2.1.2 Inelastic Backscattering

Some electrons are backscattered with a different energy. An energy loss of less than 50 eV is usually due to plasmon excitation. These excitations are very specific to the matter, which is illuminated, because they strongly depend on the electronic band structure on the crystal interfaces or defects.

$$W_i \neq W_f$$ **Equation 2.5-3**

2.5.2.1.3 Secondary Electrons

These are instigated by an incident electron passing "near" an atom in the specimen, near enough to impart some of its energy to a lower energy electron (usually in the K-shell). This causes a slight energy loss and path change in the incident electron and the ionization of the electron in the specimen atom. This ionized electron then leaves the atom with a very small kinetic energy (~ 5eV) and is thus termed a "secondary electron". Each incident electron can produce several secondary electrons. Secondary electrons have a broad energy distribution with a maximum below 50 eV. They are usually employed in spatial imaging.

Production of secondary electrons is very topography related. Due to their low energy, only secondary electrons that are very near the surface (depth < 100 Å) can exit the sample and be examined. Any changes in topography in the specimen that are larger than this sampling depth will change the yield of secondary electrons due to collection efficiencies. Collection of these electrons is aided by using a "collector" in conjunction with the secondary electron detector. The collector is a grid or mesh with a +100V potential applied to it, which is placed in front of the detector, attracting the negatively charged secondary electrons to it that then pass through the grid-holes and into the detector to be counted.

2.5.2.1.4 Auger Electrons

Auger electrons result from the de-energization of a specimen atom after a secondary electron is produced. Since a lower (usually K-shell) electron was initially emitted from the atom during the secondary electron process, an inner (lower energy) shell now has a vacancy. A higher energy electron from the same atom can "fall" to a lower energy, filling the vacancy. This creates an energy surplus in the atom which can be corrected by emitting an outer (lower energy) electron; an Auger electron. The Auger electrons are highly element specific. Their energies range from 100 eV to 1 KeV.

Auger electrons have a characteristic energy, unique to each element from which they are emitted. These electrons are collected and sorted according to energy to give compositional information about the specimen. Since Auger electrons have relatively low energy they are only emitted from the bulk specimen from a depth less than 30 Å.

2.5.2.1.5 X-rays

X-rays originate from electron ionization of atoms by removing a shell electron. This is usually a K-shell electron emitted from the atom during the secondary electron process. A higher energy electron from an outer shell immediately fills this vacancy left by the emitted electron. As the electron "falls", it emits energy, usually X-rays to balance the total energy of the atom.

X-rays or light emitted from the atom will have a characteristic energy, which is unique to the element from which it originated. Hence, an element specific analysis can be performed.

With all this in mind, it is evident that by using different detectors with sensitivity to electrons of different energies or even photons, SEM images become specific to special properties of the specimen under observation. The volume inside the specimen in which interactions occur while being struck with an electron beam is known as the specimen interaction volume. This volume depends on the following factors:

- Atomic number of the material being examined; higher atomic number materials absorb or stop more electrons and so have a smaller interaction volume.
- Accelerating voltage being used; higher voltages penetrate farther into the sample and generate larger interaction volumes
- Angle of incidence for the electron beam; the greater the angle (further from normal) the smaller the volume

Figure 2.5-1 illustrates an example of a typical interaction volume for a specimen with atomic number $Z = 28$, imaged with an accelerating voltage of 20 KeV and with the beam normal to the specimen surface. The focus of the incident electron beam on the specimen surface is important. The smaller the focus of the electron beam, the better the achievable resolution.

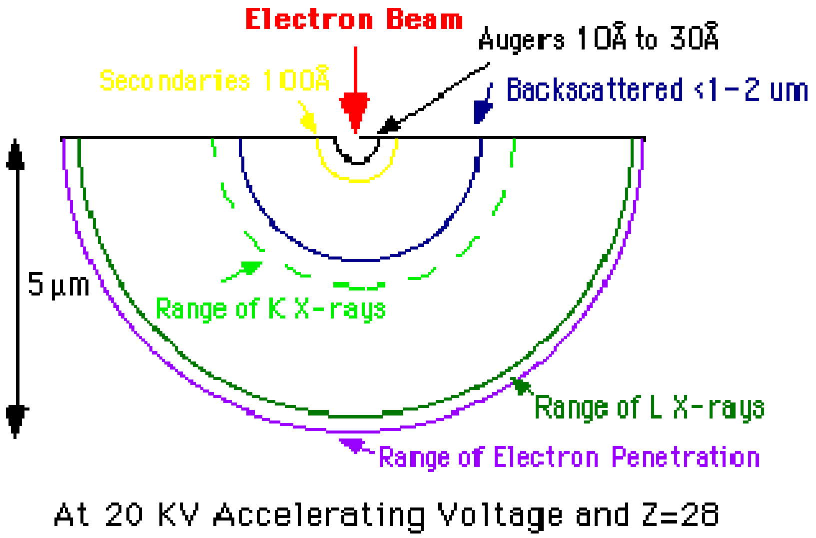

Figure 2.5-1: Schematic illustration of the interaction volume for a specimen with atomic number $Z = 28$. The acceleration voltage in this case is 20 KeV [62].

Not necessarily all electrons or photons listed above are emitted from an illuminated area. The primary electrons slightly penetrate the sample and exhibit a relatively large halo about $R_{pe} \approx 1$ µm in diameter around the focal spot. X-rays are emitted from this halo and thus, an X-ray image will not have a resolution better than 1 µm. The reach of backscattered electrons, R_{be}, is approximately half that of the primary electrons, R_{pe}. The secondary electrons have a rather limited reach, R_{se}, in a specimen. Hence, most of them are emitted very close to the focal spot. Some secondary electrons are produced at the surface as backscattered electrons, which may reduce the resolution. As for Auger electrons, these are only emitted directly from the surface.

2.5.3 Transmission Electron Microscopy (TEM)

In TEM, the electron beam is defined by a condenser lens system. The beam hits the sample, which has to be thin enough to be transparent for electrons. After traversing the sample, the electrons are collimated by an objective aperture and an objective lens. The number of diffracted spots that contribute to the final image can be restricted here. The sector lens can be used to magnify the image or the diffraction pattern. Hence, two different modes are possible: the microscopic imaging mode and the analyzing diffraction mode. Finally, the projector lens images the electrons on a screen or a two dimensional camera.

2.5.3.1 Interaction of Electrons With Thin Specimen

The processes that occur between an accelerated electron beam and a thin TEM specimen are summarized below:

2.5.3.1.1 Unscattered Electrons

Unscattered electrons are incident electrons, which are transmitted through the thin specimen without any interaction occurring inside the specimen. The transmission of unscattered electrons is inversely proportional to the specimen thickness. Areas of the specimen that are thicker will have fewer transmitted unscattered electrons and so will appear darker, conversely the thinner areas will have more transmitted and thus will appear lighter.

2.5.3.1.2 Elastically Scattered Electrons

Elastically scattered electrons are incident electrons that are deflected from their original path by atoms in the specimen in an elastic fashion i.e. no loss of energy. These scattered electrons are then transmitted through the remaining portions of the specimen. All electrons follow Bragg's Law and thus are scattered according to equation (2.5-4). Where n is an integer, the variable λ, is the wavelength of the incident electrons, d is the distance between atomic layers in the crystal, and ϑ is the angle is incidence of the electrons. All incident electrons have the same energy (thus wavelength) and enter the specimen normal to its surface. All incidents that are scattered by the same atomic spacing will be scattered by the same angle. These "similar angle" scattered electrons can be collated using magnetic lenses to form a pattern of spots, each spot corresponding to a specific atomic spacing (a plane). This pattern can then yield information about the orientation, atomic arrangements and phases present in the area of the specimen being examined.

$$n\lambda = 2d \sin \vartheta$$ **Equation 2.5-4**

2.5.3.1.3 Inelastically Scattered Electrons

Inelastically scattered electrons are incident electrons that interact with specimen atoms in an inelastic manner, loosing energy during the interaction. These electrons are then transmitted through the rest of the specimen**.** The electrons can be utilized two ways:

- Electron Energy Loss Spectroscopy

The inelastic loss of energy by the incident electrons is characteristic of the elements that were interacted with. These energies are unique to each bonding state of each element and thus can be used to extract both compositional and bonding (i.e. oxidation state) information from the specimen region being examined.

- Kakuchi Bands

These are bands of alternating light and dark lines that are formed by inelastic scattering interactions that are related to atomic spacings in the specimen. These bands can be either measured (their width is inversely proportional to atomic spacing) or "followed" like a roadmap to the "real" elasticity scattered electron pattern. The reactions that occur when energetic electrons in SEM and TEM microscopes strike a specimen are summarised in figure 2.5-2. The reactions noted on the top side of the diagram are utilized when examining thick or bulk specimens (SEM) while the reactions on the bottom side are those examined in thin or foil specimens (TEM).

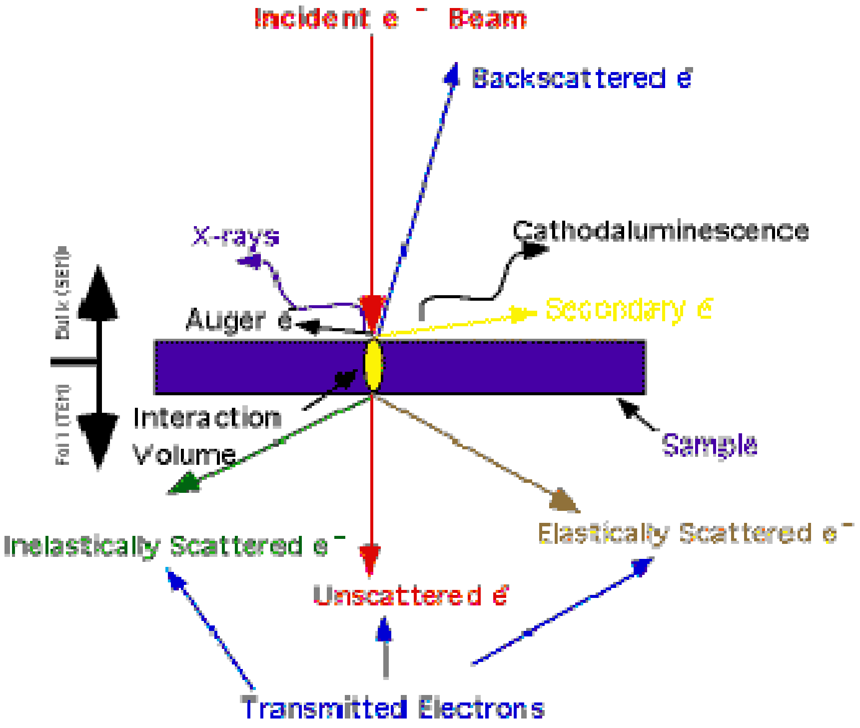

Figure 2.5-2: Schematic illustration of interactions of energetic electron in SEM (upper side) and TEM (lower side) microscopes [62].

2.6 X-ray Photoelectron Spectroscopy

2.6.1 Physical Principles

X-ray photoelectron spectroscopy (XPS) is a surface analysis technique that is used to analyze the chemistry of the surface of a material. Surface analysis by XPS basically involves the bombardment of a material in vacuum with (usually) soft x-rays. X-ray adsorption by an atom in a solid leads to ejection of an electron (photo-ionisation) either from tightly bound core level or from weakly bound valence levels (or molecular orbitals). A fraction of these electrons, generated close to the surface, escape into the vacuum system (photoemission). The overall process is known as the photoelectric effect. The photoemission is energy analysed to produce a spectrum (X-ray photoelectron spectrum) of electron intensity as a function of energy.

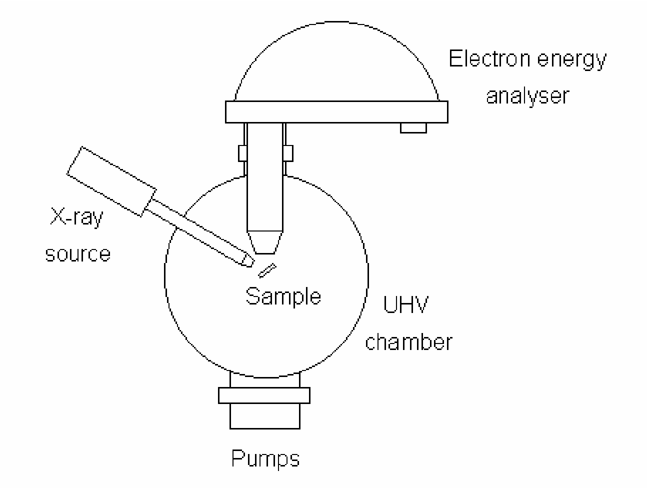

Figure 2.6-1: Schematic illustration of a typical XPS instrumental setup [63].

Figure 2.6-1 is a schematic illustration of a typical XPS instrumental setup. The main components of an XPS system include:

- A source of X-rays

- An ultra-high vacuum (UHV)
- Stainless steel chamber with UHV pumps
- An electron collection lens
- An electron energy analyzer
- Magnetic field shielding
- An electron detector system
- A moderate vacuum sample introduction chamber
- Sample mounts, sample stage and a set of stage manipulators.

For a conducting sample in electrical contact with the spectrometer, conservation of energy leads to the equation:

$$E_K = h\nu - E_B^F - \phi_{sp}$$ **Equation 2.6-1**

Where E_K is the measured kinetic energy of the emitted electron, $h\nu$ is the energy of the X-ray photon, E_B^F is the electron binding energy (BE) relative to the Fermi level (E_F) of the sample (defines as $E_F = 0$) and ϕ_{sp} is the work function of the spectrometer. Since the electron binding energy is the parameter of fundamental interest, the spectrometer can be set up to record the spectrum on this energy scale directly, rather than on the measured kinetic energy scale. The spectrometer energy scale must be accurately linear and correctly calibrated. This is achieved using clean metal standards with traceable peak energies across the energy range.

$$E_K = h\nu - E_B - \phi$$ **Equation 2.6-2**

For an insulating sample, which lacks a well-defined Fermi level and which can not be in electrical contact with the spectrometer, equation 2.6-1 does not apply. Additionally, the surface potential of the sample may be uncertain because of charging. A modified version of equation 2.6-1, i.e. equation 2.6-2 is used in this case, where ϕ is now a term which captures these uncertainties relating to surface potential and the actual reference point for E_B.

The clear implication is that for BEs from different insulating samples to be meaningfully compared, a common reference point needs to be established.

2.6.2 X-ray sources

Two types of X-ray sources are commonly used. Non-monochromated sources utilize Kα radiation from Al or Mg. These materials (as thin films deposited onto water-cooled copper targets) are bombarded with electrons up to 15 KeV in energy. The X-ray output consists of a continuous energy distribution extending up to incident electron energy (Bremsstrahlung), with much higher intensity at the characteristic Kα energy (~ 1.5 KeV). Monochromatic aluminum Kα X-rays are normally produced by diffracting and focusing a beam of non-monochromatic X-rays off of a thin disc of natural, crystalline quartz with a <1010> lattice. The resulting wavelength is 8.3386 angstroms (0.83386 nm) which corresponds to a photon energy of 1486.7 eV (Al Kα). The energy width of the monochromated X-rays is 0.16 eV, but the common electron energy analyzer (spectrometer) produces an ultimate energy resolution on the order of 0.25 eV which, in effect, is the ultimate energy resolution of most commercial systems. When working under everyday conditions, the typical high energy resolution (FWHM) is usually 0.4-0.6 eV. Non-monochromatic magnesium X-rays have a wavelength of 9.89 angstroms (0.989 nm) which corresponds to a photon energy of 1253 eV (Mg Kα). The energy width of the non-monochromated X-ray is roughly 0.70 eV, which, in effect is the ultimate energy resolution of a system using non-monochromatic X-rays. Non-monochromatic X-ray sources do not diffract out the other nearby X-ray energies and also allow the full range of high energy Bremsstrahlung X-rays (1–12 keV) to reach the surface. Figure 2.6-2 illustrates the events involved in a photoemission within an atom (e.g. carbon).

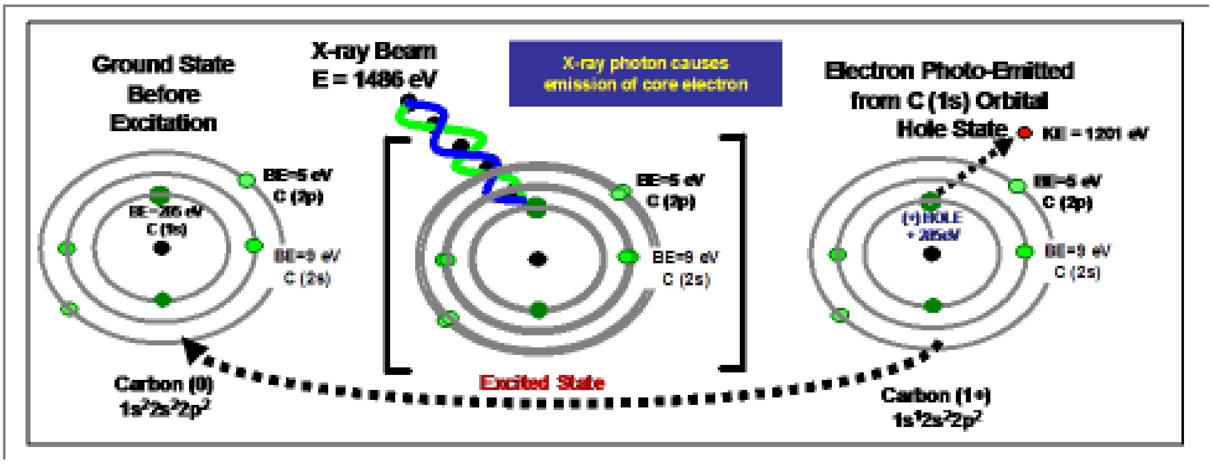

Figure 2.6-2: Schematic illustration of a photoemission process from a carbon atom [64].

Photoemission from an insulating material leads to the build up of a positive charge unless this can be dissipated in some way. Non-monochromated X-ray sources produce a broad, diverging X-ray beam, which illuminates the sample holder and other parts of the analysis chamber, generating low energy electrons. Bremsstrahlung excited low energy electrons also emerge from the front face of the Al window, separating the X-ray source from the analysis chamber, which is close to the sample. A sufficient flux of these low energy electrons is attracted to the sample surface to *neutralise* the charge build up.

2.6.3 The X-ray photoelectron spectrum

A typical XPS spectrum is a plot of the number of electrons detected (ordinate) versus the binding energy of the electrons detected (abscissa). Each element produces a characteristic set of XPS peaks at characteristic binding energy values that directly identify each element that exist in or on the surface of the material being analyzed. These characteristic peaks correspond to the electronic configuration of the electrons within the atoms, e.g., 1s, 2s, 2p, 3s, etc. The number of detected electrons in each of the characteristic peaks is directly related to the amount of element within the area (volume) irradiated.

Elastic photoemission in which a photoelectron is ejected from an atom in a solid and escapes from the surface without suffering energy loss, gives rise to discrete peaks whose energies obey equations 2.6-1 or 2.6-2 and which reflect the shell structure of the atomic electrons. Thus, at BE close to zero, the closely-spaced valence band levels appear and with increasing BE the increasingly tightly bound core levels.

2.6.3.1 Core levels

The nomenclature for core levels is nl_j where n, is the principal quantum number, l is the orbital angular number and j is the total angular momentum quantum number, $j=(l+s)$ where s is the spin angular momentum quantum number $(\pm 1/2)$. Thus s levels $(l=0)$ are singlets but all other levels $(l>0)$ give rise to doublets. The two possible states (table 2.6-1) are different in energy because the unpaired electron left in an orbital following photoionistaion can have its sin and orbital angular momentum vectors either parallel or anti-parallel. This is known as spin-orbit (*j-j*) coupling. The difference in energy between the doublet components, ΔE_j, is proportional to the spin-orbit coupling constant , which depends on the expectation value $<1/r^3>$ of the orbital involved, with *r,* being the average radius. The separation, which can be many electron volts, therefore increases with atomic number, *z*, for a given subshell (constant *n*, *l*) and decreases as *l* increases for constant *n*. The relative intensities of the components are given by the ratio of their degeneracies $(2j+1)$, as shown in table 2.6-1. The relative intensity of a core level peak is fundamentally determined by the atomic photoemission cross-section, σ, which depends on *z*, quantum numbers *n*, *l*, and *j* on the proximity of the photon energy to the photoemission threshold. However, for the two common X-ray sources, Al Kα and Mg Kα, the effect of this final factor on *relative* cross-sections is very small [65]. Relative intensities across the spectrum are also a function of the spectrometer.

Subshell	*j* values	Area ratio
s	**1/2**	**–**
p	**1/2, 3/2**	**1 :2**
d	**3/2, 5/2**	**2 :3**
f	**5/2, 7/2**	**3 : 4**

Table 2.6–1: Spin-orbit splitting parameters

2.6.3.2 Valence levels

Valence levels are those occupied by electrons with low BE (0 – 15 eV), which are involved in delocalized or bonding orbitals. The spectrum in this region consists of many closely spaced energy levels, producing a *band* structure. Hence, this region is usually referred to as the valence band. Figure 2.6-3 distinguishes the situation for conductors and insulators, where the density of electron states (per unit energy volume) is plotted. In the case of an insulator, the occupied *valence band* is separated from the empty *conduction band.* For metallic conductors, these bands overlap and the highest occupied state is termed the Fermi level, E_F. The kinetic energy of the valence photoelectrons in XPS is well over 1 KeV, which means that the final states occupy a flat continuum. As a result, the measured valence band is a close match to the initial density of states which is the focus of interest in studies of the electronic structure of materials. The contrast to ultraviolet photoelectron spectroscopy (UPS) where the kinetic energies are low, is such that the final states are just above E_F and structured (figure 2.6-3). The measured valence band is then a complex convolution of initial and final densities of states [65].

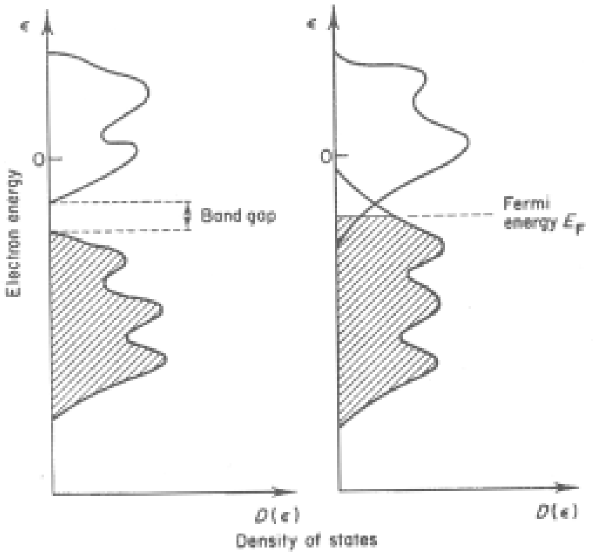

Figure 2.6-3: Schematic density of states for an insulator (left) and a metal (right). The shading indicates the extent to which the energy levels are occupied [65].

It is important to note that XPS detects only those electrons that have actually escaped into the vacuum of the instrument. The photo-emitted electrons that have escaped into the vacuum of the instrument are those that originated from within the top 10 to 12 nm of the material. All of the deeper photo-emitted electrons, which were generated as the X-rays penetrated 1–5 µm of the material, are either recaptured or trapped in various excited states within the material. For most applications, it is, in effect, a non-destructive technique that measures the surface chemistry of any material.

2.7 X-ray diffraction (XRD)

X-ray diffractometry (XRD) is a non-destructive analytical technique, which reveals information on the crystallographic structure, chemical composition, and physical properties of materials and thin films. The technique is based on the *elastic* scattering of x-rays from structures that have long range order. This is done by observing the scattered intensity of an X-ray beam hitting a sample as a function of incident and scattered angle, polarization, and wavelength or energy. X-ray diffraction analysis uses the property of crystal lattices to diffract monochromatic X-ray light. This involves the occurrence of interferences of the waves scattered at the successive planes, which are described by Bragg's equation (equation 2.5-4).

XRD is used as an adjunct to chemical analysis in the identification of the constituents of mixtures of crystalline phases.

3 Experiments

3.1 Surface Patterning

3.1.1 Nanoparticle Preparation

Poly-styrene-block-2-vinyl-pyridine (PS(*x*)-*b*-P2VP(*y*)) is dissolved in toluene to a concentration of 2 mg/ml and subsequently stirred for 24 hours. A suitable metal precursor salt (table 3.1-1), which is capable of forming a stable coordination with pyridine (e.g. $HAuCl_4$) is added and the micelle solution stirred for another 24 to 48 hours.

Salt
$Zn(NO_3)_2 \cdot 6H_2O$
$Co(NO_3)_2 \cdot 6H_2O$
$Fe(NO_3)_3 \cdot 6H_2O$
$Cu(NO_3)_2 \cdot 9H_2O$
$Ni(NO_3)_2 \cdot 2.5H_2O$
$HAuCl_4 \cdot xH_2O$

Table 3.1–1: Metal precursor salt used for the preparation of nanoparticles (Sigma Aldrich)

3.1.2 Surface Preparation

Si, Si/SiO_x and glass surfaces were used as supports for two dimensional arrays of Au nanoparticles. All surfaces were cleaned in *piranhia*, which is a concoction of hydrogen peroxide and sulphuric acid (H_2O_2 : H_2SO_4 in a ratio of 1: 3) for approximately 30 min in order to discard of any organic contaminants. The surfaces were subsequently rinsed, sonicated in distilled water and dried in a stream of nitrogen before the nanoparticle coating process.

To coat the surfaces (Si, Si/SiO_x and glass) with nanoparticles, a monolayer of metal-loaded micelles was brought to all surfaces by dipping a clean, dry surface in a Au-loaded micelle solution at a speed of 12 mm/ min. A subsequent treatment in H_2 (0.4 mbar; 250 W) or O_2 (0.1 mbar; 100 W) plasma, etches away the organic counterpart (micelles) leaving behind the inorganic nanoparticles on the surface in the same quasi hexagonal order as the initial metal-loaded micelles.

To bring Au nanoparticles in direct contact with a bare Si substrate, carbon tetraflouride (CF_4) plasma is used to etch the oxide layer within the growth chamber in order to prevent re-oxidation of the Si surface.

3.2 1-D Material Growth

3.2.1 Chemical Vapour Deposition (CVD)

Si 1-D structures reported in this work were grown on various Au nanoparticle - coated substrates by chemical vapour deposition (CVD). Growth experiments were performed in a chamber designed by Oxford Instruments Plasma Technology for growth of 1-D structures. Growth proceeded via thermal decomposition of silane (SiH_4) under a constant flow of 40 standard cubic centimetres per minute (sccm) and chamber pressure of ~ 2 mbar for 15 minutes at various temperatures. Growth of most 1-D nanostructures usually requires a nanoparticle seed, which acts as a catalyst and nucleation site to promote their selective growth.

3.3 Structural Characterization

3.3.1 Scanning Electron Microscopy

3.3.1.1 SEM sample preparation

SEM samples are administered in the maschine chamber as prepared if they are in the solid state and have a reasonably good conductive surface. If the surface is nonconductive, a very thin (< 10 nm) conductive layer (e.g. carbon or gold) is sputtered on the sample surface.

3.3.1.2 SEM imaging

A Zeiss filed emission scanning electron microscope (FE-SEM) (Ultra 55), which has an acceleration voltage range up to 30 KeV was used to characterize the morphology of the 1-D materials grown. The voltage range used was typically between 1 – 10 KeV.

3.3.2 Transmission Electron Microscopy (TEM)

3.3.2.1 TEM Specimen Preparation

For TEM imaging, a thin specimen with a thickness usually less than 10 nm is used in order to allow penetration of the accelerated electrons. Samples were prepared in three different ways:

- **Touch Method;** by which a TEM grid with a porous polymer film is placed on a sample surface with micrometer long Si 1-D structures, slightly pressed on the surface, and gently peeled off with a pair of tweezers. This enables several Si 1-D structures to stick to the TEM grid and be examined. This method is mainly applicable for very long structures (≥ 3 µm). Shorter structures do not adhere appropriately to the TEM grid.
- **Solution Method;** Si 1-D structures are scrapped into a small container containing an ethanol solution. A drop-wise admission of the Si 1-D material containing solution onto a Tem grid with a polymer film enables adequate *fishing* of the Si 1-D structures onto the TEM grid. This technique is applied to shorter Si 1-D structures (≤ 3 µm). The setback of the technique is the unpleasant aggregation of the Si 1-D structures which renders imaging of an isolated structure difficult.
- **Cross-sectional Specimen [66]:** A small disc with a diameter of about 3 mm, which corresponds to the size of a TEM specimen holder, is cut in an ultrasonic disc cutter (Gatan ultrasonic disc cutter). After mechanical thinning, the disc is ground from the substrate side down to 100 µm, and subsequently dimpled from the substrate side down to 30 – 50 µm. The minimum thickness depends on the brittle nature of the material being handled. Finally, a small hole is formed in the centre of the sample with a low angle ion mill (Gatan PIPS). Specimen regions that are transparent to the electrons are usually found close to the edge of the hole. The preparation of the cross-sectional sample enables the investigation of thin films on substrates as well as Si 1-D materials that have been grown on the

substrate. This method is applicable to very short Si 1-D structures (≤ 200 nm) and nanoparticles anchored to the substrate surface. The setback however, is the processing glue used to glue the upper disc (dummy) to the sample to be investigated. The amorphous nature of the glue usually covers the structures and renders imaging rather tedious.

3.3.2.2 TEM Imaging

Structural analysis of specimen was conducted with a Zeiss 912 Omega energy filtered transmission electron microscope, which functions with an acceleration voltage of 120KeV. High resolution TEM (HRTEM) measurements were performed with a Jeol Jem 4000 EX, which runs with an acceleration voltage of 400KeV as well as a JEOL 1250 ARM, which runs with an acceleration voltage of 1250 KeV. The HRTEM measurements were performed in a phase contrast-imaging mode.

3.3.3 X-ray Diffraction

XRD analysis was performed with a Bruker AXS diffractometer "D8-Discover" with a parallel beam path and energie dispersive detector "SOL-X". The radiation source was a Cu Kα 40KV/ 30mA with a wavelength λ = 1,541838 Å (wieghted average of Kα1 and Kα2). The measurements were performed in grazing incidence with a constant theta angle of 2°. For peak referrence, an ICDD-reference card # 04-0784 was used.

XRD measurements were performed on Au/α-Al_2O_3, Au/SiO_x/Si substrates and a Au/α-Al_2O_3 substrate which was initially annead at 500°C.

3.4 Surface Analysis

3.4.1 X-ray Photoelectron Spectroscopy (XPS)

XPS spectra were recorded with a Spec. Hemispherical analyzer using mono-chromatized My Kα radiation (1253.6 eV). The spot size area is about 5 mm^2. The pass energy ranged during the measurements ranged between 30 – 50 eV with a step size of 0.1 and 3 to 5 scans performed.

4 Results & Discussion

Before utilizing a material for any given purpose, the properties of the material have to be characterized in order to gain insight on its suitability for the desired process. In section 2.2.3, the melting temperature of Au nanoparticles is seen to drop as the size of the nanoparticles decreases. This low melting point can also be extrapolated to a decrease in boiling point with nanoparticle size reduction. This implies that the evaporation of Au nanoparticles is likely to set in well below temperatures assigned to bulk Au (2856°C). For this reason, it is important to characterize the thermal stability of Au nanoparticles in order to determine if they are a priori suitable for example, in catalysis reactions that are performed at high temperatures.

Section 4.1 illustrates the small size distribution obtained for Au nanoparticles prepared by micelle nanolithography as well as the order parameter acquired. The order parameter is a normalized parameter that indicates the degree of order of a system. An order parameter of 0 indicates disorder; the absolute value in the ordered state is 1 [67].

In section 4.1-1, the thermal stability of Au nanoparticles prepared by micelle nanolithography on SiO_x/Si substrates is discussed

4.1 Gold Nanoparticles prepared by Diblock Copolymer Micelle Nanolithography

Figure 4.1-1 shows an SEM micrograph of a SiO_x/Si surface coated with a Au-loaded micelle monolayer film (left). The surface after subsequent plasma treatment is shown in the SEM micrograph on figure 4.1-1 (right). Au nanoparticles are identified as circular white dots, arranged in a quasi hexagonal manner. The insets in both images show close ups of the hexagonal arrangement of the micelles as well as the Au nanoparticles which maintain the initial pattern after plasma treatment. A quantification of the hexagon arrangement was determined from the global bond orientational order parameter [67] by aid of a software program [68]**.** The computed value obtained for 1210 particles is 0.64 on a scale of 1 (indicating perfect hexagonal order). The spacing of the Au nanoparticles is approximately 121 nm. The size distribution taken for 540 Au nanoparticles was found to be on an average diameter of 10 ± 2 nm as indicated in figure 4.1-1c.

The growth of 1-D materials involves temperatures of hundreds of degrees above ambient conditions. Under such circumstances, the thermal stability of the Au nanoparticles becomes crucial. If the nanoparticles evaporate before the synthesis temperature is attained, then Si 1-D growth is inhibited due to the absence of the Au catalyst material.

Another major problem usually encountered during 1-D material is particle migration, which results in Ostwald ripening. This is the migration of part or all of the material from nanoparticles to merge and form larger ones. This is a fatal disadvantage in pre-organised systems, which require defined patterns because particle migration not only leads to distorted patterns but also alters the size of 1-D structures, whose diameter depend on the size of the nanoparticles. Hence, in order to be classified adequate for high temperature growth processes, nanoparticles must fulfil the following categories:

- Possess thermal stability at the reaction temperature.
- Be mechanically stable on the surface to inhibit migration.

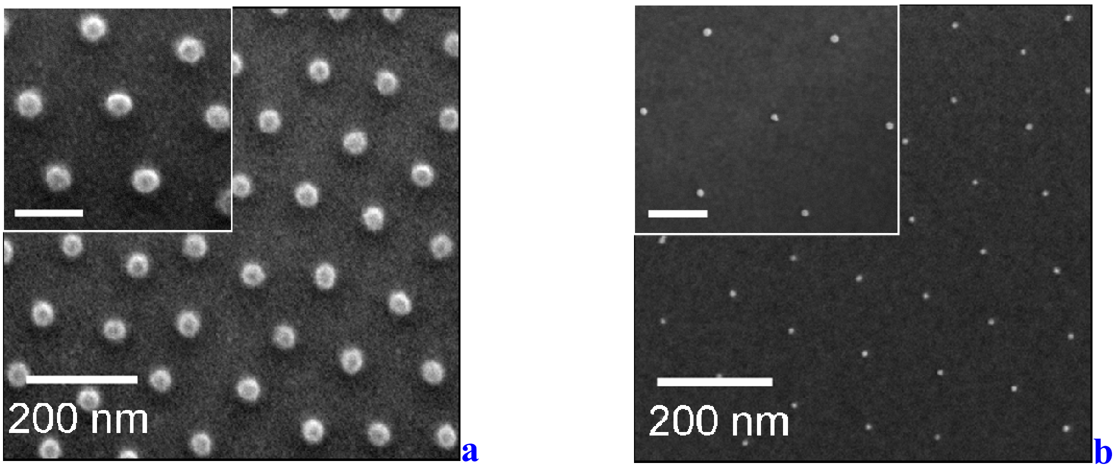

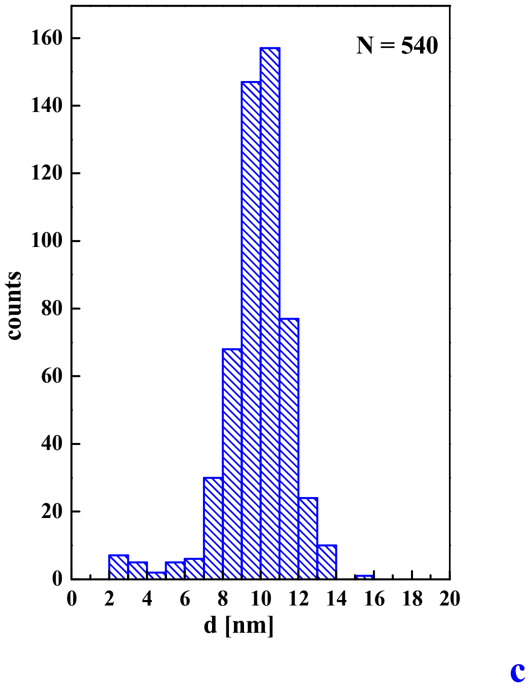

Figure 4.1-1: SEM micrographs (top view) of Au-loaded mono-micelle film before plasma treatment (a) and Au nanoparticles with diameters of approximately 8 nm arranged in a quasi-hexagonal order after plasma treatment (b). The scale bar in both insets is 100 nm in magnitude. The insets show Au-loaded micelles identified as white circular spots with diameters of ~ 30 nm (left), and Au nanoparticles (right) arranged in a hexagonal manner. (c) The size distribution histogram shows Au nanoparticles with an average diameter of 10 ± 2 nm.

4.1.1 Thermal Stability of Gold Nanoparticles on SiO_x/Si Surfaces

X-ray photoelectron spectroscopy (XPS) is a surface chemical analysis technique, which gives insight on the composition and the chemical state of elements on a solid. Au 4f and Si 2p photoelectrons have been acquired to systematically monitor temperature dependent changes in a Au/SiO_x/Si system. For this, a Au/SiO_x/Si system was heated from room temperature to 800°C in steps of 50°C / 30 min under ultra high vacuum (UHV) conditions after which, *in-situ* XPS measurements were performed.

Figure 4.1-2 illustrates XPS spectra recorded for the Si 2p and Au 4f photoelectrons from room temperature to 800°C. The Si 2p spectrum at room temperature (RT) shows two distinctive broad peaks at 104.36 eV and 100.02 eV, which correspond to Si in SiO_X and Si in the Si substrate respectively [69]. The slight shift of both Si 2p peaks to lower binding energies is probably due to desorption of remnant surface impurities and/or a change in the Femi level. Upon further heating, a thinning (desorption) of the oxide layer occurs which is evidenced by a drop in the intensity of the oxidic Si 2p peak. A systematic drop in the intensity of the Au 4f peaks (87.93 eV for Au $4f_{5/2}$ and 84.23 eV from Au $4f_{7/2}$ [70-72] as temperature is raised is a probably indication of Au evaporation. Upon transition from 700°C to 750°C, the Au 4f peaks assume shifts of the order of ~ 0.85 eV to higher binding energies, 88.8 eV (Au $4f_{5/2}$) and 85.05 eV (Au $4f_{7/2}$). This shift is probably due to the formation of a Au silicide [73]. This may have resulted from the possible diffusion of Au in a molten state to the Si layer as a consequence of oxide thinning. At 800°C, the Au nanoparticles appear to have evaporated. This is seen in the vanishing of the Au 4f peaks. To confirm this, an SEM analysis of the surface after 800°C heat treatment is performed. Figure 4.1-3 shows Au nanoparticles, ~ 20 nm in diameter, and inter-particle lateral spacing of ~ 120 nm (left). An SEM micrograph of the sample after heating (figure 4.1-3, right) reveals a surface with dark irregularly shaped spots, arranged in the same quasi hexagonal manner as the Au nanoparticles. The spots are approximately double the width of the Au nanoparticles and the distance between them is less than 120 nm. The holes probably originate from the spreading of the Au nanoparticles in a molten state at high temperatures, which subsequently diffuse into the SiO_x/Si substrate. The fact that diffusion of Au into Si occurs is well known [74]. The observation of dark spots rather than Au nanoparticles confirms the disappearance of the Au nanoparticles at 800°C. This implies the 20 nm Au nanoparticles can be exploited for catalysis up to 750°C. In addition, the fact that the dark spots on the SiO_x/Si substrate do not touch and maintain the quasi-hexagonal order is a clear indication that Au nanoparticle migration is considerably hindered. Point-like white features are observed at the centre of the dark spots. These are probably remnant of Au nanoparticles that are too small to give a detectable Au 4f photoelectron signal.

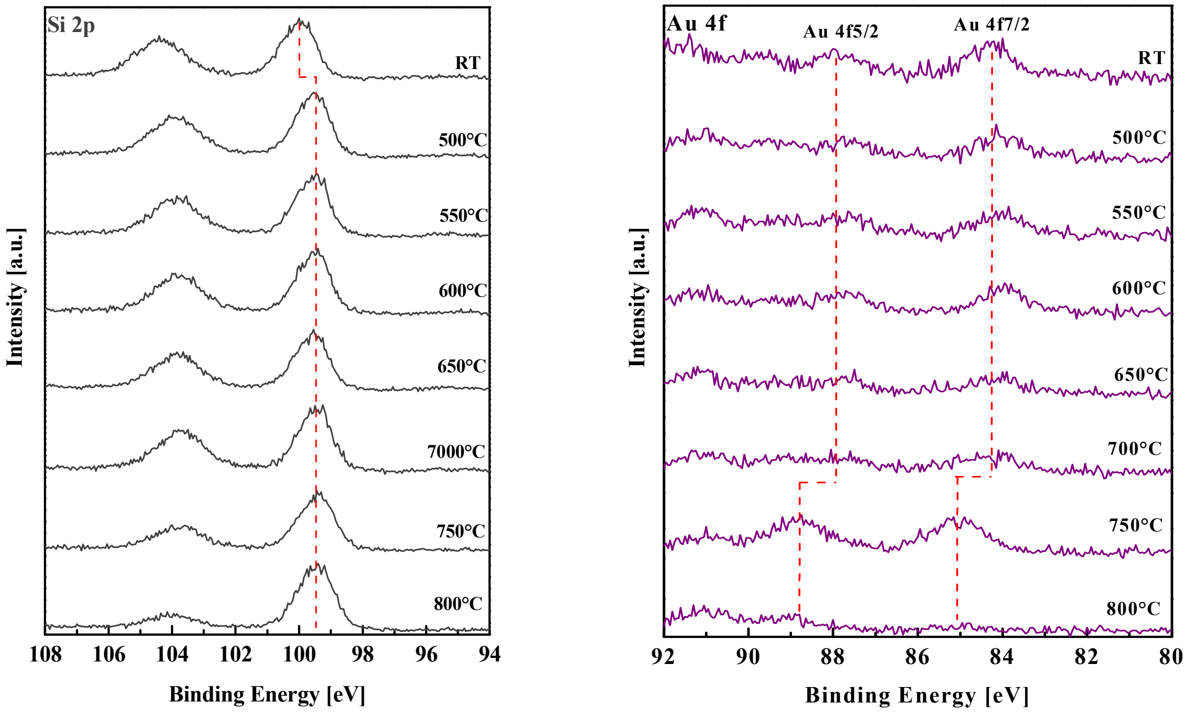

Figure 4.1-2 **XPS spectra showing Si 2p (left) and Au 4f (right) photoelectrons as a function of temperature. The shift (~ 0.48 eV) of the Si 2p peaks to lower binding energies with temperature rise from room temperature (RT) to 500°C is assigned to probable desportion of remnant impurities from the surface. The drop in the Si 2p oxidic peak is indicative of a thinning of the oxide layer as temperature rises. The shift (~ 0.85 eV) of the Au 4f peaks to higher binding energies is assigned to the probable formation of a silicide resulting from Au diffusion through a thinning oxide layer to the underlying Si surface.**

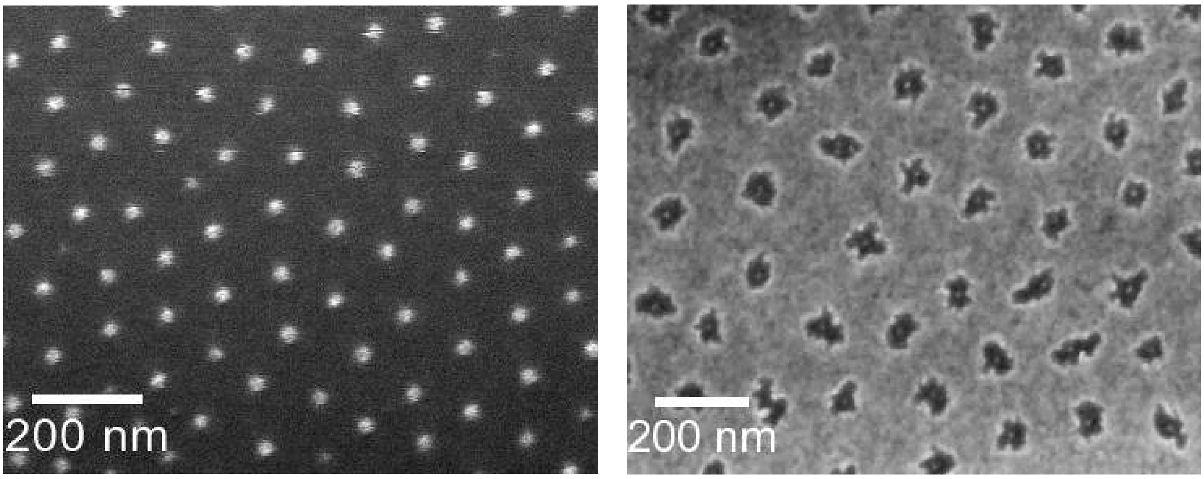

Figure 4.1-3: SEM images (top view) of Au/SiO_x/Si showing Au nanoparticles in quasi hexagon al order with diameters of ~ 20 nm (left). The same surface, after heat treatment to 800°C in steps of 50°C / 30 min under UHV conditions (right). The dark spots are approximately double the width of the Au nanoparticles. This may have resulted from the nanoparticles spreading upon melting and penetrating the substrate during the high temperature process.

An atomic force microscopy (AFM) analysis of the surface (1 μm^2) after heat treatment reveals the dark spots to be nanopores, which according to this analytical method, are about 5 nm in depth. The AFM micrograph in figure 4.1-4 illustrates this observation.

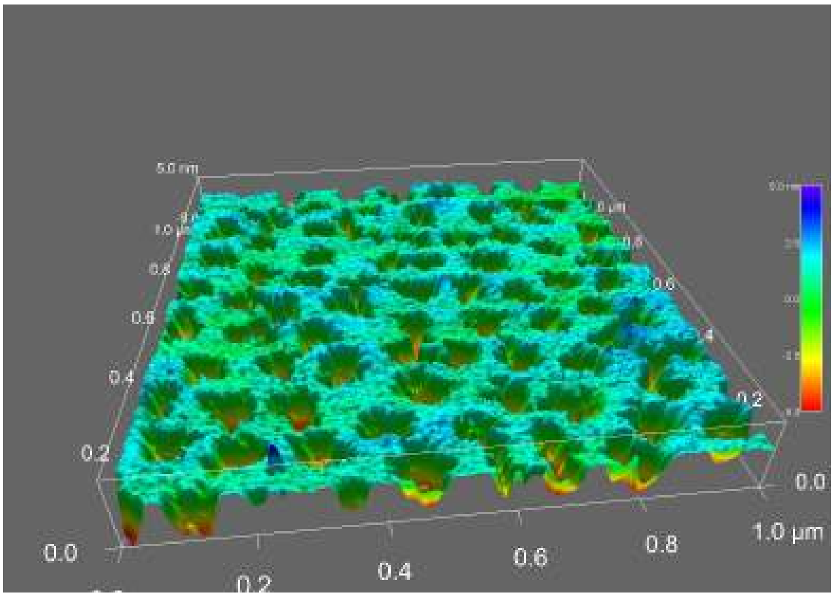

Figure 4.1-4: AFM scan of a Au/SiO_x/Si surface (1 μm^2) after heat treatment to 800°C under UHV conditions. The surface is rough and porous. The pores are ~ 5 nm in depth

TEM cross-sectional analysis performed on the same surface reveal results, which underpin the AFM observations. Figure 4.1-5 shows a cross sectional view of the surface. The micrograph shows the SiO_x/Si substrate with *pit* or nanopore like structures filled with glue from the sample processing procedure. The average dimension of the nanopores in this figure correspond to 8 ± 2 nm in depth and 36 ± 5 nm in breadth. The differences in nanopore depth values between AFM and TEM are attributable to the finite dimensions of the AFM cantilever.

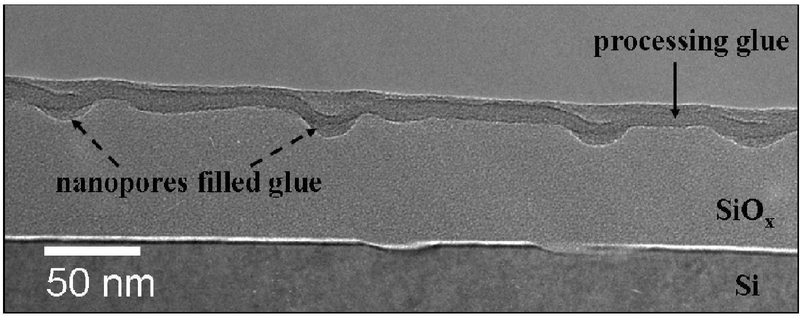

Figure 4.1-5: TEM micrograph of the $Au/SiO_x/Si$ surface after heat treatment to 800°C under UHV conditions. Au nanoparticles are not observed. The nanopores are filled with glue from the sample preparation process. The nanopores are typically 8 nm in depth and 36 nm in breadth.

4.1.2 The $Au/SiO_x/Si$ Conformation

Section 4.1-1 indicates, that, Au nanoparticles manifest remarkable stability at elevated temperatures on a SiO_x/Si substrate. This is reflected in their reluctance to migrate at high temperatures as indicated by figure 4.1-3. A possible explanation for this may be due to partial embedded nature of the Au nano particles in the SiO_x layer of the SiO_x/Si substrate (figure 4-1-6). Figure 4.1-6 is a TEM micrograph showing the morphology and location of Au nanoparticles with respect to the underlying SiO_x/Si substrate. This is better elucidated in the HRTEM image (figure 4.1-6, inset). The TEM micrograph shows a row of Au nanoparticles on the SiO_x/Si substrate. The inset shows a Au nanoparticle partially embedded in the SiO_x matrix. This implies the matrix anchors the Au nanoparticle, clamping it to the surface and inhibiting migration during high temperature processes. This results from the fact that the H_2

plasma etching process promoted the growth of an additional SiO_x layer. The base pressure of the plasma chamber, is appoximately 10^{-4} mbar. This not the very best vacuum condition for a clean environment. There is a high probability that the plasma is a mixture of H_2 and some contamination from atmospheric humidity, which may promote the growth of an oxide layer at the sides of the Au nanoparticle. This growth may be caused by the possible elevated temperatures (i.e. T > room temperature) in the chamber during the plasma etch process. A chronological monitor of the oxide layer by XPS (figure 4.1.7) reveals a progressive growth of the oxide from the *piranhia* cleaning step to the H_2 plasma process. According to the XPS data, there is considerable growth of the oxide layer resulting from the H_2 plasma etch process. This is evident from probing the rise in intensity of the Si 2p peak associated with Si in SiO_X at 103.55 eV. The peak at 99.77 eV corresponds to Si in SiO_X [74]. After H_2 plasma treatment, the Si peak due to Si in SiO_X shifts by 0.78 eV to higher binding energies (104.33 eV). This is tentatively assigned to the formation of a SiO_x layer with a different oxidation state. However, due to the broad nature SiO_X peak at 104.33 eV after H_2 plasma treatment, and the resolution limitations imposed by the x-ray source, it is not possible to accurately discern which oxidation state is formed.

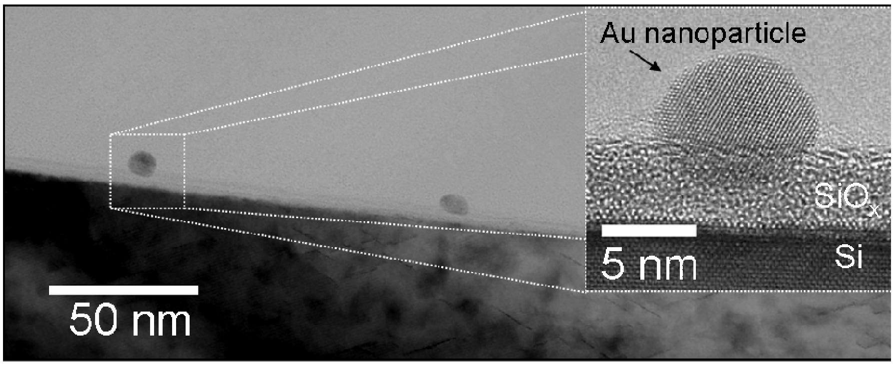

Figure 4.1-6: TEM image of Au/SiO_x/Si conformation. Inset shows an HRTEM image of a Au nanoparticle partially embedded in the amorphous SiO_x layer.

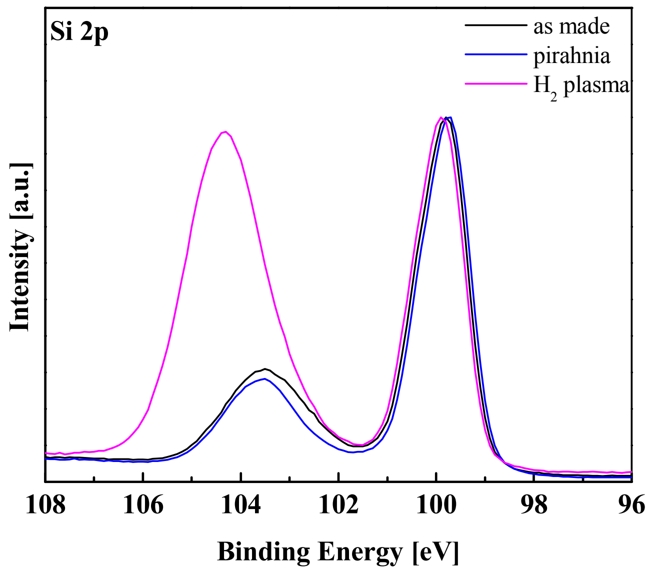

Figure 4.1-7: **Si 2p core level spectrum showing the evolution of the SiO_x layer with sample treatment. This is monitored via the Si oxidic peak at 103.55 eV, which shifts to 104.33 eV after H_2 plasma treatment.**

4.1.3 Summary

With respect to thermal stability, XPS analysis shows that 20 nm Au nanoparticles can withstand heat treatment till 750°C and at 800°C, they evaporate completely. This is indicated by the loss of the Au 4f signal at 800°C. The presence of pores rather than Au nanoparticles also confirms this point. The quasi hexagonal order of the pores indicates a reluctance of the Au nanoparticles to migrate. This is attributed to the embedded nature of the Au nanoparticles in the SiO_x layer of the underlying substrate. This is good for the intended application because the nanoparticle arrangement is maintained and this prevents a loss of size control by hampering nanoparticle fusion (Ostwald ripening).

With much credit attributed to the Au/SiO_x/Si conformation, the observations till now have earned Au nanoparticles prepared by diblock copolymer micelle nanolithography unquestionable qualification in 1-D material synthetic processes. The truth of the matter is, for such synthetic processes, low temperatures ($T < 500$°C) are preferable for industrial, environmental and economical reasons. So fear of Au nanoparticles being lost at critical elevated temperatures may be discarded. However, based on the observations recounted thus far, it is clear that the substrate is bound to play a very distinctive role on the performance of the Au nanoparticles in the Si 1-D structure growth processes.

In the forthcoming sections, the factors that influence Si 1-D structure growth in the systems described in this work, will be further elaborated upon. A filtration of what factors influence or dominate the outcome of a specific Si 1-D structure are be discussed.

4.2 Si 1-Dimensional (1-D) Material Growth

Si 1-D structures can be synthesized following approaches such as: catalyst mediated growth, which usually involves the use of a metal catalyst that serves as a nucleation site [14, 66, 75-79]. Alternatively, growth may be catalyst free i.e., the source material may be directly used to nucleate growth. This has recently been beautifully demonstrated in the hydrothermal synthesis of a novel material, Si nanotubes (SiNTs).

In most cases, Si 1-D growth is carried out following catalyst mediated methods. This is due to the fact that the catalysts employed do not only act as nucleation sites to seed growth but they also control the diameter as well as location of Si 1-D materials on a substrate [18].

On the other hand, catalyst free synthesis of Si 1-D material, as performed by Tang *et al.* was based on a self-assembly technique [66]. The problem with such methods is that the control of 1-D material diameter becomes a rather tricky procedure and is not as straight-forward as when metal catalyst seeds are employed. However, the advantage with catalyst free Si 1-D growth techniques, as is the case with the synthesis of other 1-D materials through this route, is that, the intrinsic properties of the material can be studied The presence of catalysts in the 1-D material systems are usually considered as impurities, which perturb the intrinsic properties of 1-D materials like Si. In any case, the implementation of nanoparticles as catalyst seeds is very important for devices that require nanomaterials to assume pre-patterned configurations. As mentioned in section 2.3-4, interesting size driven manifestations arise in nanomaterials such as Si due to quantum confinement effects [80, 81]. Hence, control over the diameter of Si 1-D structures is important in order to better tune device functionality and exploit these quantum effects precisely.

Si 1-D material growth in this work employs the use of Au nanoparticle seeds prepared by diblock copolymer micelle nanolithography. Section 4.1-2 shows that the Au nanoparticles are located within the SiO_x on the SiO_x/Si matrix. This already indicates that the properties of the matrix will have great impact on those of a Au nanoparticle within its vicinity. Consequently, this will also strongly influence the outcome of a Si 1-D material growth process.

4.2.1 Influence of Substrate on Seed Layer Performance

Most catalyst mediated Si 1-D growth processes involves the use of droplets induced by the breaking up (or annealing) of thin films at high temperatures [82]. Such thin film systems support the use of hydrogen terminated Si surfaces in order to promote the formation of a Au-Si eutectic phase, which is crucial for Si 1-D growth [14]. In the presence of SiO_x, Si 1-D material growth, if at all possible, is usually achieved at exceptionally high temperatures [82]. For this reason, Si 1-D growth on amorphous substrates such as glass becomes a rather tricky process. This is because glass has a low thermal stability in comparison to most crystalline substrates such as Si. The poor activity of thin film droplets on oxide surfaces such as glass during Si 1-D growth present a major setback in contemporary technology quests – the need to transfer technology to cheaper materials e.g. amorphous substrates like glass and plastic.

By contrast, when nanoparticles are used instead of thin film droplets, several advantages arise:

- Nanoparticles do not need to undergo annealing steps before Si 1-D growth. This implies high temperature annealing steps can be discarded.
- Nanoparticles have lower melting points due to size driven effects (discussed in section 2.3-3). This means, reactions in a molten particle can be performed at lower temperatures.
- Au nanoparticles show enhanced catalytic activity when on oxide substrates [56, 83]. Hence, they can readily promote Si 1-D growth on oxide substrates.

All these factors motivate the use of Au nanoparticles on oxide substrates

This section illustrates the impact of an underlying substrate on Si 1-D structure growth. Three systems are considered; Si, SiO_x/Si and borosilicate glass substrates. The discrepant thermo-mechanical properties of the substrates are exploited in order to selectively drive growth processes, which alter the structure and (or) morphology of Si 1-D materials.

4.2.1.1 The Au/Si System

4.2.1.1.1 Motivation

The Au/Si system was chosen to promote vertical aligned growth. This idea is based on the diameter dependent orientation of Si 1-D structures [56]. One of the typical crystallographic growth directions of Si 1-D structures below a critical diameter of 40 nm is <110> [56]. Growth where most Si 1-D structures are vertically aligned is typically achieved by bringing the catalytic nanoparticles in direct contact with a substrate of appropriate crystallographic orientation [14, 15].

4.2.1.1.2 Si 1-D Growth on Au/Si

i) Growth at 320°C from approximately 12 nm gold Nanoparticles

The growth of Si 1-D structures directly on a Si surface is enabled by performing a CF_4 plasma etch procedure in order to remove the SiO_x layer under high vacuum conditions. This prevents re-oxidation of the surface and ensures direct contact of Au nanoparticles with the underlying Si substrate. The misfortune of this process lies in the loss of Au nanoparticles. As a result, the overall density of Si 1-D structures obtained is less than that initially intended. Nevertheless, the Si 1-D structures obtained are sufficient to probe the influence of a Si substrate on Si 1-D growth. Figure 4.2-1 shows an SEM micrograph (45° tilted view) of Si 1-D structures grown on an etched Si surface at 320°C.

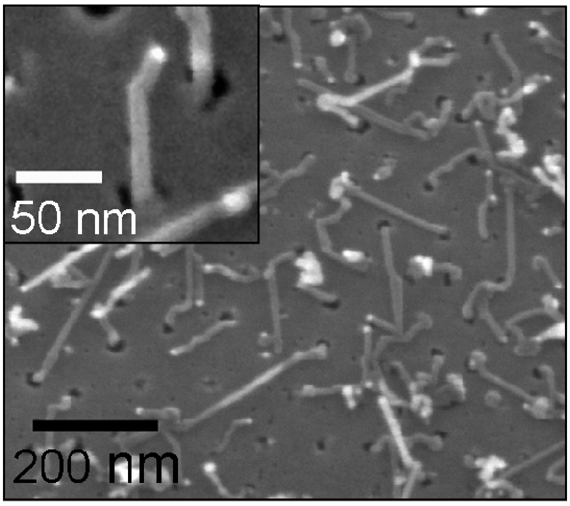

Figure 4.2-1: **SEM micrograph of Si 1-D structures on an etched Si substrate grown at 320°C. Si 1-D structures are ~ 12 nm in diameter and 150 to 200 nm in length. The inset shows a Si 1-D structure that has grown out of a nanopore in the Si substrate. A Au nanoparticle at the tip of the Si 1-D structure is indicative of a tip growth mode.**

The Si 1-D structures are ~ 12 nm in diameter, have lengths ranging between 80 – 200 nm, and grow mainly parallel to the substrate surface. The inset shows a Si 1-D structure that has grown out of a nanopore in the Si substrate in vertical orientation. The Au nanoparticle located at the tip of the Si 1-D structure is indicative for a tip growth mode.

ii) Growth at 420°C from approximately 14 nm Gold Nanoparticles

The growth rate of Si 1-D structures on Si substrates increases with temperature. Also, the tip growth mode previously observed for growth at 320°C prevails. For brevity purposes, only one temperature is demonstrated in figure 4.2-2. The Si 1-D structures are ~ 14 nm in diameter and 1.2 μm in length. The Si 1-D structures are mainly vertically aligned although they appear somewhat disordered in the SEM micrograph. This is due to the wavering of the Si 1-D structures - a factor instigated by Coulomb interactions caused by the electron beam, rendering imaging vertically aligned structures difficult.

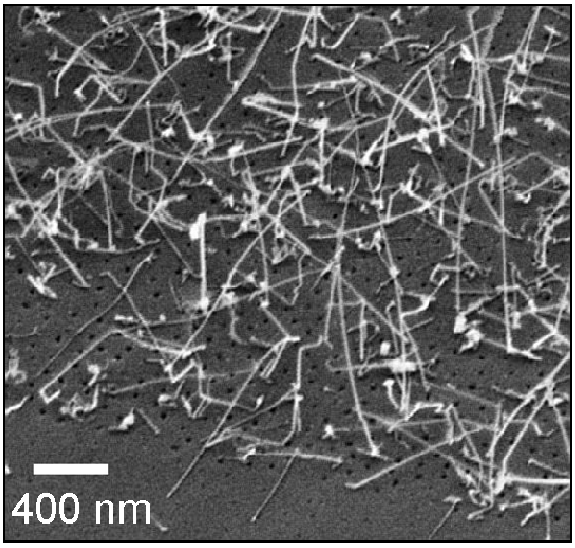

Figure 4.2-2: SEM micrograph (45° tilt) of Si 1-D structures with diameters of ~ 14 nm and ~ 1.2 µm in length, grown on an etched Si surface at 420°C.The structures are mainly vertically aligned but waver due to coulomb interaction between them, instigated by the electron beam during imaging.

4.2.1.2 The Au/SiO_x/Si System

4.2.1.2.1 Motivation

The Au-nanoparticle/SiO_x/Si system is interesting because Si 1-D growth in Au-film/SiO_x/Si systems is problematic for reasons stated earlier in section 4.2-1. Also, the catalytic activity of Au nanoparticles is known to be particularly enhanced on oxide substrates [55]. The location of the Au nanoparticles with respect to the SiO_x/Si (figure 4.1-6) indicates that any physical changes in the physical state of the SiO_x layer will affect the Au nanoparticles. This is because Au has a higher expansivity than SiO_x and can encounter compressive stress induced by the substrate upon expansion at high temperatures. Clearly, this will affect a Si 1-D growth process.

4.2.1.2.2 Si 1-D Growth on Au/SiO_x/Si

i) Growth at 320°C from approximately 12 nm Au Nanoparticles

The growth of Si 1-D structures on SiO_x/Si at 320°C is depicted in the SEM micrographs in figure 4.2-3. The structures are typically 12 nm in diameter with lengths ranging between 70 – 110 nm. The morphology is a mixture of quasi vertically oriented, as well as curly Si 1-D structures. The Si 1-D structures grow selectively from Au nanoparticle seeds. The inset in figure 4.2-3b shows a vertically aligned Si 1-D structure without a Au nanoparticle at its tip, indicating a root growth mode. The temperature implemented in the growth procedure is well below the thermal fragmentation temperature of the feed gas, SiH_4 (approximately 420°C). This implies that growth is mainly catalyst mediated and highly selective. As a result, side deposition of source material, which is on of the setbacks of CVD processes is prohibited.

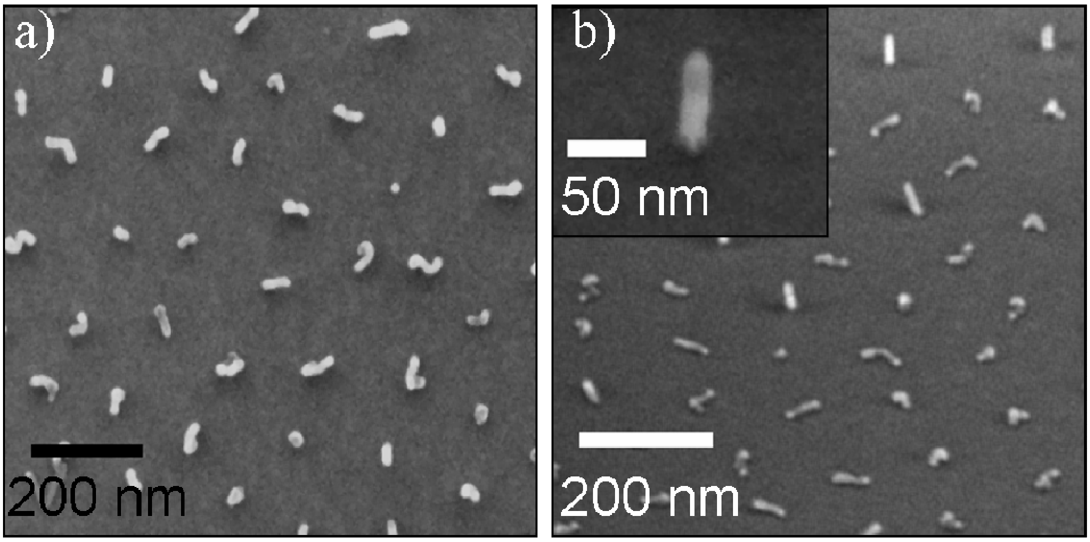

Figure 4.2-3: SEM micrographs showing (a) the top view and (b) a tilted view of Si 1-D structures grown on SiO_x/Si substrates. The structures are ~ 12 - 14 nm in diameter and have lengths ranging between 70 – 110 nm. The inset shows a vertically aligned Si 1-D structure. The Au nanoparticle seed is not at the tip of the Si 1-D structure

ii) Effect of Temperature on Si 1-D Growth from approximately 14 nm Au Nanoparticles

The progressive elevation of growth temperature increases the growth rate of the Si 1-D structures on Au/SiO_x/Si substrates. Figure 4.2-4 summarises the events through 350°C to 480°C. The Si 1-D structures obtained for each subsequent temperature raise, show no variations in morphology. They are very long (~ 8 µm), form bundles (figure 4.2-4 a-c) and are intertwined (figure 4.2-4 d-f). The inset in figure 4.2-4e shows a sparse region on the surface, indicating the growth of a Si 1-D structure from a Au nanoparticle. This confirms a root growth mode for Si 1-D structure growth in the Au/SiO_x/Si conformation.

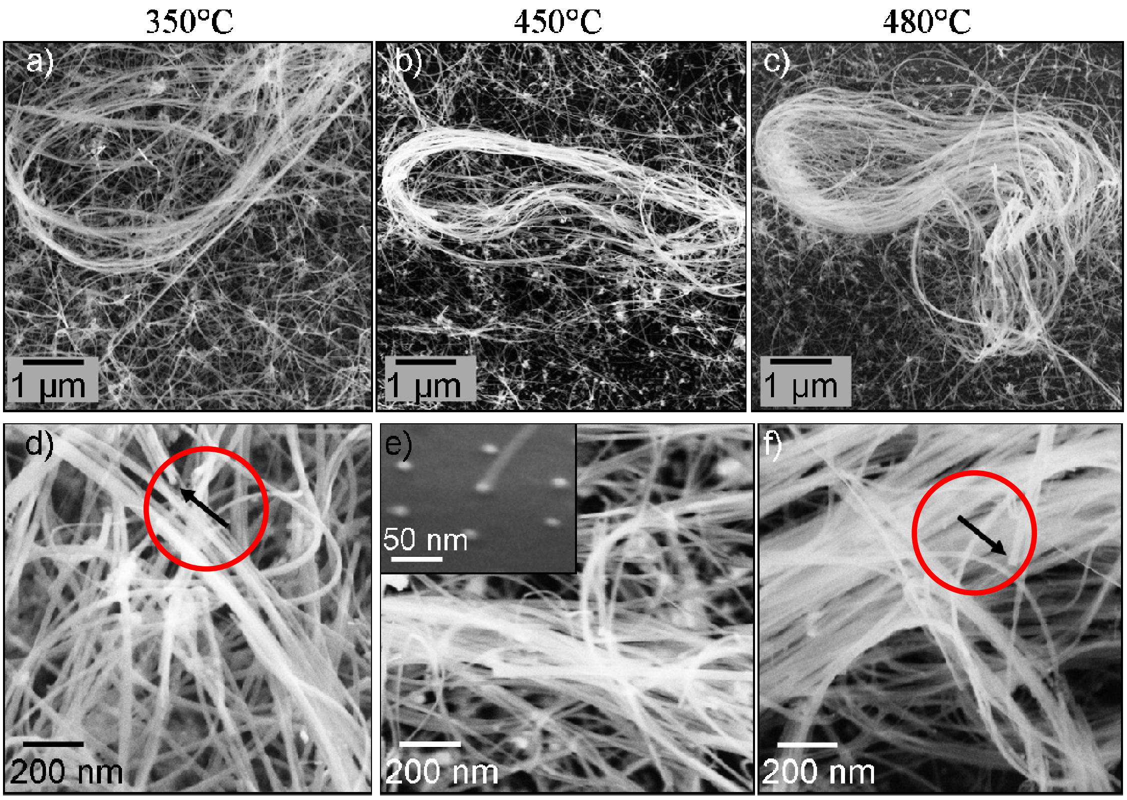

Figure 4.2-4: **SEM micrographs of Si 1-D structures grown on SiO_x/Si substrates at 350°C, 450°C and 480°C. The structures are ~ 14 nm in diameter and ~ 8 µm long. The low magnification images (a-c) show bundles of Si 1-D structures. A zoom in on the bundles (d-f) shows the intertwined nature of the Si 1-D structures. Arrows indicate tips of the structures without Au nanoparticles on them. The inset in (e) shows a sparse region indicating the growth of a Si 1-D structure from a Au nanoparticle. This confirms a root growth mode.**

The events leading to the differentiation of the growth mode of Si 1-D structures on Si and SiO_x/Si substrates are summarized in the schematic illustration in figure 4.2-5. The CF_4 process is the only factor, which deviates from the modus operandi of Si 1-D structure growth. The CF_4 etch strips off the underlying support of the Au nanoparticles and as a result, weakens the interaction between the nanoparticle and the Si substrate. The consequences for this are manifested by a tip growth mode, as well as the loss of several Au nanoparticles. The root growth mode observed in the case of Au/SiO_x/Si indicates a strong nanoparticle-substrate interaction. The SiO_x matrix anchors the Au nanoparticles, preventing migration during the high temperature processes.

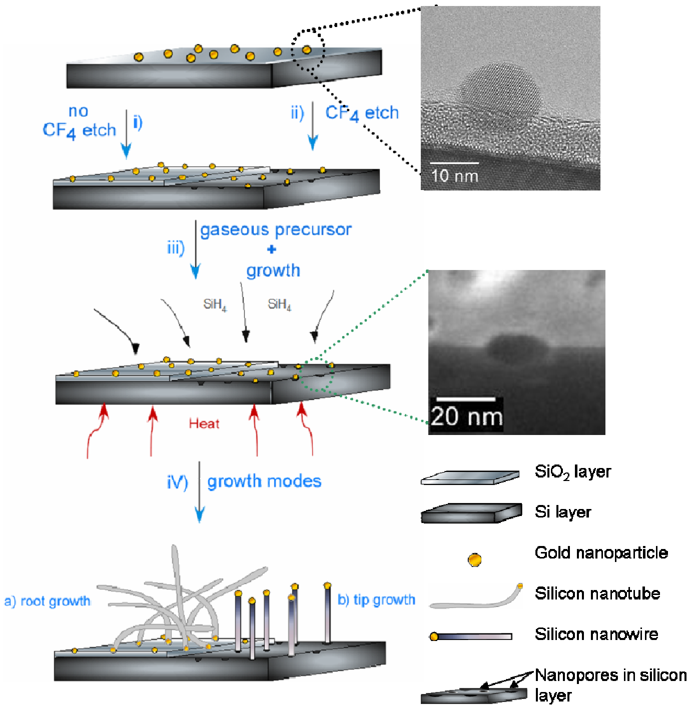

Figure 4.2-5: Schematic illustration of Si 1-D growth on Si and SiO_x/Si substrates. The modification of the modus operandi with a CF_4 etch step, alters the growth manner from root to tip growth mode.

4.2.1.3 The Au/Glass System

4.2.1.3.1 Motivation

The Au/glass system is one of particular interest because albeit glass is mainly composed of silica (SiO_x), it mingles with foreign elements, which greatly alters its thermal properties. The fact that glass softens more at much lower temperatures than crystalline substrates, permits it to be classified as a 'low' temperature substrate alongside materials as plastics. This aspect however, has rendered the growth of Si 1-D structures on glass rather problematic due to the high temperatures involved during thin film catalyst annealing processes. Therefore, the low melting temperature of Au nanoparticles can be well exploited in this conformation to overcome the problems encountered with bulk materials of the same element.

A) Temperature dependence of Si 1-D Growth on Au/Glass

i) Growth at 330°C from approximately 10 nm Au Nanoparticles

The growth of Si 1-D structures on glass substrates at 330°C leads to the development worm-like structures - of about 9 nm in diameter and about 80 nm in length, - growing parallel to the glass substrate surface as depicted in figure 4.2-6. This observation is similar to that obtained for Si 1-D structure growth on Si surfaces at approximately the same temperature (figure 4.2-1). It appears, that at these low temperatures, growth along the substrate surface is preferred. The worm-like morphology of the Si 1-D structures is similar to the morphology of Si 1-D structures grown on Au/SiO_x/Si substrates in this temperature range (give temperature).

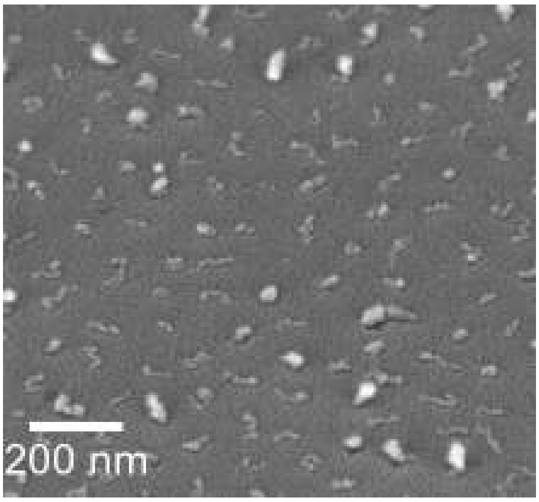

Figure 4.2-6: SEM micrograph of Si 1-D structures grown on a glass surface at 330°C. The structures are identified as worm-like in morphology with diameters of ~ 9 nm and ~ 80 nm in length.

ii) Growth at 350°C and 420°C from approximately 14 nm Au Nanoparticle

Temperature has previously been shown to be intricately involved in altering the morphology of Si 1-D structures [84]. Upon probing the temperature dependence of the morphology of the Si 1-D structures on glass substrates, one observes dramatic changes with increasing growth temperature. Figure 4.2-7 illustrates the temperature dependent morphological changes observed at 350°C and 420°C. Raising the temperature to 350°C (figure 4.2-7a) promotes the growth of Si 1-D structures almost perpendicular to the substrate with a curly morphology. This morphology already differs discrepantly from that observed at 330°C (figure 4.2-6). The lengths of the structures grown at 330°C (D ~ 9 nm; *l* ~ 80 nm) and 350° (D ~ 14 nm; *l* ~ 110 nm) do not differ considerably. However, growth performed at temperatures above 400°C (figure 4.2-7b, performed at 420°C) leads to straight Si 1-D structures. Most of them are vertically aligned with respect to the substrate, and have diameters, of D ~ 14 nm and attain lengths up to 2 µm.

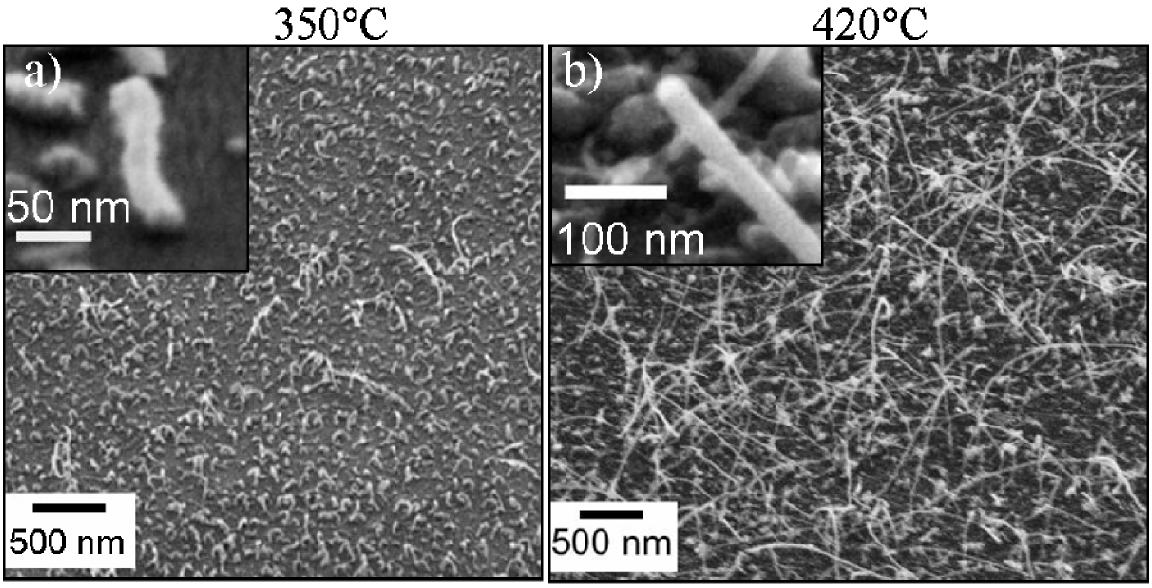

Figure 4.2-7: SEM micrographs of Si 1-D structures grown at (a) 350°C and (b) 420°C on glass substrates. The morphology of the structures changes from short (~ 100nm), curly and semi-vertical to long (~ 2µm) and vertically aligned. Coulomb interaction between the Si 1-D structures leads to them bending. The growth mode also changes from root (a) to tip growth mode (b) with increase in temperature.

These results are in compliance with previous observations where a straight Si 1-D structure, as well as an increase in their growth rate is observed with rise in growth temperature [84]. Furthermore, the crystalline quality of Si 1-D and bulk material improves with increase in temperature [84]. This may be the reason for the enhanced alignment of the Si 1-D structures. The inset in 4.2-7a shows a Si 1-D structure grown at 350°C without a Au nanoparticle at its tip indicating root growth. Contrary to this, the Si 1-D structures grown at 420°C manifest a tip growth mode as illustrated by figure 4.2-7b (another sample grown under same conditions). This is a strong indication of variants in nanoparticle-substrate interaction with increase in temperature.

The growth rate of Si 1-D structures increases with temperature. The transition from root to tip growth mode is attributed to an expansion of the glass surface upon heating that weakens the grip of the substrate on the nanoparticles. As a consequence, the nanoparticle can easily detach itself from the substrate and prompt a tip growth mode.

The morphology, orientation and growth mode of Si 1-D structures on glass substrates can be tuned by temperature. Imaging vertically aligned Si 1-D structures was again problematic as previously observed for Si 1-D structures of the same size grown on Si substrates (figure 4.2-2). This is due to electrostatic coulomb interactions between the Si 1-D structures. Altering the accelerating voltage of the electron beam did not hinder the bending of the Si 1-D structures.

4.3 Influence of Substrate on the Structure of Si 1-D Materials

The heretofore-presented results indicate the evident influence of an underlying substrate on the growth mode of Si 1-D structures. For a nanoparticle to be *held* in place by its underlying substrate, some degree of compressive stress must be acting on the nanoparticle. The stress will in turn influence the diffusion processes at the Au nanoparticle site during growth. Stress will increase or decrease depending on the rate of expansivity of the surrounding matrix with respect to the Au nanoparticle. Hence, should the expansion of the surrounding matrix be very minimal in comparison to that of the Au nanoparticle, a triaxial stress will arise in the system, which dictates, what diffusion processes will dominate during a Si 1-D growth i.e., whether supersaturation of Si material occurs within or on the surface of the Au nanoparticle.

In this light, two main diffusion processes shall be defined with respect to the Au nanoparticle:

- Bulk diffusion: penetration of Si material mainly into the interior of the Au nanoparticle.
- Surface diffusion: surface sedimentation of Si material on a Au nanoparticle.

Before a growth process, the ground state of a nanoparticle needs to be considered in order to trace and correctly interpret the magnitude of change in a system which influences other externally incorporated processes such as diffusion of foreign materials.

4.3.1 Tracking Substrate-induced Stress / Strain in Gold Nanoparticles

When Au nanoparticles are prepared by micelle nanolithography, using pyridine, they are fashioned as a result of probable complexation between the gold particles and pyridine units, which reside in the core of the micelles [61]. When, in plasma, the Au-compound-complex is reduced to elemental Au, several little nanoparticles fuse to form one nanoparticle and *attach* themselves to the underlying substrate. Therefore, one expects to obtain polycrystalline Au nanoparticles. This is evidenced from the multiple Au diffraction peaks in the X-ray diffraction (XRD) pattern (figure 4.3-1), which correspond to the powder diffraction file **(PDF)** card of Au (**4-784**) (FCC metallic gold). The additional unlabelled peaks originate from the underlying substrates (α-Al_2O_3 and SiO_x/Si).

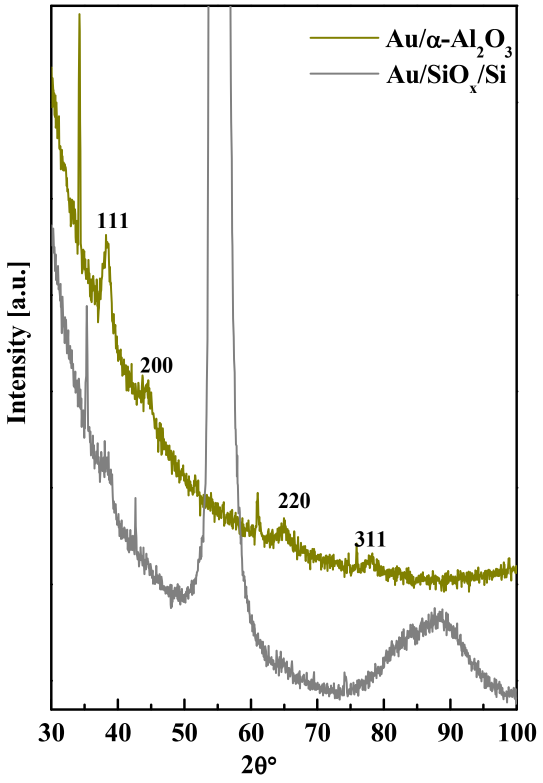

Fgure 4.3-1: XRD pattern of ~ 14 nm Au nanoparticles on SiO_x/Si and α-Al_2O_3 substrates taken at grazing angle of incidence. The labelled peaks are assigned to Au diffractions. The presence of multiple peaks is an indication of the polycrystalline nature of the Au nanoparticles. The unlabelled peaks in both cases come from the underlying substrate.

The origin of the compressive stress that arises early in a nanoparticle formation process is usually attributed to the action of surface and/ or interface stress [85, 86]. The source of the idea lies in the observation that the lattice spacing in a very small isolated crystallite is smaller than the spacing in a bulk crystal of the same material at the same temperature [87]. The lattice constant values obtained from fitting the diffraction pattern are summarised in table 4.3-1. Only the (111) reflection in the Au/SiO_x/Si system could be fitted. This is due to the very low intensity of the diffraction peaks and a poor peak-to-background ratio obtained from the specimen.

Lattice constant, a [Å]		
Reflections	**Specimen**	
	Au/α-Al_2O_3	Au/SiO_x/Si
111	4.061	
200	4.080	4.054
220	4.059	

Table 4.3–1: Lattice constant, a of Au nanoparticles on α-Al_2O_3 and SiO_x/Si surfaces.

The estimated error of the individual lattice constant results is about ± 0.02 Å. This is a large value and results from the low intensity of the diffraction peaks. The reference value taken for the lattice constant of Au, a = 4.0786 Å (PDF card 4-784). Thus no significant discripancies in the lattice constant values for nanoparticles and the bulk material can be determined at this point.

Stress in a nanoparticle can also originate from its interaction with the underlying substrate. To understand the degree of stress a substrate can impose on a nanoparticle, it is necessary to initially consider what processes occur in the development of the nanoparticle. When a nanoparticle is growing, crystallites forming on the growth surface (substrate) become firmly *attached* to the substrate at an early stage of their growth. Upon further growth in volume of the cluster, the internal elastic strain in the crystallites tends to relax because the surface radius becomes larger and the corresponding internal stress becomes smaller. However, the cluster is prevented from such relaxation due to the constraint of the substrate at a certain radius, R^*. This is because as the crystallite continues to grow, the strain is prevented from relaxing because it is subjected to a mismatch strain by the substrate. The remaining strain is balanced by surface stress, but the mismatch strain is unbalanced within the grain itself [87]. This is then transferred to the substrate through tractions across the nanoparticle-substrate interface. Laugier initially proposed this mechanism in 1981 [87].

Although the lattice constant values obtained do not show any major descripancy with the lattice contant of bulk Au, the presence of stress in the Au-substrate systems (Au/Si, Au/SiO_x/Si and Au/glass) is not discarded due to the fact that the Au nanoparticles are in contact (Au/Si), as well as strongly interacting (Au/SiO_x/Si and Au/glass) with the substrate. Hence, strain due to a lattice mismatch between the nanoparticle and the substrate should be expected even though its magnitude is not represented in the results obtained here. In section 4.3-2, the presence of a substrate induced stress is illustrated.

4.3.2 Influence of Substrate-Induced Stress on Si Diffusion in to a Gold Nanoparticle

When materials with positive expansion coefficients α_T are heated, they expand. If two materials in contact with one another, which have mismatches in thermal expansivity, are heated, their expansion rates are not syncronized. If a material with a high α_T is situated in a material with a lower α_T, the material with a higher α_T is bound to sense compressive strain upon expansion when heated. This is because the surrounding matrix expands slower, and does not respond linearly to the expansion of the material with a higher α_T within it. Table 4.3-2 summarises the linear thermal expansion coefficients, α_T (T = 20°C) of all the materials discussed. Au has the highest α_T value amongst all materials in question. Si and glass have α_T values of approximately the same order of magnitude, while SiO_x has the least α_T value. This implies that the SiO_x matrix expands least upon heating and exerts a firmer grip on the Au nanoparticle. As a result, the nanoparticle remains *captive* to the SiO_x substrate, while the glass substrate exerts less compressive strain on the Au nanoparticle, and hence, weakening the SiO_x nanoparticle-substrate interaction during expansion (at 420°C) (section 4.2.3.1). As for the third case, the interaction is initially weakened by the CF_4 etch process which strips off the SiO_x support beneath the Au nanoparticle leaving it in a more of *touch* rather than incorporated position with respect to the Si substrate.

Material	**Thermal expansion coefficient α_T [K^{-1}]**	
	20 - 300°C	300 - 500°C
Au	14×10^{-6}	
Si	$2.63 - 3.84 \times 10^{-6}$	$3.84 – 4.07 \times 10^{-6}$
Silica	0.59×10^{-6}	0.54×10^{-6}
Borosilicate glass*	$7.3 - 7.4 \times 10^{-6}$	

*** purchased from Karl Roth GmbH, Karlsruhe.**

Table 4.3–2: Temperature-dependent linear thermal expansion coefficients [α_T].

4.3.2.1 Si 1-D Structures obtained on Au/Si Substrates

SEM micrographs (figure. 4.2-1) reveal that the growth of Si 1-D structures on Si substrates leads to a tip growth mechanism. HRTEM analysis (figure. 4.3-2) depicts a SiNW structural configuration for growth performed at 420°C. The acquired SiNW structure is assigned to dominant bulk diffusion of Si from the underlying substrate during Au-Si eutectic formation as well as from the feed gas (SiH_4). Bulk diffusion is accounted for by the minimal interaction between the Au nanoparticles and the underlying/surrounding Si substrate after the SiO_x surface is stripped off by the CF_4 etch process. Hence, the Au nanoparticle can expand under very minimal strain upon heating and incorporate Si atoms into its lattice. Figure 4-3-3 is a schematic illustration of the described processes. It is presumed that both surface and bulk diffusion processes occur during growth. However, the dominant process is what determines the outcome of the Si 1-D structure obtained.

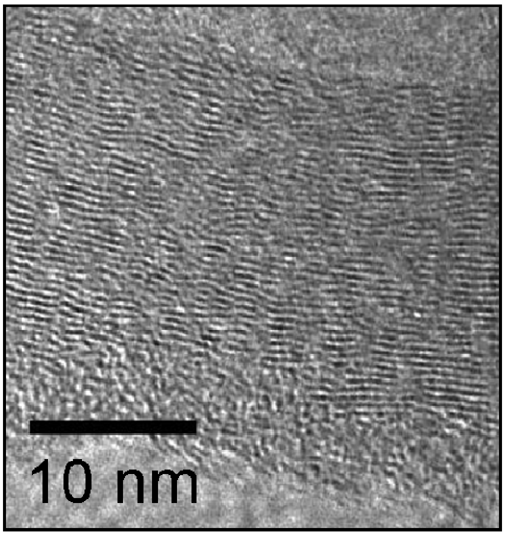

Figure 4.3-2: HRTEM image of a Si 1-D structure (d ~ 18 nm) grown on a Si substrate at 420°C.

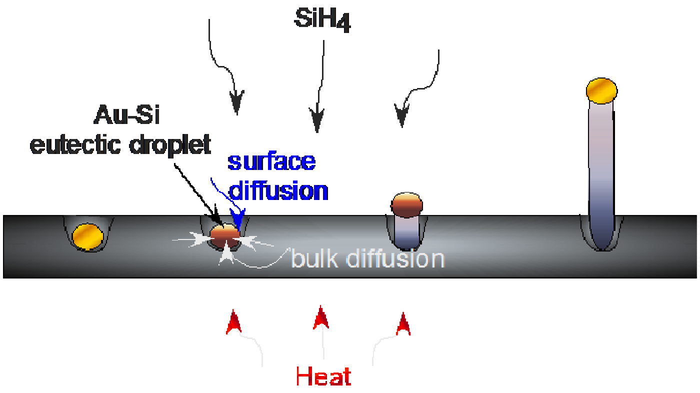

Figure 4.3-3: Schematic illustration of SiNW growth on Si surface. During growth, the Au-Si alloy develops as a result Si diffusion from the substrate into the Au nanoparticle. Si from SiH_4 fragmentation also diffuses into the Au nanoparticle. The Au nanoparticle is able to expand with little constrain due to minimized interaction with the substrate. This provides a favourable path for bulk diffusion into the nanoparticle, which leads to SiNW growth.

4.3.2.2 Si 1-D Structures obtained on Au/SiO$_x$/Si Substrates

Looking at the Au/SiO$_x$/Si system, one faces two materials with α_T values differing by two orders of magnitude. SiO$_x$ has a α_T value, which varies only very slightly with increase in temperature as shown in table 4.3-2. Figure 4.3-4 shows TEM micrographs revealing the temperature dependent variance in structure of the Si 1-D structures at 350°C, 450°C and 480°C on Au/SiO$_x$/Si. The Si 1-D structures observed over the different temperature ranges are typically 15 ± 4 nm in diameter. At 350°C (figure 4.3-4a), the Si 1-D structures are tubular in nature. This is depicted from the contrast between the outer and inner walls of the Si 1-D structure as well as the discontinuity in crystal lattice in the interior of the SiNT as depicted in the HRTEM inset (4.3-4a). The structures look similar to those observed for self assembled SiNTs [17] with the SiNTs having a closed end. This closed end has several defects and has been assigned to an energy minimization process during SiNT formation [17].

The absence of Au nanoparticles at the tips of the SiNTs, confirms the root growth mode asserted earlier in section 4.1.2.1 (figure 4.2-4). At 450°C (4.3-4b/c), SiNWs are found to coexist with SiNTs. Also, tip and root growth modes coexist in the system. At 480°C (figure 4.3-4d), mainly SiNWs and no SiNTs are observed. This is seen in the HRTEM inset (4.3-4b) from the continuity of the crystal lattice without any abrupt disruption as observed for SiNTs. The substrate expansion at this temperature is however not enough to release the Au nanoparticles. This is seen from the Au free SiNW tips in figure 4.3-4d. A mixture of tip and root growth modes has also been observed at this temperature (not shown). This indicates the non-uniform expansion of the SiO$_x$ matrix i.e. not all Au nanoparticles sense a relief from the *grip* of the substrate-induced compressive strain. From table 4.3-2, it is evident that the expansion of the SiO$_x$ matrix is quite minimal at 450°C and 480°C compared to its expansion at 350°C. This implies another factor initiating the formation of SiNWs is the increase in diffusion rate with increase in temperature [88]. In addition, the small size of nanoparticles play a vital role in lowering the diffusion activation energy of Si atoms due to an increase in surface (interface)/volume ratio.

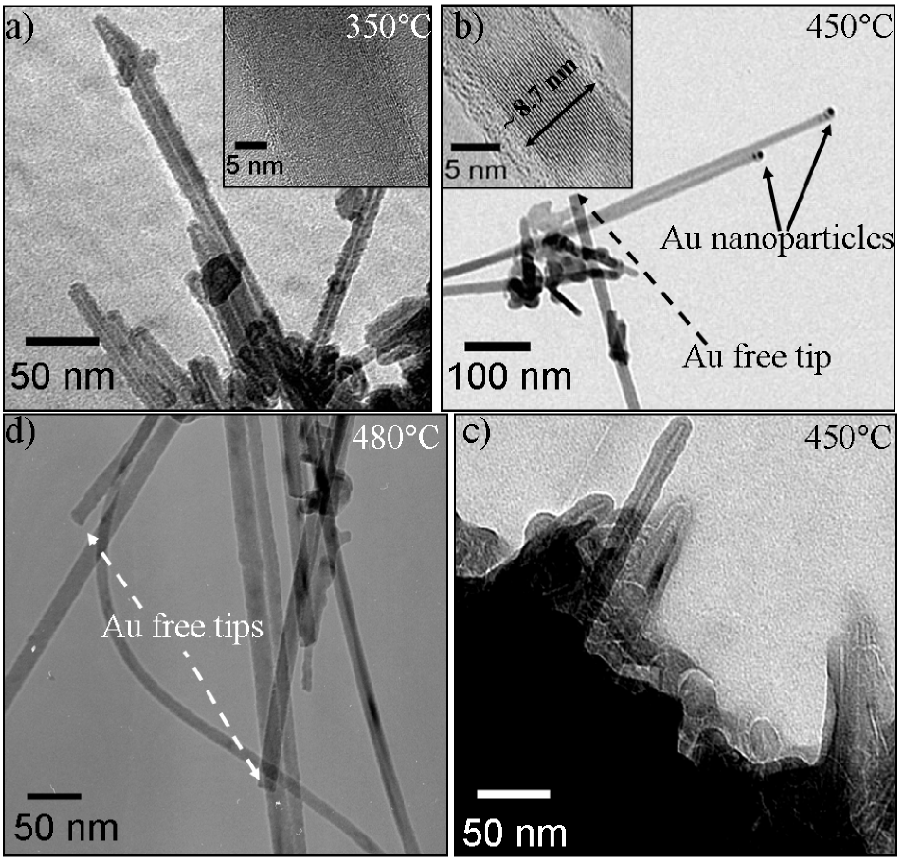

Figure 4.3-4: **TEM images of Si 1-D structures grown on SiO_x/Si substrates, yielding (a) SiNTs at 350°C (b-c), a mixture of SiNWs and SiNTs at 450°C and(d) SiNWs at 480°C The SiNTs are closed at the tip and do not show the presence of a Au nanoparticle. In the cases of the SiNWs, there are Si 1-D structures with and without Au nanoparticles at the tips, indicating a mixture of growth modes on the surface. The insets show HRTEM images of (a) a SiNT and, (b) SiNW. The distinguishing factor between these structures is the discontinuity in crystal lattice in the interior of the Si 1-D structure in the case of a SiNT while in SiNWs the crystal lattice this discontinuity is absent.**

Nevertheless, with increase in temperature, the SiO_x matrix is expected to considerably *give way* to the expansion of the Au nanoparticles. Also, diffusion rate is expected to rise with temperature such that, at a given critical temperature, $T_c \approx 450°C$, bulk diffusion will become favourable and dominant in the Au/SiO_x/Si system. This will in turn enable the formation of SiNWs rather than Si nanotubes (SiNTs) whose occurrence is predictably induced by the segregation of Si atoms at the Au nanoparticle surface. A schematic illustration of this proposed SiNT growth mechanism is depicted in figure 4.3-5.

This surface segregation is linked to compressive stress imposed by the substrate, which as earlier mentioned, inhibits the expansion of the Au nanoparticles during the growth process and renders Si incorporation into the Au nanoparticles difficult. This theory is simply checked by performing Si 1-D material growth at elevated temperatures and probing the structural changes that occur as clearly demonstrated in figure 4.3-4d.

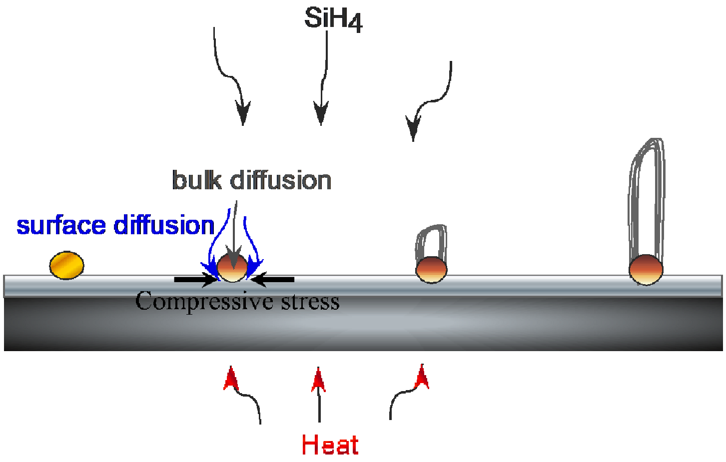

Figure 4.3-5: Schematic illustration of substrate-induced compressive stress on a Au nanoparticle. This in turn leads to a situation of dominant surface diffusion with respect to the Au nanoparticle. The induced surface sedimentation of Si promotes the formation of a SiNT.

The dual growth modes observed on the SiO_x surface at 450°C are ascribed to two main factors:

- The fact that the SiO_x matrix is amorphous and does not expand linearly or evenly upon heating. Hence the 'lines of weakness' in the substrate will vary at certain positions depending on the local expansion of the SiO_x matrix at the Au nanoparticle site.
- The non-uniform depth of the Au nanoparticles in the SiO_x matrix (figure. 4.3-6); Some Au nanoparticles are embedded at deeper levels in the SiO_x matrix than others. Thus, their stability with respect to substrate anchorage varies. Au nanoparticles with very shallow embedment will easily be liberated from the matrix and Si 1-D structures growing from such structures will manifest a tip growth mechanism. On the other hand, deep-sited Au nanoparticles will be tightly bound to the SiO_x matrix and Si 1-D structures growing from them manifest a root growth mechanism.

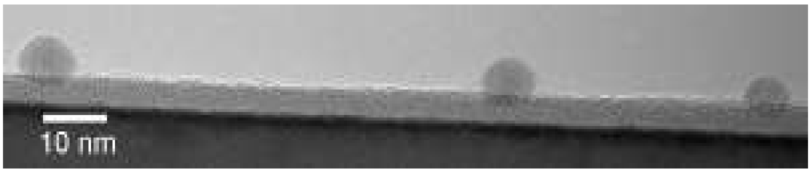

Figure 4.3-6: HRTEM image of a Au nanoparticles (d ≈ 6 – 8 nm) on a SiO_x/Si substrate. The Au nanoparticles are partially imbedded at different depths in the SiO_x matrix.

4.3.2.3 Si 1-D Structures obtained on Au/Glass Substrates

SEM micrographs (figure 4.2-7) of Si 1-D structures show a turn-over from root to tip growth mode when transiting from 350°C to 420°C. Table 4.3-2 shows that the α_T value of glass is an order of magnitude higher than that of SiO_x and of almost the same order of magnitude as Si. This implies the expansion of the glass substrate upon heating will be of a similar manner as observed in the Au/Si configuration. In other words, the degree of substrate-induced compressive stress will be minimal enough to favour expansion of the Au nanoparticle and enhance bulk diffusion. Figure 4.3-7 shows a TEM cross sectional view of vertically aligned SiNWs grown at 420°C with diameters of ~ 14 nm and lengths attaining ~ 530 nm.

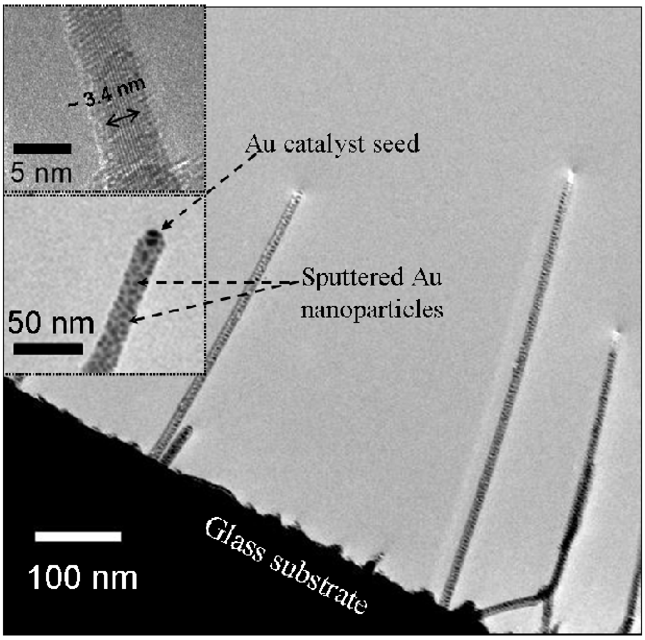

Figure 4.3-7: TEM image with cross-sectional view of vertically aligned Si 1-D structures grown at 420°C on a borosilicate glass substrate. The Si 1-D structures are approximately 10 nm in diameter with lengths up to ~ 550 nm. The upper inset shows a Au free region of a Si 1-D structure (D ~ 5 nm) with a crystalline core (D ~ 3.4 nm) and a thin external amorphous sheath. The Au nanoparticle seed which promoted Si 1-D growth is located at the tip of the Si 1-D structure (lower inset). The black spots on the Si 1-D structure are Au nanoparticles which stuck on the Si 1-D structure during the sputter coat process which was performed to render the glass surface conductive.

The structures are partially coated by Au nanoparticles resulting from a Au sputter coat process conducted to render the glass surface conductive prior to imaging. The sputtered Au nanoparticles, identifiable, as tiny black spots on the Si 1-D structure are observable in the lower inset of figure. 4.3-7. The catalytic Au nanoparticle, which promoted Si 1-D growth, can be well appreciated at the tip of the Si 1-D structure. The strong oscillations of the Si 1-D structures in the electron-beam also rendered the imaging of an entire 1-D structure tedious. The upper inset is a HRTEM micrograph illustrating a sputter coat-free region of a SiNW, about 5nm in diameter with an approximately 3.4 nm crystalline core surrounded by a thin external amorphous sheath.

4.3.3 Summary

To recapitulate, at growth temperatures below 420°C, Si 1-D structures grown from Au nanoparticles on Si and glass substrates yields SiNWs while SiO_x/Si substrates yield SiNTs. This has been tentatively assigned to the degree of compressive strain imposed by the substrate on the Au nanoparticles as they expand upon heating. For a Si atom to diffuse into a Au nanoparticle, there has to be some *space* into which it can incorporate itself. For this to be made favourable, the Au nanoparticle needs to expand. However, if this expansion is being prohibited by an external factor such as the matrix surrounding the nanoparticle, the energy barrier the Si atoms have to overcome in order to diffuse into the Au nanoparticle becomes high. As a result, a lower energy path has to be sought by the atoms. The low energy path in this case, is a surface diffusion process, which leads to the sedimentation of Si atoms on the surface of the Au nanoparticles. Subsequent saturation of Si on the Au nanoparticle surface leads to SiNT formation. Table 4.3-3 summarises the Si 1-D structures obtained for all three Au/substrate systems at different growth temperatures, (T_g,) from Au nanoparticle with diameters of ~ 14 nm. From this, a clear consequence of the thermo-mechanical properties of a substrate shows that when nanoparticles experience different degrees of compressive stress, one obtains a Si 1-D material whose morphological evolution is governed by strain-induced surface diffusion. The growth of Si 1-D structures takes place selectively at the Au nanoparticles. Obviously, the Au nanoparticles must have their own impact on the Si 1-D growth process.

T_g [°C]	**Au/Si**		**Au/SiO_x/Si**		**Au/glass**	
	Structure	**Growth mode**	**Structure**	**Growth mode**	**Structure**	**Growth mode**
350	SiNW	Tip	SiNT	Root		Root
420	SiNW	Tip	SiNT	Root	SiNW	tip
450		Tip	SiNT + SiNW	Root + Tip		
480			SiNW	Root + Tip		

Table 4.3–3: Summary of Si 1-D structures obtained on various substrates at various temperatures

4.4 Influence of Gold Nanoparticles on Si 1-D Growth – Influence of Size Effects or Impurity–

The nanaparticle effects discussed in this section apply for all substrates (Au/SiO$_x$/Si, Au/Si, Au/glass). So for brevity, discussion shall be restricted to the Au/SiO$_x$/Si, system only.

4.4.1 Impact of Size Effects

The Au-Si phase diagram (figure. 2.2-.3) indicates that a Au-Si eutectic typically forms at ~ 363°C. This temperature, however, has been scaled from the bulk melting properties of Au and Si (1064°C and 1410°C respectively). Thus, one can expect that the Au-Si eutectic temperature in systems involving small Au nanoaprticles, such as those employed in this work, would be less than that reported in a Au-Si bulk system. Si 1-D structures were synthesized under the same gas flow (40 sccm) and pressure (approx. 2 mbar) conditions. The temperature was varied in order to probe the minimal and maximal growth active temperature range for each nanoparticle size.

Figure 4.4-1 shows SEM micrographs obtained when Si-1D structure growth experiments were performed on ~ 10 nm Au nanoparticles within a temperature range of 300°C – 370°C. Below the threshold of 320°C, no growth of Si 1-D structures on Si/SiO$_x$ was observed. This is tentatively ascribed to several to several factors: presuming a liquid phase diffusion, growth may not have occurred due to the Au nanoparticle not having melted in order to enable miscibility with Si. However, Si 1-D structure growth resulting from Si diffusion into a solid phase particle has been reported [15]. Hence, a more plausible option may well be due to the fact that the threshold activation energy for growth has not been attained. At 320°C, selective Si 1-D growth from Au nanoparticles is observed. Growth is possible with Au nanoparticles of this size until ~ 350°C, above which growth is interupted (370°C) as seen figure 4.4-1d,. This implies the window within which Si 1-D structure growth can occur is very narrow for Au nanoparticles with an average diameter of 10 nm.

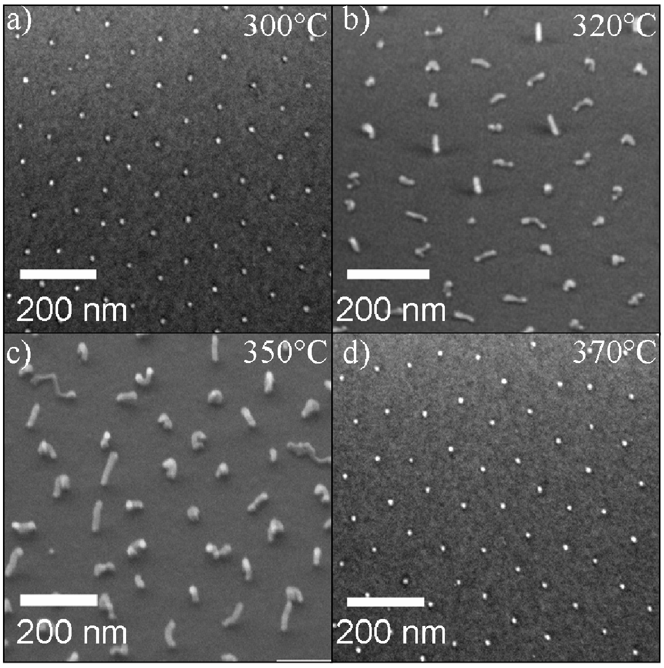

Figure 4.4-1: SEM micrographs (45° tilt) of temperature-dependent activity of 10 nm Au nanoparticles during Si 1-D growth. The threshold for activated growth is at 320°C and the deactivation temperature is 370°C.

Upon probing this phenomenon with ~ 15 nm Au nanoparticles, it becomes apparent that size effects play a vital role as concerns the lower and upper limits for Si 1-D growth. Figure 4.4-2 shows SEM micrographs of Si 1-D structures grown from Au nanoparticles with an average size of 15 nm. The minimum possible growth temperature moves up by ~ 30°C to 350°C. The window for Si 1-D growth also gets wider and extends by ~ 130°C to 480°C. Contrary to the ~ 30°C growth window obtained for 10 nm Au nanoparticles. The shift to higher growth activation temperatures may hence be attributed to differences in melting point between the 10 and 15 nm Au nanoparticles, which increase with augment in nanoparticle size.

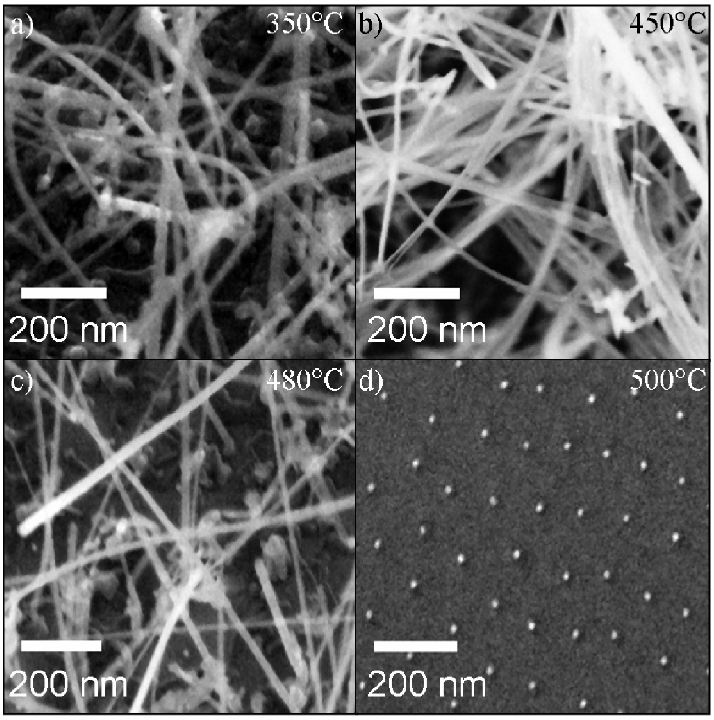

Figure 4.4-2: SEM micrographs of temperature-dependent activity of ~ 15 nm Au nanoparticles during Si 1-D growth at (a) 350°C (b) 450°C, (c) 480°C and (d) 500°C. The threshold for activated growth is at 350°C and the deactivation temperature is 480°C.

In a previous study, it has been predicted that the observed length of a Si 1-D structure may not necessarily represent the entire grown length [84]. It is presumed that the side depositon of Si source material partially embeds part of the Si 1-D structure.. This implies the length of a Si 1-D structure observed on a substrate depends on the competitive nature between catalytic and non-catalytic deposition of source material. Should the Si 1-D structure growth rate fall short of competition, the non-catalytic side deposition of material will bury part and if not, the entire Si 1-D structure. In the case of growth failure at 370°C, this can clearly not be the case because the experimental conditions are well below the thermal fragmentation temperature of SiH_4 (~ 420°C). Hence, if any growth should occur, it is mainly catalyst driven. As to side deposition of source material, if at all any occurs, it is negligible. Figure 4.4-3a shows a TEM cross sectional view of the surface confirming the absence of any Si 1-D growth. In fact, the surface looks very similar to that obtained for surfaces on which no growth was performed (figure 4.1-6). Figure 4.3-3b shows TEM a cross sectional view of the surface on which growth failed at 500°C. The TEM micrograph shows

Au nanoparticles surrounded by dark material, presumed to be Si debris resulting from the side deposition of source material. In this case again, Si 1-D growth is not observed. The Au nanoparticles are clearly still on the surface but activity has totally ceased.

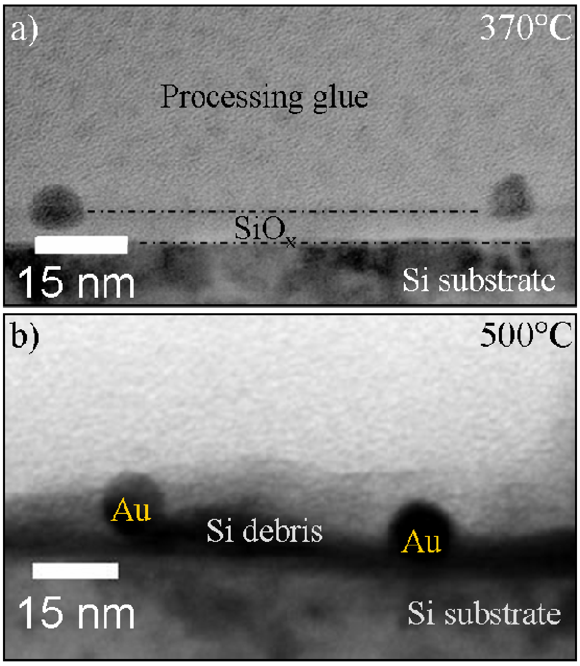

Figure 4.4-3: **TEM micrographs of 10 nm and 15 nm Au nanoparticles after Si 1-D growth failure at (a) 370°C and (b) 500°C. The absence of Si debris at the sides of the Au nanoparticles at 370°C is because this process was run at temperatures well below the fragmentation temperature of SiH_4. The Si debris at the side of the Au nanoparticles after growth failure at 500°C indicates the side deposition of thermally fragmented SiH_4 molecules. Yet, no Si 1-D structure growth is observed in either case**

A monitor of the size distribution of the Au nanoparticles before and after growth reveals only minor changes (figure 4.4-4). There is barely a definite reduction in size of the 10 nm Au nanoparticles while the 15 nm Au nanoparticles show a main population distribution shift in size from 15 to about 13 nm. In both cases, the size distribution broadens after growth failure. This is assigned to uneven evaporation of Au upon heating which leads to nanoparticle size variations. Variations in upper and lower Au nanoparticle size,limits result from the fact that nanoparticle analysis was performed at different areas on the sample before and after growth.

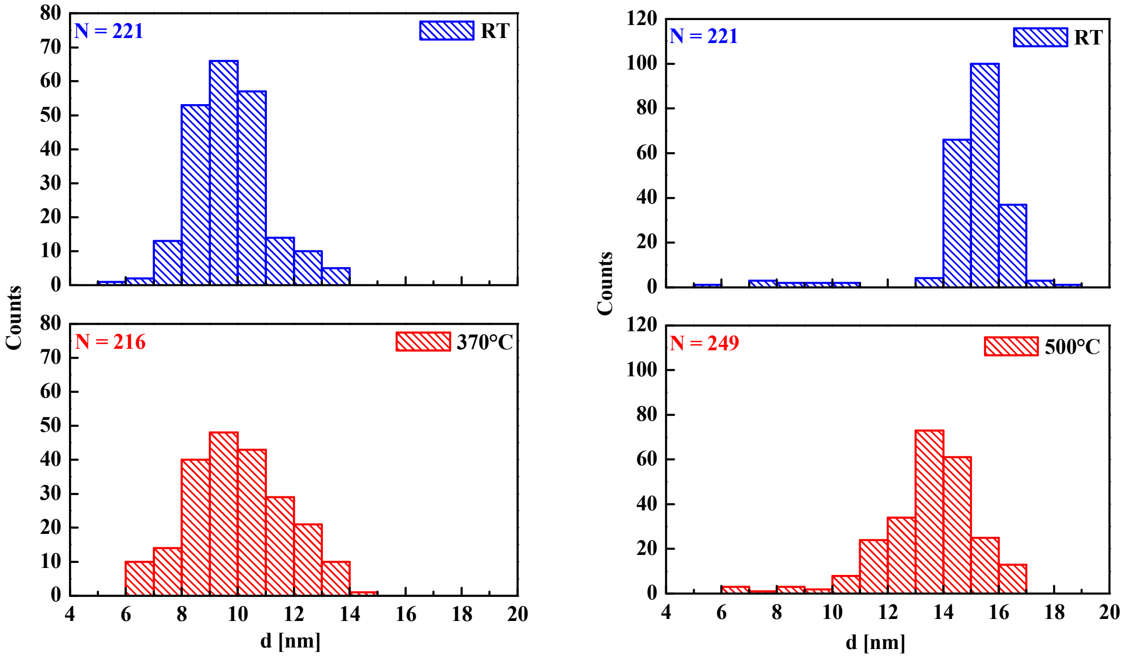

Figure 4.4-4: **Size distribution of Au nanoparticles before (room temperature –RT) and after Si 1-D growth failure at 370°C (left) and 500°C (right). In both cases, a broadening in size distribution is observed after growth failure. This is assigned to uneven evaporation of Au material upon heating which results in nanoparticles size variations. Variations in upper and lower Au nanoparticle size limits result from the fact that nanoparticle analysis was performed at different areas on the sample before and after growth.**

During a nanoparticle dip-coat process, the surface at the edges of a sample is usually made up of larger Au nanoparticles with a broad size distribution and very short-range quasi hexagonal order. This is due to the formation of several micelle monolayers resulting from solution accumulation. During the plasma process, the Au nanoparticles fuse to form larger nanoparticles. The edges give further revelations on the size-dependent scaling of Au nanoparticle catalytic activity as a function of temperature. Figure 4.4-5 shows a SEM micrograph of one of the edges of a Si wafer surface after growth was attempted at 550°C using ~ 10 nm Au nanoparticles. Growth of SiNWs with diameters ranging between 40 – 200 nm has occurred only at the edge of the wafer while the main body of the sample (lower inset) is buried with just mould-like structures observable. This is because the nanoparticle activity has come to a halt. Hence, raising the growth temperature does not promote Si 1-D growth from small Au nanoparticles but rather, enhances non-catalytic deposition of Si source material, which buries the Au nanoparticles. Larger Au nanoparticles at the wafer edge are still within their catalytically active range and promote Si 1-D growth at temperatures (≥ 490°C) similar to those typically used in systems where Au thin films are employed as catalyst [14].

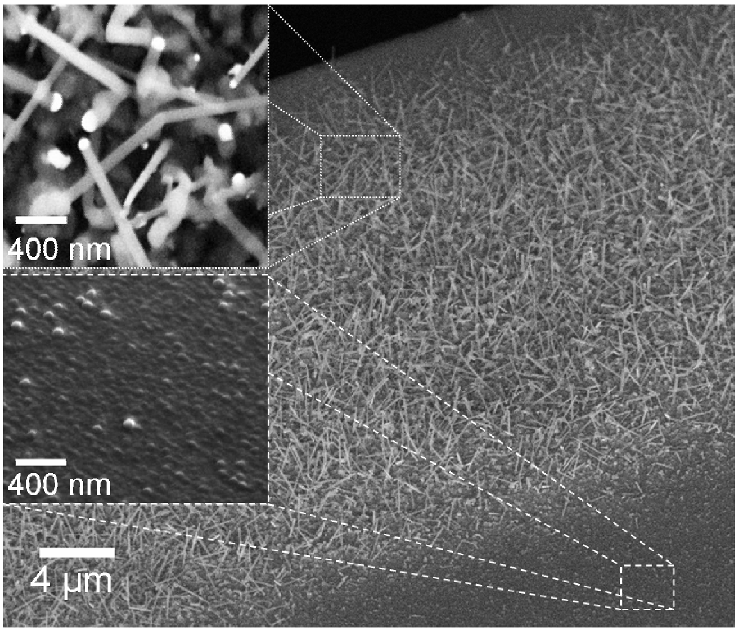

Figure 4.4-5: SEM micrograph (45° tilt) of a Si wafer edge after a Si 1-D growth experiment at 550°C. SiNWs with diameters ranging from 40 – 200 nm are observable at the edges of the wafer. Mould-like structures resultant from Au nanoparticles being concealed by non-catalytic side deposition of Si source material.

4.4.2 Impurity Effects

As mentioned in section 2.2.3, the melting point of Au nanoparticles decreases with diminishing nanoparticle size [50]. This phenomenon results from the fact that surface effects become more significant with size downscaling due to an increase in surface/ volume ratio with respect to the atoms. The atoms at the surface of a nanoparticle are less stable than those in the interior because of their low coordination number. This implies that less energy is required to break the weak bonds on the surface. Hence, if the surface area dominates the volume of the nanoparticle, then melting is bound to set in at lower temperatures than in a bulk system. This melting temperature logically scales with size because more and more surface atoms make up the bulk of the nanoparticle as its size diminishes. An increase in number of surface atoms also leads to a greater liability of their taking part in bond formation with elements from the gaseous phase.

The adulteration of a *pure* system with foreign elements is causative for changes in physical characteristics of the system. For example, carbon contamination lowers the melting point of metals such as Fe and boron alters the electronic activity in Si. Small amounts of impurities manifest themselves quite visibly in bulk systems. So the questions arising are:

- What is the situation then when foreign atoms incorporate themselves within or on a Au nanoparticle surface?
- How do these foreign elements influence the activity of a Au nanoparticle during a Si 1-D growth process?
- How does the impact of these impurities scale with Au nanoparticle size?

4.4.2.1 Role of Plasma Treatment

It is generally known, that the performance of a material strongly depends on its quality, which in turn depends the synthetic route(s) chosen. The Au nanoparticles employed in this work for Si 1-D synthesis can either be prepared using H_2 or O_2 plasma. Discussion so far has been based on Au nanoparticles prepared in a H_2 plasma environment. At this point, it is worth mentioning the findings of Lu *et al*. [83], who carried out Si 1-D growth experiments using the same nanoparticle preparation technique and same Au nanoparticle size (10 nm) as applied in this work. Whereas Lu *et al*. reported observing growth of Si 1-D structures at 550°C using Au nanoparticles prepared in O_2 plasma, this work shows that Si 1-D growth performed on Au nanoparticles (~ 10 nm) prepared in H_2 plasma halts at temperatures beneath 400°C. Also, an increase in growth temperature does not instigate Si 1-D structure formation. It is interesting to note that even larger particles (15 nm) do not promote (figure) Si 1-D growth at temperatures above 480°C. Rather, non-catalytic side deposition of the source material is observed (figure 4.4-3). In addition, no growth occured, when Si 1-D growth experiments were performed with Au nanoparticles prepared in O_2 plasma, under identical experimental conditions as those that yielded growth with H_2 plasma-treated Au nanoparticles. The surface shows no morphological differences before and after a growth attempt. This implies that the temperature dependent Au nanoparticle catalytic activity is strongly dependent on plasma treatment. Whereby, H_2 plasma-treatment promotes growth from nanoparticles at lower temperatures (T < 400°C) than O_2 plasma treatmeant (T > 550°C).

The command for higher synthesis temperatures with O_2 treated nanoparticles is tentatively assigned to the formation of an oxidised Au nanoparticle during the O_2 plasma process. The oxidised state of a Au nanoparticle consists of a crystalline Au core surrounded externally by amorphous Au_2O_3 sheath as depicted in the schematic illustration in figure 4.4-6. The external Au_2O_3 layer probably acts as a barrier, shielding the diffusion of Si atoms into the Au nanoparticle. This layer needs to be desorbed in order to enable Si diffusion into Au. In bulk systems, this layer is desorbed at temperatures between 150°C and 200°C [89]. Due to device limitations, an *in situ* monitor of Au_2O_3 formation under similar experimental conditions during the experiment was not possible. This is because the O_2 plasma pre-cleaning step was conducted on a sample heated to the reaction temperature in the growth chamber. XPS analysis on samples treated in O_2 plasma under standard conditions (section 3.1.2) did not reveal any peaks indicative of Au_2O_3. This is based on the unstable nature of Au_2O_3 [89]. Measurements to detect peaks corresponding to Au_2O_3 have only been observed on samples measured immediately after an O_2 plasma oxidation of Au nanoparticles prepared by the micelle technique employed in this work. Figure 4.4-7 shows Au 4f photoelectrons obtained from Au nanoparticles treated in H_2 and O_2 plasma compared to the 4f spectrum of bulk Au. The Au 4f peaks of the nanoparticles manifest slight shifts to higher binding energies. This may be due to the accumulation of positive charges on

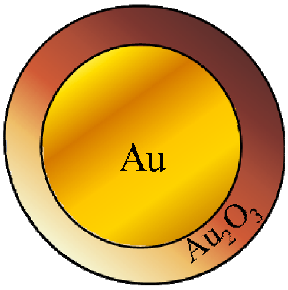

Figure 4.4-6: Schematic illustration of an oxidised Au nanoparticle with a crystalline Au core surrounded by an amorphous Au_2O_3 sheath

the nanoparticle surface and not to silicide formation because Au does not form silicides on SiO_x/Si surfaces at room temperature [90]. The temperatures employed by Lu and co-workers[83] for Si 1-D material growth are ~ 200°C well above the temperatures applied in synthesis of Si 1-D structures using H_2 treated Au nanoparticles of the same size range. This affirms the fact that the synthesis route, one chooses indeed plays a great role in engineering the properties of the resultant material.

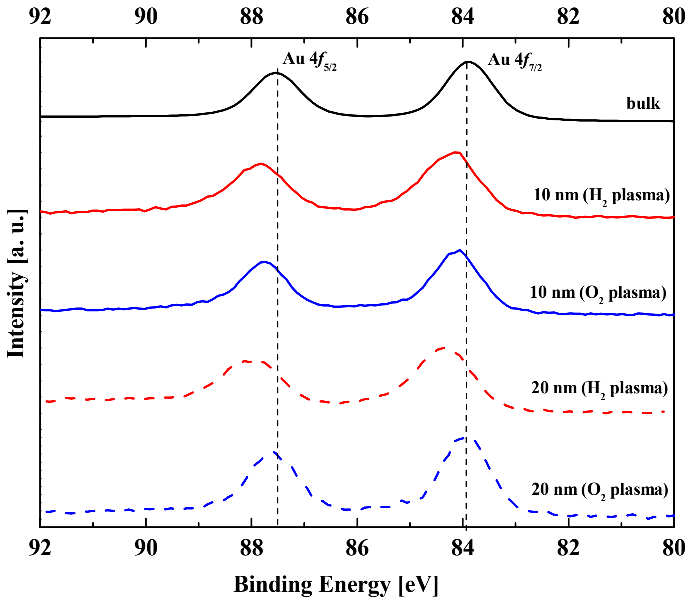

Figure 4.4-7: Au 4f core level spectra of Au nanoparticles obtained after plasma etch processes in H_2 and O_2 atmosphere compared with a bulk Au reference spectrum.

4.4.2.2 Tracking Hydrogen in Gold Nanoparticles

So far, it is evident that Au nanoparticles treated in H_2 plasma demonstrate catalytic activity at lower temperatures than Au nanoparticles of the same size, treated in O_2 plasma. This implies the nanoparticle activity at low temperatures can not be fully accounted for by size effects. The activity of the nanoparticles is independent of the substrate used. Hence, substrate effects are not responsible for this phenomenon. Therefore, the enhanced activity is probably due to the presence of hydrogen impurity in the Au nanoparticles. Until now, the following is known:

- There exists a certain critical growth temperature, T^*, at which the Au nanoparticles traverse from a catalytically active to a passive state. Further increase in temperature does not promote Si 1-D growth.
- T^* Increases with augment in Au nanoparticle size.

If hydrogen is responsible for the enhanced activity, then a transition from an active to a passive catalytic state ought to be an implication of the *loss* of the promoting factor (hydrogen) at T^* (T^*.for 10 nm nanoparticle 370°C; T^* for 15 nm nanoparticle 500°C). To check this, Au nanoparticles were heated to a temperature, $T \geq T^*$ and cooled to room temperature. A growth experiment was then carried out in the active growth range of the nanoparticles. This however, did not lead to any Si 1-D growth. Thus, confirming the absence of the growth-promoting factor.

If hydrogen is bonded to Au atoms in or on a nanoparticle, then the energy required to break the bonds will vary with size due to surface size effects. If one assumes a hydrogen *storage* and *release* mechanism then it is logical that smaller nanoparticles will *store* less hydrogen than larger ones. The *release* of hydrogen will consequently scale with size because smaller nanoparticles have more surface atoms with less coordination (section 2.2.1). For this reason, bonds at the surface are probably less stable, and require less energy to be weakened or broken. This is somehow analogous to the reasons behind the low melting point of small particles because melting relates to bond weakening.

Hydrogen is a very light element and difficult to detect. Several experiments were conducted in order to track the evolution of H_2 at T^* for 10 nm (370°C) and 15 nm (500°C) Au nanoparticles. A monitor of Au 4f core level photoelectron spectra from room temperature to 550°C reveal no considerable changes which can be attributed to a change in chemical state of the Au nanoparticles. UV-Vis absorption measurements on 15 nm Au nanoparticles before and after heat treatment do not reveal any observable changes in the optical properties of the Au nanoparticles. Thermal desorption spectroscopy (TDS) measurements up to 500°C, detect only hydrogen amounts comparable to the background which corresponds to less than 10^{-2} μg of H_2. XRD measurements were performed on a Au/α-Al_2O_3 before and after after annealing at 500°C. The lattice constant valuses obtained for 15 nm Au nanoparticles are 4.061 Å and 4.073 Å before and after heating respectively. This error range obtained from the peak fits (section 4.3.1) however falls within the referrence lattice constant value for bulk Au **(PDF)** card of Au (**4-784**) (FCC metallic gold).

Even though Si 1-D growth experiments show strong evidence of hydrogen enhanced catalytic activity, it has not been possible to physically detect the presence of a AuH_x compound. AuH_x is however known to be a stable anion[91]. This can be confirmed by the fact that Au nanoparticles treated in H_2 plasma are still active for Si 1-D growth after several weeks of exposure in ambient conditions.

4.4.3 Summary

Based on experimental observations, the low temperature catalytic activity of Au nanoparticles (with respect to Si 1-D growth) is observed in Au nanoparticles prepared in a H_2 plasma environment. Au nanoparticles of the same size prepared in an O_2 plasma environment do not promote Si 1-D growth at low temperatures. This effect is observed to be independent of the substrate used. There is a nanoparticle size dependent critical temperature, $T*$ at which the Au nanoparticles become passive. Once nanoparticles have been treated at $T*$, growth can no longer be archieved even if the nanoparticle is subjected to condition under which Si 1-D growth will normally occur. These factors strongly suggest the presence of H_2 in Au nanoparticles, which promotes low temperature growth of Si 1-D structures. However, due to device limitations, the presence of H_2 in Au nanoparticles prepared in H_2 plasma has not been possible to measure.

5 Synthesis of Other Materials

5.1 $F_{16}CuPc$ 1-D Growth from Au Nanoparticle Templates

(Dosch group collaboration, MPI- Stuttgart)

Interactions between atoms and molecules lead to bond formation, and different crystallographic arrangements in materials. Nanomaterials manifest properties, which fall between those of the bulk and atomic phase of the same elemental material. The smaller the nanomaterial, the more pronounced the atomic character becomes, in respect to quantization of energy levels, which greatly alter the electronic and optical properties of the material. One thus expects the sensitivity of a nanomaterial to minimal external forces and foreign elements to become enhanced with downscaling. To study the influence of external factors, and how these scale with size, one has to have reasonable hands-on control in tuning the size and external factor. This in turn enables a qualitative assessment of the threshold limits of size-induced effects on a system under study.

In this section, the interaction of small aromatic molecules with Au nanoparticles is probed. The influence of external factors such as Au nanoparticle size and temperature are taken into focus.

5.1.1 Motivation

The quest for low-cost, energy-saving and flexible electronics is currently dominating preferential semiconductor fabrication. On the other hand, technology is also being developed to suit the already well-established silicon technology. The mélange of organic-inorganic materials in technological development have opened a route to new materials and cheaper electronics. Organic semiconductors are less costly, easily processed into various forms (rigid or flexible) and their properties are controllable by molecular engineering. Among the different explored materials, small aromatic molecules have been recognized as promising candidates for future applications, because they can be grown in films of high crystalline order, thus fulfilling one of the important requirements to obtain high charge carrier mobility [cite]. However, although ordered organic films have been successfully implemented in electronic devices (such as OFETs or OLEDs), the controlled growth of organic low-dimensional architectures still remains a challenge.

This is in contrast with inorganic semiconductors whereby the controlled fabrication of inorganic 1-D semiconductors structures has opened new promising avenues for nanoscale device applications with novel material properties. In general, different synthetic strategies have been used to promote the crystallization of solid structures along one direction, for instance, by using templates of metal aggregates to catalyze their 1-D growth. This has been accomplished to create 1-D structures from semiconductor materials such as ZnO [92], GaN **[93]**, InP [94].

As favourable as organic semiconductors may be, most of them face major setbacks such as low thermal stability and easy contamination on exposure to air which drastically alters their electronic properties. Copper-hexadecafluorophthalocyanine ($F_{16}CuPc$) is a promising n-type organic semiconductor due to its air stability, high thermal and chemical stability as well as high charge mobility [95-97]. Its chemical formula is $C_{32}F_{16}N_8Cu$. Figure 5.1-1 is a schematic of the molecular structure of $F_{16}CuPc$ showing its dimensions.

Figure 5.1-1: Schematic representation of the molecular structure of $F_{16}CuPc$ (left) and its molecular dimensions (right).

Previous studies have compared the properties of F_{16}CuPc thin films, relating them to the crystalline structure and morphology of each substrate on which they are grown [98]. In particular, relating them to the molecule-molecule and molecule-substrate interactions in each case [99]. These studies indicate that while the packing of the molecules is similar in the layers deposited on the different substrates, the degree of order they present is highly influenced by the morphology and crystalline structure of each substrate. According to x-ray diffraction studies, the deposition of F_{16}CuPc on SiO_x substrates leads to molecules oriented in an upright manner **[100]**. Copper phthalocyanine (CuPc) molecules deposited on metal surfaces such as Au have been found to have orientations parallel to the substrate [101].

As an organic semiconductor, F_{16}CuPc has been chosen because it exhibits an intrinsically anisotropic growth, driven by the strong intermolecular coupling of π-electrons on adjacent molecules, which can be exploited to *direct* their one dimensional growth along one dimension. This anisotropy is usually reflected on a characteristic morphology of terraces or crystallites elongated along the packing direction of the co-facial stack [98]. With this approach it is expected that the Au nanoparticles assume the function of providing an energetically favor reaction site for nucleation and induce 1-D growth.

5.1.2 F_{16}Cu Pc 1-D Growth

Molecular beam epitaxy (MBE) is a thin film growth technique based on the reaction between a molecular or atomic beam and a substrate maintained at desired temperature (T_s) under UHV conditions. Oganic molecular beam expitaxy (OMBE) is an important advancement in the growth of high purity organic films in a highly controlled manner [101].

Si (100) wafers were cleaned and coated with gold nanoparticles as previously described. The size of the Au nanoparticles was then increased by an additional electroless deposition step [102]**.** The F_{16}CuPc molecules were deposited on Au nanoparticle arrays by vapour deposition in ultrahigh vacuum (1×10^{-9} mbar) at a low rate (~ 3 Å/min). To have an *in situ* monitor of the F_{16}CuPc coverage, the substrates employed exhibit the Au nanoparticle array only on one-half of the surface and have a smooth SiO_x surface on the other half. All samples discussed have a nominal $F_{16}CuPc$ coverage of 8-10 nm. Before growth, the Au nanopatterned surfaces were heated to 450°C under ultrahigh vacuum (UHV) conditions for 2 hours in order to desorb remnant impurities and contamination. Figure 5.1-2a is a general scheme of the growth of $F_{16}CuPc$ onto the Au nanoparticles. The SEM micrograph (figure 5.1-2b) is a 55° tilted view of the substrate at the boundary between the Au nanoparticle array and the bare SiO_x/Si substrate. The Au nanoparticles have diameters, D ~ 20 nm and lateral spacing, L of ~ 120 nm.

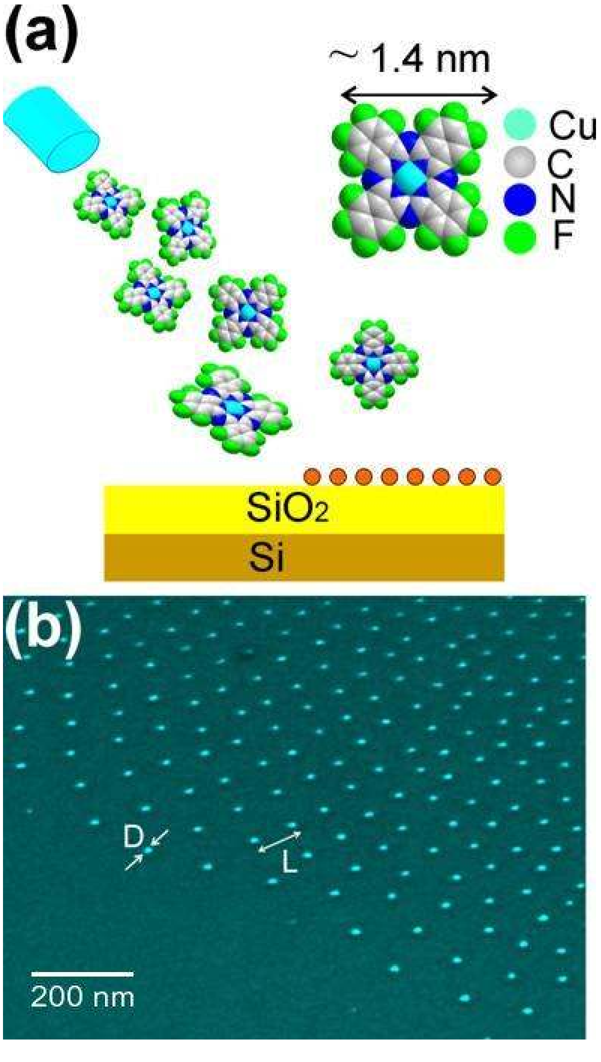

Figure 5.1-2: (a) General scheme of the growth of $F_{16}CuPc$ onto the template of gold nanoparticles. Half of the substrate is left uncovered as reference. (b) SEM image (55° tilt) of the substrate at the boundary between the nanoparticle array and the bare SiO2. The distance *L* between the gold nanoparticles and their size *D* are externally controlled parameters

Figure 5.1-3 shows SEM micrographs of the F_{16}CuPc morphology obtained on an uncoated area of a SiO_x surface. The F_{16}CuPc film illustrates the typical island like morphology obtained for the low surface coverage adopted here (120 Å). Thicker films lead to a smooth continuous film.

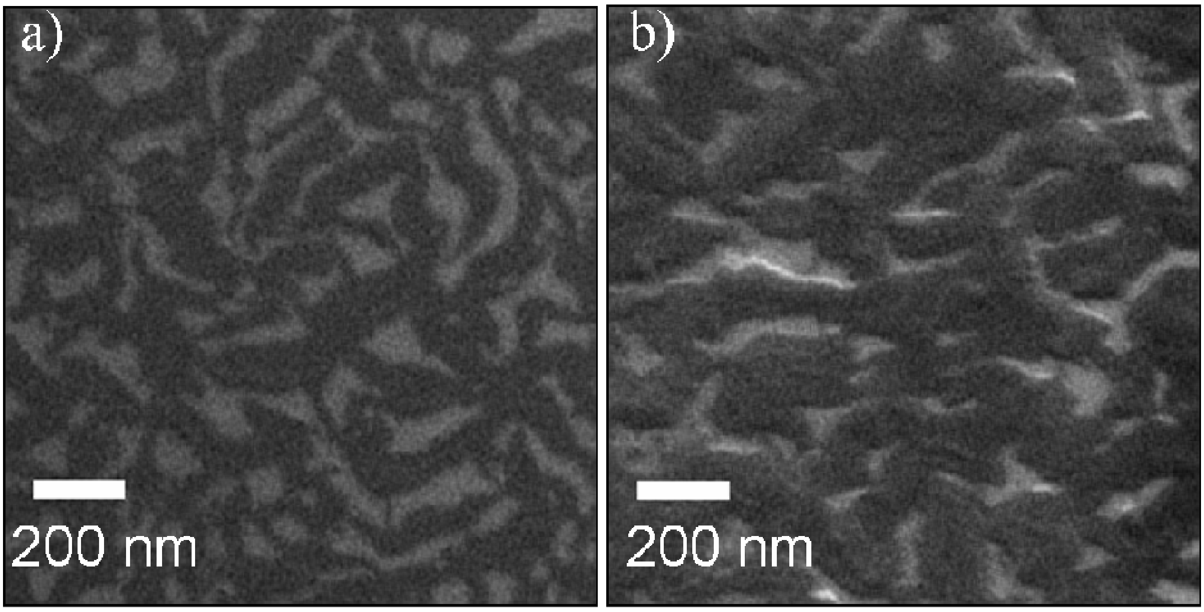

Figure 5.1-3: SEM micrographs showing a top (a) and tilted (b) view of a F_{16}CuPc thin film on a SiO_x surface

The resulting $F_{16}CuPc$ structures grown from Au nanoparticles are shown in the SEM micrograph in figure 5.1-4, which discloses $F_{16}CuPc$ 1-D nanostructures to possess a typical diameter of $d \sim 20$ nm, and grow standing on top of the Au nanoparticles (inset figure 5.1-4). Apparently, the Au nanoparticles act as nucleation sites for the $F_{16}CuPc$ molecules and promote their wire-like growth. These organic nanostructures are found to be stable after several weeks of storage in air.

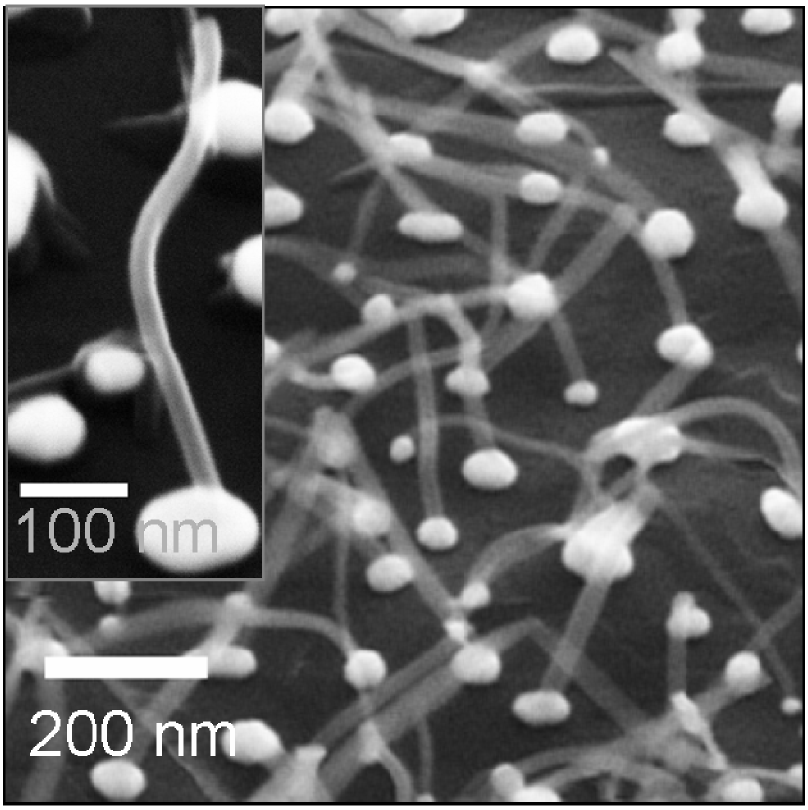

Figure 5.1-4: **FSEM image illustrating the vertical growth of 1-D $F_{16}CuPc$ wire-like nanostructures with widths ranging between 20-25 nm on top of Au nanoparticles and lengths up to ~ 300 nm. The inset is an SEM image of a vertically aligned $F_{16}CuPc$ 1-D structure ~ 20 nm in diameter on a 100 nm Au nanoparticle (tilt angle of 55° in both images).**

The high degree of selectivity of this Au nanoparticle-assisted 1-D growth is illustrated in figure 5.1-5a, which zooms in onto the boundary between the reference SiO_x surface and the gold nanoparticle array. As can be seen in a higher resolution SEM image in the inset in figure 5.1-5b (taken on another sample), uniform $F_{16}CuPc$ 1-D nanostructures connect the Au nanoparticles, thereby forming a network. This conduct is attributed to electrostatic forces between the Au nanoparticles and the organic structures, which are negatively charged by the electron beam. This would in fact imply, that applying an electric field between nanostructured Au electrodes could control the growth direction of a single 1-D F16CuPc structure. On the other hand, this charging effect renders the SEM observation of the standing F16CuPc 1-D structures rather difficult because these soft nanostructures bend towards the surface under the Coulomb force induced by the electron beam.

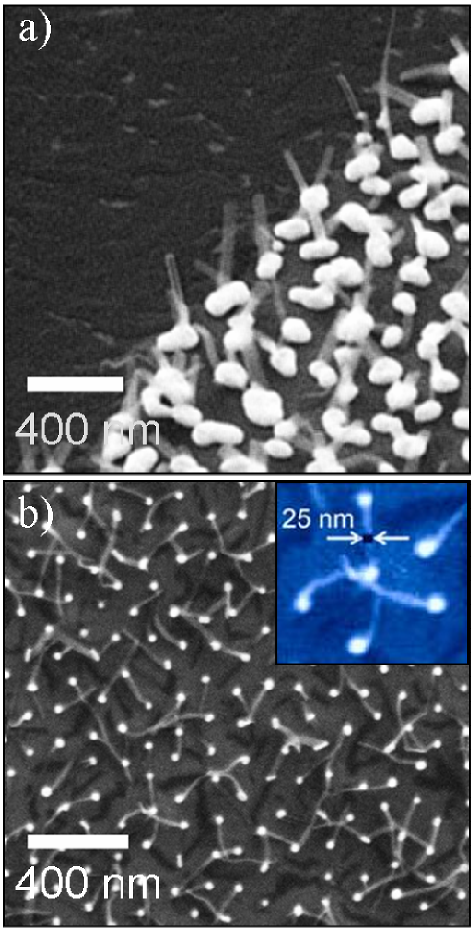

Figure 5.1-5: (a) SEM micrograph (45° tilt) taken at the boundary between the gold template and the SiO_2 showing the high selectivity of the 1-D $F_{16}CuPc$ growth. The Au nanoparticle lateral separation, L ~ 120 nm and the nanoparticle diameter varies between ~ 100-200 nm. (b) Typical SEM micrograph (top view) on another sample (mean Au nanoparticle size of D~30 nm and average distance of L ~150 nm) showing the network of $F_{16}CuPc$ 1-D nanostructures connecting nearby Au nanoparticles.

The distance, *L*, between the Au nanoparticles and their size, *D*, are externally controlled parameters. The former enables control of the packing density of the F_{16}CuPc 1-D structures. Interestingly, the F_{16}CuPc 1-D structures grow with a fixed diameter (*d* ~ 15-30 nm) regardless of the Au nanoparticle size *D* (see inset in figures 5.1-4 and 5.1-5b). The origin of the selection of this length scale is yet unclear. It is, however, in striking contrast to the formation of inorganic 1-D structures, which adopt a diameter dictated by the size of the metallic seed **[18].**

5.1.3 Effect of Au Nanoparticle Size

The effect of the Au nanoparticle size *D* on F_{16}CuPc growth is summarized in Figure 5.1-6

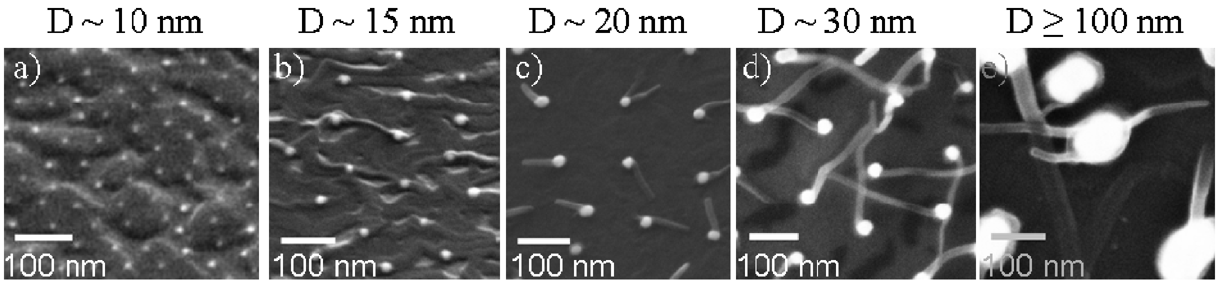

Figure 5.1-6: SEM images illustrating the influence of the Au particle size on F16CuPc 1-D growth. Single structures emerge from each Au particle when the size of the nanoparticle exceeds a critical linear dimension of *D = 20 nm. The width of the F16CuPc 1-D structures is independent of the Au nanoparticle size.**

Figure 5.1-6 shows the growth structures obtained from *D* = 10, 15, 20, 30, and >100 nm Au nanoparticles. Stunningly, the only a smooth thin film growth- like that seen bare SiO_x surfaces - was observed with sizes $D \leq 20$ nm, when deposition of F16CuPc was performed on Au nanoparticles templates (figure 5.1-6a-b). Apparently, there exists need for a critical particle size *D** to able to induce F_{16}CuPc 1-D growth. Single 1-D structures emerge (from each Au particle) when the nanoparticle size exceeds a critical linear dimension of *D**= 20 nm, which is in good compliance with the mean diameter of the F_{16}CuPc 1-D structures, implying that the 1-D growth is only possible when the nanoparticle size exceeds the intrinsic diameter of the F_{16}CuPc 1-D structures (figure 5.1-6c-e). It is also interesting to note that several of these structures grow on one Au nanoparticle for particles with diameters $D > 100$ nm (figure 5.1-6e).

5.1.4 Effect of temperature

The substrate temperature also plays a critical role for the growth of the 1-D F16CuPc structures. Figure 5.1-7 shows SEM micrographs for samples grown at different substrate temperatures. When F_{16}CuPc deposition is performed at room temperature (figure 5.1-7a), none or only very truncated 1-D structures (with maximum lengths of ~ 40 nm) are observed to grow from the Au nanoparticles. Higher substrate temperature promotes the growth of longer 1-D structures: lengths of about 300 and 800 nm are formed for growth at 120 °C (Figure 5.1-7b) and 140 °C (Figure 5.1-7c), respectively. At T~160 °C, 1-D growth is considerably hindered (Figure 5.1-7d) due to molecular desorption, which sets in at this temperature. The observed temperature-dependent morphology gives clear evidence that the 1-D growth of F_{16}CuPc on Au nanoparticles is a thermally activated process. The assembly of

-

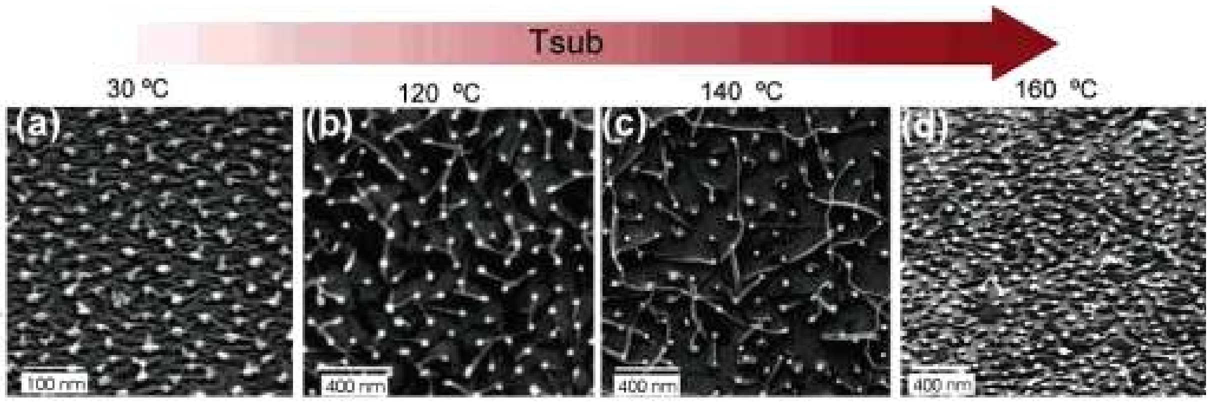

Figure 5.1-7: SEM images illustrating the influence of substrate temperature on F16CuPc 1-D growth. The optimal temperature is about 140°C.

Thermodynamic forces apparently govern F16CuPc in such uniform 1-D nanostructures, i.e., by the minimization of surface energies (resulting in 20 nm-width 1-D structures) together with kinetic parameters (nucleation at the Au nanoparticles is clearly mediated by surface and bulk diffusion). A preliminary cross-sectional transmission electron microscopy (TEM) study has been performed on one sample with $F_{16}CuPc$ 1-D structures, previously protected by a Pt capping layer and sectioned by focused ion beam (FIB). The cross-sectional TEM image (Figure 5.1-8) confirms the growth of standing or vertically oriented 1-D nanostructures. It can be appreciated that the 1-D structure stands perpendicular to one of the Au nanoparticle facets, tilted to about 25° with respect to the normal surface. This TEM study strongly suggests that the Au nanoparticle facets may play a decisive role in determining the growth direction and, possibly, the width of the resulting $F_{16}CuPc$ 1-D nanostructure (Figure 5.1-8). Unfortunately, the Pt layer, which acted as a protective layer during the FIB process, hindered the observation of the atomic structure of the gold nanoparticle and the identification of the facet. Further investigation is required to elucidate the mechanisms responsible for this novel growth and whether this is a general phenomenon observable for other metallic seeds and organic systems.

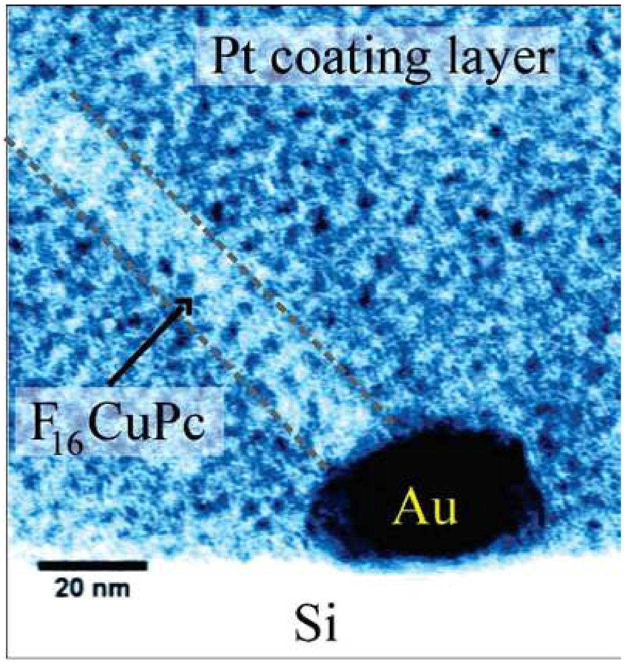

Figure 5.1-8: Cross-sectional TEM image from one of the samples. The TEM specimen has been prepared by low-current Ga ion-beam sectioning. A protective Pt capping layer is e-beam deposited in the FIB system prior to sectioning. The TEM image shows one F16CuPc 1-D structure standing perpendicular to one of the facets of the gold nanoparticle.

5.1.5 Summary

In conclusion, it has been demonstrated that it is possible to grow uniform F_{16}CuPc 1-D structures (diameter ~ 15-30 nm), whose precise localization and packing density, can be accomplished by templates of Au nanoparticles. Contrary to the situation vastly observed during inorganic semiconductor 1-D structure growth, the F_{16}CuPc 1-D structures do not adopt the diameter of the Au nanoparticle seed they grow from. Like inorganic 1-D synthesis, the lengths of the F_{16}CuPc 1-D structures increase with rise in synthesis temperature.

In conclusion, the above results show that this F_{16}CuPc 1-D structure growth strategy, which is technologically simple and inexpensive, is vastly applicable to other small aromatic molecules with strong intermolecular coupling between ð-orbitals. This provides exciting systems to test fundamental questions with respect to localization excitons and quantum transport in organic 1-D structures. The fact that the F_{16}CuPc 1-D structures assemble in a network connecting Au nanoparticles by the action of electrostatic forces suggests promising avenues for the bottom-up fabrication of integrated organic circuits.

5.2 Synthesis of nanoparticles of some 1st row transition metals

As mentioned in section 2.3, inorganic nanoparticles possess distinct properties, which differ from those of the bulk material of the same element. These properties include enhanced catalytic activity, lower melting point and changes in mechanical properties. First row transition metals are interesting due to their potential appliance in fields such as catalysis, sensors, and optoelectronic devices, just to name a few.

The ability of transition metals to form complexes makes them suitable candidates for micelle nanolithography. However, in practise, the incompatibilities between organic and inorganic systems render material synthesis in such hybrid systems rather tricky e.g. the poor solubility of inorganic salts in organic solvents.

The upcoming sections discuss the challenges encountered in these systems and how appropriate trade offs are found to strike the balance.

5.2.1 Platform for nanoparticle formation

The synthesis of nanoparticles requires the implementation of a precursor. which will induce nanoparticle formation. In section 2.4, the role of micelles as nanoparticle precursors has been discussed. A diblock copolymer, consisting of distinct hydrophilic and hydrophobic parts such as poly-styrene-block-2-vinyl-pyridiine (PS-b-P2VP) is used for the preparation of inverse micelles in the organic solvent, toluene. The polystyrene (PS) part is well solvated in toluene and surrounds the polar core of the micelle constituted of poly-2-vinyl-pyridine (P2VP). The metal ions coming from the metal precursor are selectively located in the polar core and most probably coordinated to the pyridine units.

As metal precursor, a salt should be chosen that is effectively taken up into the micelles. Due to the organic nature of the system, the metal counter-ion is also expected to play an important role. It should be:

- Hydrophobic in order to improve the solubility of the salt in the organic solvent
- Weakly coordinating, so that the metal ions can be effectively taken up in the pyridine core.

5.2.2 Nanoparticle extraction from mono-anionic compounds

Metal precursors with three different singly charged anions are considered: acetates (CH_3COO^-), chlorides (Cl^-) and nitrates (NO_3^-). Table 5.2-1 qualitatively summarises the anion characteristics, which are relevant to the synthetic system (micelles in toluene).

Anion	Coordination with metal ion	Solubility in organic solvents
(CH_3COO^-)	Yes	soluble
(Cl^-)	Yes	insoluble
(NO_3^-)	weakly	soluble

Table 5.2–1: Basic properties of single charged anions

The first row transition metals studied were Fe, Co, Ni, Cu and Zn. No nanoparticles could be observed on the surface after the plasma etch process when acetate precursors of first row transition metals (e.g. Fe and Zn) were used. Figure 5.2-1 is an SEM micrograph of a SiO_x/Si surface after a dip-coat process in a micelle solution loaded with Fe acetate $(Fe(CO_2CH_3)_2$. This surface is compared to that obtained when unloaded micelles are coated on a SiO_x/Si surface. In both cases, the surfaces appear mainly smooth. In conclusion, albeit the acetate salts being very soluble in the system, it is probable that the strong coordination of the CH_3COO^- anion prevents the efficient uptake of the metal ions into the P2VP core.

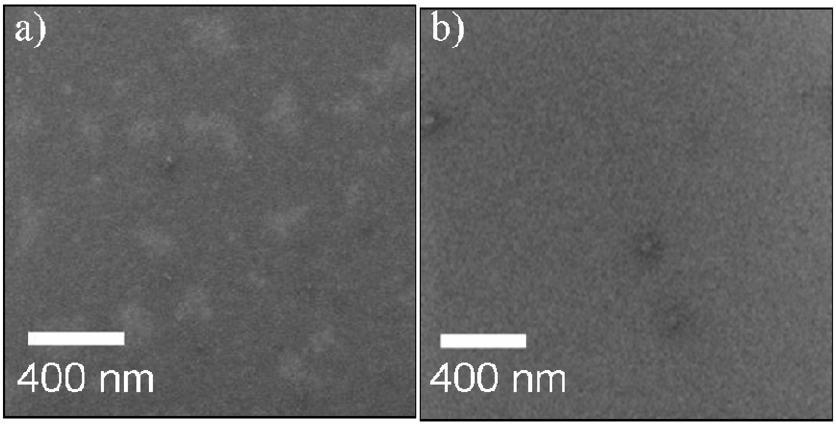

Figure 5.2-1: SEM micrographs of SiO_x/Si surfaces coated with unloaded micelles (left) and micelles in the presence of $Fe(CO_2CH_3)_2$

In the case of Cl^-, complex formation is observed after incorporation of the metal salt into the micelle solution. Figure 5.2-2a shows an SEM micrograph of micelles obtained after loading with $ZnCl_2$. The micelles are disorder and vary greatly in size (~ 10 – 30 nm). This behaviour was observed for the other elements except in the case of $FeCl_2$, which gave micelles in a better quasi hexagonal order (figure 5.2-2b).

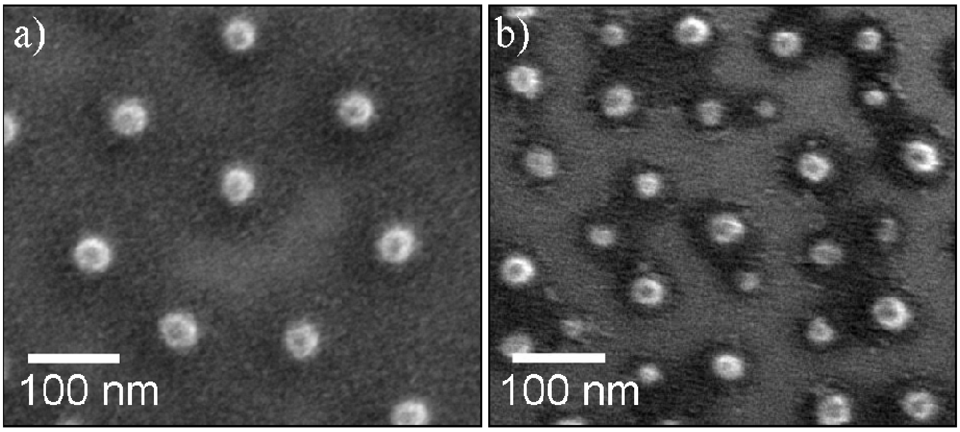

Figure 5.2-2: SEM micrographs of $FeCl_2$ (left) and $ZnCl_2$ (right) loaded micelles on a SiO_x/Si surface. The $ZnCl_2$ loaded micelles have sizes varying between 10 – 30 nm.

When NO_3^- anions were used, a good quasi hexagonal arrangement of the micelles was observed. This also led to nanoparticles arranged in the same manner after plasma treatment. The SEM micrographs (figure 5.2-.3) show SiO_x/Si surfaces after the plasma etch process with nanoparticles of the materials studied. The nanoparticle sizes range between 6 – 8 nm. The success of these nitrate metal salts is probably due to the weak coordinative nature of the NO_3^- anion.

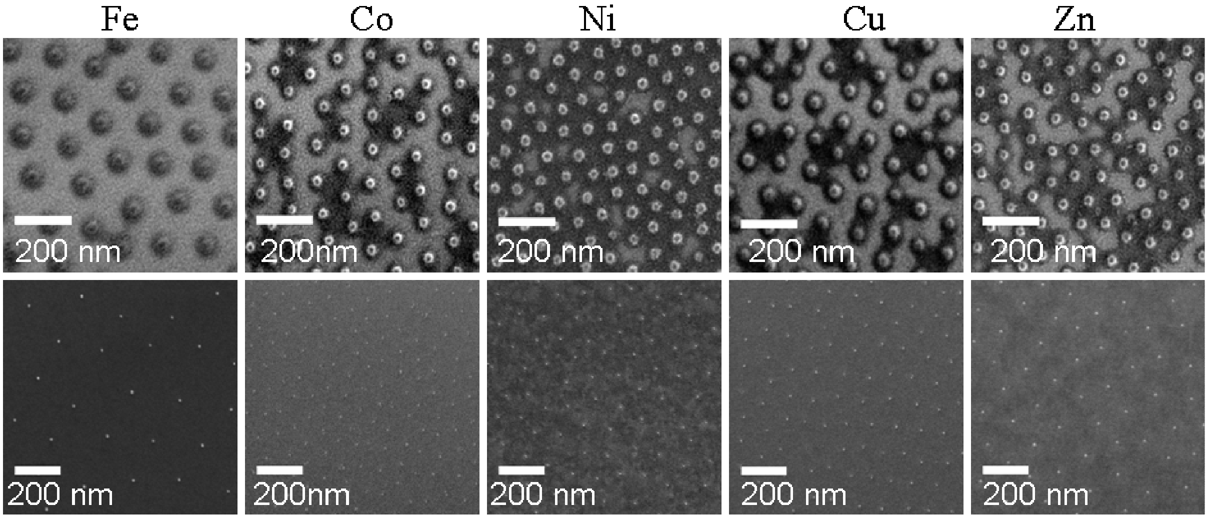

Figure 5.2-3: SEM micrographs of micelles loaded with Fe, Co, Ni, Cu and Zn nitrate compounds (top row) and the subsequent nanoparticles obtained after the plasma etch process (bottom row).

5.2.3 Summary

Fe, Co, Ni, Cu and Zn nanoparticles have been successfully synthesized from reverse micelles by implementing non-coordinating NO_3^- salts of the elements listed. The use of CH_3COO^- salts neither led to any observably micelle nor nanoparticle formation. Contrary to this, Cl^- salts led to visible micelle formation. However, the micelles were disordered and varied considerably in size (10 – 30 nm). It should be noted that these observations are not a generalisation over all first row transition elements but a survey of the compatibility of the metal precursors stated (5.2-1) with a P2VP core under the reaction conditions presented in section 3.1.1.

5.3 Highly Efficient Catalysts for Carbon Nanotube (CNT) Synthesis

Carbon nanotubes (CNTs) are allotropes of carbon. They can be considered as a prototype for 1-D nanotubes because of their relative simplicity, their unique properties, the vast information available on them, and their promise for practical applications [45]. There are in fact many types of CNTs, including single wall carbon nanotubes, double wall CNT, multi-wall CNTs, etc. A single wall CNT (SWCNT) is a one-atom thick sheet of graphite (called graphene) rolled up into a seamless cylinder with diameter of the order of a nanometer. Figure 5.3-1 shows schemes. Alongside SWCNTs, other distinct CNT structures with respect to the numbers of walls are; double-wall CNTs (DWNTs),and multi-wall CNTs (MWNTs). Other supramolecular assemblies have been demonstrated, such as CNTs packed with fullerenes (C60), so called “peapods” [103]. Typically, SWNTs are 0.4–5 nm in diameter, and MWNTs are up to 100 nm in diameter.

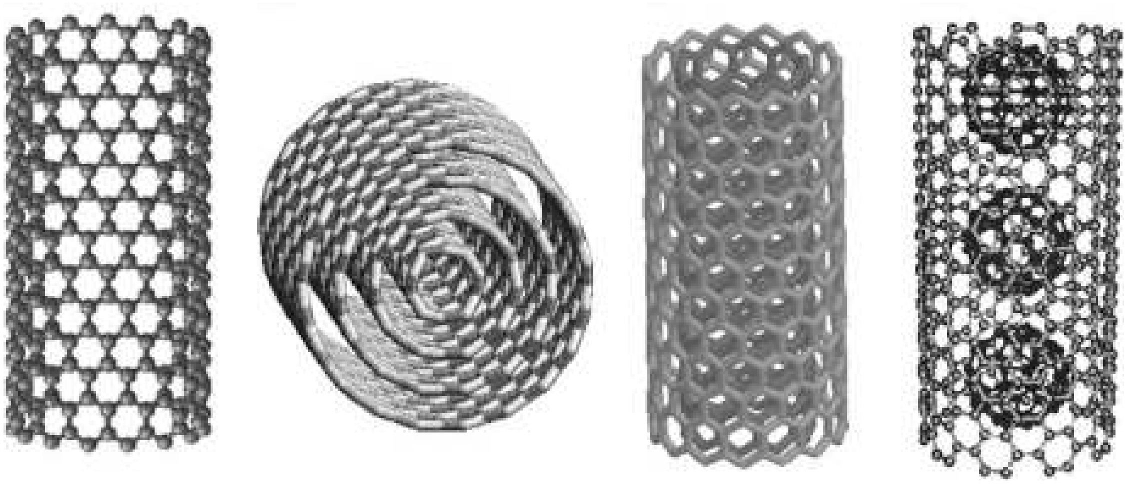

Figure 5.3-1: Schematic illustrations of basic CNT structures (from left to right): a single wall carbon nanotube (SWNT), a multi-wall carbon nanotube (MWNT), a double wall carbon nanotube (DWNT) and lastly a peapod nanotube consisting of a SWNT filled with fullerenes (e.g., C60) [103].

5.3.1 General Issues on CNT Growth

The synthesis of CNTs usually involves the use of metal catalysts from first row transition metals such as Fe, Co and Ni [104]. Other variants involve a mixture of these catalysts with other transition elements such as Molybdenum (Mo) [105]. Like inorganic 1-D structures, the diameter of CNTs is controlled by the size of the catalyst seed they grow from. The carbon source for CNT growth is usually a suitable hydrocarbon compound e.g. methane, acetylene, ethanol, etc. By controlling the catalyst composition, reactant chemistry, reaction temperature, and application of mechanical forces during growth, the properties of the resultant CNT can be reasonably tuned [104].

CNT growth can be performed via several synthesis routes such as arc discharge, hydrothermal, plasma enhanced CVD and catalytic CVD. Growth via the catalytic CVD process involves CNTs formation by organization of carbon on a metal nanoparticle catalyst in a high temperature hydrocarbon atmosphere. The carbon dissociates from the source compound and adds to the CNT through surface and/or bulk diffusion at the catalyst. Figure 5.3-2 is a schematic illustration of a CNT formation process at a metal catalyst seed.

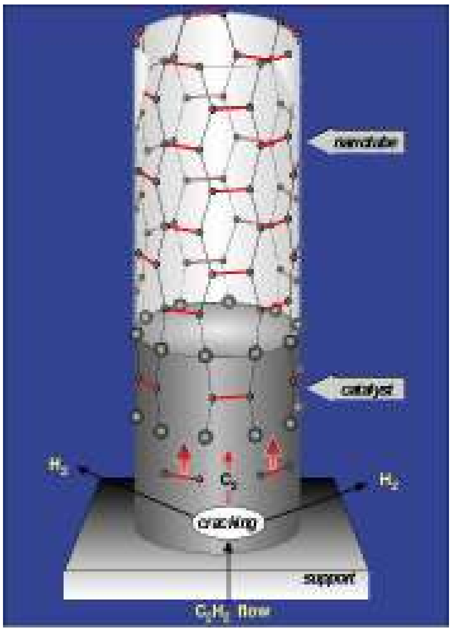

Figure 5.3-2: Schematic illustration of CNT formation at a catalyst nanoparticle site. Hydrocarbons are cracked at the catalytic site and the precipitated carbon grows into a nanotube.

5.3.2 Synthesis of CNTs from highly Efficient Metal Nanoparticle Catalysts

The synthesis of 1-D structures via CVD is usually encountered with the unpleasant effect of source material side deposition. This occurs when synthesis is performed at temperatures or conditions within which the source material is able to fragment without the aid of a catalyst. To minimize this process, synthesis should either be performed below the fragmentation temperature or a highly competitive or efficient catalyst should be employed.

One of the major flaws in CNT catalytic CVD synthesis is the durability of the catalysts employed during a growth process. For CNT growth to proceed and sustain, the interface (nanoparticle surface) between the nanoparticle and the precursor must be open to the elements. The coverage of this interface with soot or amorphous carbon halts the CNT growth process. This occurs when the non-catalytic deposition rate is competitive with or exceeds the catalytic deposition rate. This problem has been tackled to some extent by implementing oxidising agents such as water vapour in order to limit the quantity of amorphous carbon formed during a growth process. This procedure however, involves careful estimation of the oxidising agent because in excess, this would lead to incineration of the CNTs.

By aid of Co and Ni nanoparticles prepared by micelle nanolithography on SiO_x/Si substrates, CNTs have been grown under atmospheric pressure conditions in a quartz tube furnace at various temperatures and variable time scales. The precursor material was brought to the sample by bubbling argon (carrier gas) through ethanol at 40 sccm.

5.3.2.1 Size dependent Growth Rate of CNTs

Figure 5.3-3 shows CNTs grown at 850°C for 15 mins from Co nanoparticles. After 15 mins growth time, CNT structures are not observable on the main area of the surface with Co nanoparticles ~ 6 nm in diameter (figure 5.3-3a). Contrary to this situation, CNTs are observed, growing from ~ 20 nm, irregularly arranged Co nanoparticle clusters at the edge of

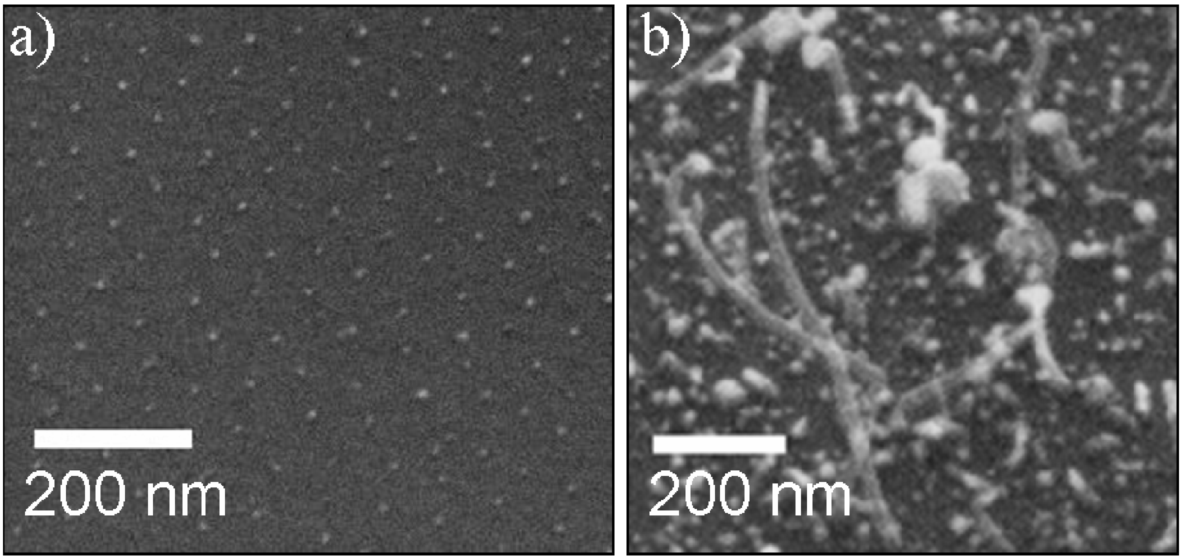

Figure 5.3-3: SEM micrographs (45° tilt) illustrating CNT growth after 15mins growth at 850°C on ~ 6 nm Co nanoparticles (a) and on larger clusters on the same sample (b). No CNT growth is observed on the 6 nm Co nanoparticles while CNTs with average diameters of 20 nm are observed at the sample edge where larger nanoparticle aggregates are situated.

the same sample (figure 5.3-3b). This is indicative of a more rapid CNT growth rate from larger nanoparticles – a situation similar to that observed for Si 1-D structures grown on SiO_x/Si substrates (section 4.2.1.1). Extending the growth time to 30 mins under the same growth conditions leads to CNTs with lengths ranging up to 20 µm (figure 5.3-4). The selectivity of the CNT growth process is illustrated in figure 5.3-4, which shows the boarder region between the patterned and unpatterned area of the SiO_x/Si surface. The inset shows a higher resolution SEM micrograph of the CNTs lying on the surface in an inter-twined manner. This is typically observed in CNT growth systems involving a relatively low density of catalyst material surface coverage. In such systems, external factors such as electric fields are used to vertically align CNTS. However, at high catalyst density and growth rate, vertically aligned CNT growth can be achieved due to Van der Waals interactions between dense neighbouring CNTs.

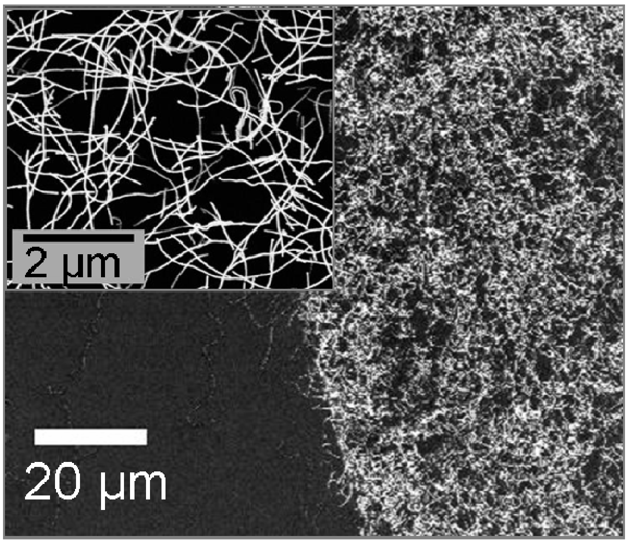

Figure 5.3-4: SEM micrograph (top view) of boarder between patterned and unpatterned area of a $Co/SiO_x/Si$ surface after CNT growth at 850°C for 30 mins. The CNTs are identified as bright white structures on the surface with lengths ranging up to 20 µm. The inset shows higher resolution SEM micrograph of inter-twined CNTs

5.3.2.2 Low temperature CNT growth under atmospheric pressure

When using thin metal films as catalysts for CNT growth, the film has to be transformed into fine particles. However, it is difficult to run this process at low temperatures. With the potential to synthesize predefined nanoparticles, micelle nanolithography can control size and site density. Hence, CNT growth temperature can be easily tuned because extra procedures such as etch gases (e.g. ammonia) usage, in order to reduce nanoparticle size, or and plasma conditions [16], in order to lower synthesis temperatures, can be dispensed with. Growth experiments on ~ 4 nm Ni nanoparticles at 450°C for 30 mins yields CNTs ~ 4 nm in diameter and lengths ranging up to 90 nm (figure 5.3-5). These are identifiable as white worm-like structures on the SiO_x/Si surface. Not all nanoparticles yield CNTs. Some of the nanoparticles are much smaller than those, which yield growth and may require much longer growth times to permit CNT growth.

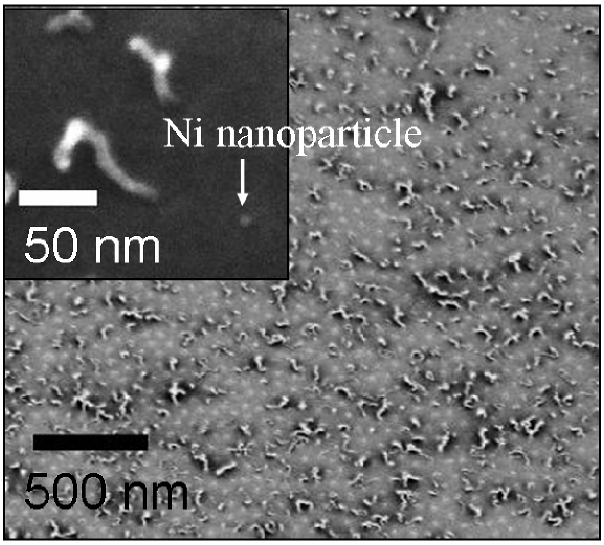

Figure 5.3-5: CNT growth from Ni nanoparticles at 450°C. Not all Ni nanoparticles yield CNTs. The inset shows a worm-like CNT with a diameter of ~ 5 nm and length of ~ 97 nm.

5.3.3 Summary & conclusion

In summary, CNTs have been successfully grown from Co and Ni Nanoparticles synthesized by diblock copolymer micelle nanolithography. Growth occurred via a catalytic CVD process under atmospheric pressure conditions. The growth rate of CNTs depends on the size of the nanoparticles and the synthesis temperature employed. The nanoparticles demonstrate catalytic efficiency over a broad range of temperatures (450 - 850°C).

Most CNT chemical vapour deposition growth processes are not very selective due to the side deposition of amorphous carbon, which gives the growth surfaces a black colour. For this reason, purification steps have to be performed to fish out clean CNTs from the soot [100]. Contrary to this situation, all samples reported here showed no colour changes observable by the naked eye before and after CNT growth. The visual presence of CNTs on the SiO_x/Si surfaces is confirmed by SEM analysis.

This approach is economical and of industrial interest because a relatively cheap carbon source (ethanol) is implemented in small amounts (< 5 ml) over several CNT growth experiments (~ 3 weeks). Also, the clean nature of the surface after growth is a primary indication that the CNTs grown are relatively clean.

6 General Summary & Closing Remarks

This work has illustrated that nanoparticles synthesized by micelle nanolithography show good thermal stability for Si 1-D growth processes and do not migrate on the surface at elevated temperatures. This is advantageous for applications such as field emission, where the position of a nanowire or nanotube is critical for the performance of the field emitting devices. The nanoparticles synthesized by the micelle nanolithography technique also show narrow size distribution, which enables the synthesis of Si 1-D structures with well-defined diameters.

The growth of small diameter Si 1-D structures ($d \leq 20$ nm) from Au nanoparticles proceeded via a chemical vapour deposition (CVD) route and growth was achieved at temperatures as low as 320°C. This rendered the process highly selective because growth was conducted at temperatures well below the thermal fragmentation temperature of silane (SiH_4), which is 420°C. This implies that molecular fragmentation was strictly performed by the nanoparticles. This limited side deposition of the source material which is a usual problem encountered in CVD processes. Low temperature synthesis has enabled the transfer of catalyst-mediated Si 1-D growth from expensive crystalline substrates to cheaper ones such as borosilicate glass. This is technologically relevant due to the fact that the transfer of electronics onto cheap substrates provides an alternative for the manufacture of cheaper electronic devices.

The nanoparticle/substrate interaction indicated the presence of a substrate-induced strain on the Au nanoparticles, which substantially influenced the resultant Si 1-D structures grown as well as their growth mode. The formation of Si nanowires (SiNWs) has been attributed to a dominant bulk diffusion of Si atoms into the interior parts of the Au nanoparticle. This results from an expansion of the substrates upon heating, which in turn exerts less compressive stress on the nanoparticles. This is demonstrated as a tip growth mode in the Si 1-D structures, which reflects a weakened interaction between the nanoparticles and the underlying substrate. This phenomenon is best illustrated in the case of the Au/glass system where a transition from a root to a tip growth mode is observed as the growth temperature is raised from 350°C to 420°C. Si 1-D structure growth on Si substrates also results in SiNWs due to the weak Au/Si interaction after the underlying SiO_x layer, initially supported the Au nanoparticle, is stripped off in a CF_4 plasma process.

When the substrate exerts a reasonable amount of stress on the Au nanoparticles such that, bulk diffusion of Si into the nanoparticle is considerably impeded, a surface diffusion mechanism is induced. This is reflected in the formation of Si nanotubes (SiNTs) up to a transitional temperature of 450°C, where a mixture of SiNWs and SiNTs is observed. This is attributed to non-uniform expansion of the amorphous SiO_x matrix within which the Au nanoparticle is partially embedded. Whereby, a relaxation at one location may lead to compression at another place on the SiO_x surface. The mixture of growth modes (tip and root) observed is due to the fact that the Au nanoparticles have different depths in the SiO_x matrix, which leads to variations in the magnitude of nanoparticle-substrate interactions for each Au nanoparticle. At 480°C, only SiNWs are obtained. This is assigned to an increase in diffusion rate with temperature increase as well as a further expansion of the SiO_x matrix, which reduces the substrate-induced stress imposed on the substrate.

At this juncture, it is worth mentioning that the sp^3 hybridized nature of Si renders its formation of tubular structures as would, sp^2 hybridized carbon, difficult [106]. This has rendered SiNT growth quite challenging. Nevertheless, the first real SiNTs were synthesized only recently by a self assembly technique at 470°C [17]. This work has provided an alternative route for SiNT growth by exploiting a substrate-induced stress mechanism to instigate Si surface diffusion on a Au nanoparticle and promote SiNT growth. The use of Au nanoparticles enables the precise control over the diameter of SiNTs – a parameter, which is not controlled in the SiNT hydrothermal synthesis process [17]. In addition, the synthesis temperatures used in this work are currently the lowest reported thus far.

Low temperature growth of Si 1-D structures was achieved by preparing the Au nanoparticles in a H_2 plasma environment prior to the growth process. No Si 1-D growth was observed when Au nanoparticles of the same size, prepared in an O_2 plasma environment, were subjected to conditions that normally yield growth for nanoparticles prepared in a H_2 plasma environment. This clearly indicated the strong dependency of Au nanoparticle performance on synthesis route. Au nanoparticles prepared in H_2 plasma indicated a critical temperature, *T**, at which Au nanoparticle activity showed a transition from a catalytically active to a passive state (with respect to Si 1-D growth). *T** was found to vary with size and the transition from catalytic to passive state occurred at 370°C and 500°C for ~ 10 nm and ~ 15 nm Au nanoparticles respectively. When *T** is has been attained or at temperatures beyond *T**, no growth can be achieved with the nanoparticles when conditions which normally would yield growth are re-applied. This gives insight to the fact that the passive state involves the *loss* of a promoting component from the Au nanoparticles, which is presumed to be H_2. Unfortunately, neither the evolution of H_2 at *T**, nor any changes in optical characteristics or electronic properties of the Au nanoparticles could be observed. However, all growth experiments point towards the fact that H_2 impurities promote low temperature catalytic activity in the Au nanoparticles during a Si 1-D growth process. More sensitive characterization techniques need to be sought in order to quantify the degree of H_2 impurity in the nanoparticles. The conclusion from all this is that nanoparticles of the same size, do not necessarily manifest the same properties. The choices of substrate and preparation route(s) play very decisive roles in determining the outcome of a Si 1-D growth process. The anomalies observed from Au nanoparticles during a Si 1-D growth process originate from all three factors – nanoparticle size, nanoparticle/ substrate interaction, impurities in nanoparticles, all which alter reaction kinetics.

The synthesis of an organic semiconductor 1-D structure ($F_{16}CuPc$) by organic molecular beam epitaxy (OMBE) revealed the importance of size control at nanoscale. It was observed that $F_{16}CuPc$ molecules formed 1-D structures on Au nanoparticles only at nanoparticle size, $D \geq 20$ nm, which corresponded to the average size of the $F_{16}CuPc$ 1-D structures. This indicated that the common presumption that nanoparticles dictate the diameter of 1-D structures, does not apply to the $F_{16}CuPc$ 1-D/Au nanoparticle system.

An advantage of micelle nanolithography lies in the fact that the technique can be extended to synthesize other nanoparticles other than Au. The synthesis of some first row transition metal catalysts such as Fe, Co, and Ni enabled the synthesis of carbon nanotubes (CNTs). The efficiency of the catalysts was illustrated in their activity throughout the time allocated to each growth procedure, which also led to CNTs with lengths ranging up to 20 μm. The substrate surfaces did not turn black after growth as is usually observed for most CNT growth processes. This gave preliminary insight on the clean nature of the CNTs.

In the course of working on this thesis, certain facts came to light:

- What is known to work for all, must not work for your system. Material properties vary based on the chosen synthetic route(s) as well as the instruments used to perform the synthesis.
- Judgment of a phenomenon can not be limited to its ability to be measured and subsequently assigned physical values. In other words, because it can not be *seen* does not mean it is not there.
- There are exceptions to every rule. Not all factors (e.g. diameter of organic 1-D structures) are controlled in the same way.
- Patience pays. Some processes just need more time (e.g. in the case of CNT synthesis).

7 Bibliography

1. Bai, J., et al., *Metallic single-walled silicon nanotubes.* Proceedings of the National Academy of Sciences of the United States of America, 2004. 101(9): p. 2664-2668.

2. Cavaleri, J.J., et al., *Femtosecond Study of the Size-Dependent Charge-Carrier Dynamics in Zno Nanocluster Solutions.* Journal of Chemical Physics, 1995. 103(13): p. 5378-5386.

3. Hill, N.A. and K.B. Whaley, *Size Dependence of Excitons in Silicon Nanocrystals.* Physical Review Letters, 1995. 75(6): p. 1130-1133.

4. Liu, H.J., et al., *Electronic structure of ensembles of gold nanoparticles: Size and proximity effects.* Physical Review B, 2005. 72(15): p. -.

5. Ma, D.D.D., S.T. Lee, and J. Shinar, *Strong polarization-dependent photoluminescence from silicon nanowire fibers.* Applied Physics Letters, 2005. 87(3): p. -.

6. Wan, Q., et al., *Room-temperature hydrogen storage characteristics of ZnO nanowires.* Applied Physics Letters, 2004. 84(1): p. 124-126.

7. Cui, Y., et al., *Doping and electrical transport in silicon nanowires.* Journal of Physical Chemistry B, 2000. 104(22): p. 5213-5216.

8. HAISHENG RONG, J.R., ANSHENG LIU; COHEN Oded, KUO Ying-Hao, PANICCIA Mario, Kubby Joel A, Reed Graham T. *Silicon based laser, amplifier, and wavelength converter for optoelectronic integration*. in *Proceedings of SPIE, the International Society for Optical Engineering (Proc. SPIE Int. Soc. Opt. Eng.)*. 2006.

9. She, J.C., et al., *Field electron emission of Si nanotips with apexes of various compositions.* Applied Physics Letters, 2005. 87(5): p. -.

10. Peng, K.Q., et al., *Aligned single-crystalline Si nanowire arrays for photovoltaic applications.* Small, 2005. 1(11): p. 1062-1067.

11. Nagesha, D.K., M.A. Whitehead, and J.L. Coffer, *Biorelevant calcification and non-cytotoxic behavior in silicon nanowires.* Advanced Materials, 2005. 17(7): p. 921-+.

12. Hanrath, T. and B.A. Korgel, *Supercritical fluid-liquid-solid (SFLS) synthesis of Si and Ge nanowires seeded by colloidal metal nanocrystals.* Advanced Materials, 2003. 15(5): p. 437-440.

13. Holmes, J.D., et al., *Control of thickness and orientation of solution-grown silicon nanowires.* Science, 2000. 287(5457): p. 1471-1473.

14. Schmidt, V., S. Senz, and U. Gosele, *UHV chemical vapour deposition of silicon nanowires.* Zeitschrift Fur Metallkunde, 2005. 96(5): p. 427-428.

15. Wang, Y.W., et al., *Epitaxial growth of silicon nanowires using an aluminium catalyst.* Nature Nanotechnology, 2006. 1(3): p. 186-189.

16. Hofmann, S., et al., *Controlled low-temperature growth of carbon nanofibres by plasma deposition.* New Journal of Physics, 2003. 5: p. -.

17. Tang, Y.H., et al., *Self-assembled silicon nanotubes under supercritically hydrothermal conditions.* Physical Review Letters, 2005. 95(11): p. -.

18. Yi Cui, X.D., Jiangtao Hu, and Charles M. Lieber, *Diameter-controlled synthesis of single-crystal silicon nanowires.* APPLIED PHYSICS LETTERS VOLUME, 2001. 78 (22): p. 2214-2216.

19. McAlpine, M.C., et al., *High-performance nanowire electronics and photonics on glass and plastic substrates.* Nano Letters, 2003. 3(11): p. 1531-1535.

20. McAlpine, M.C., R.S. Friedman, and D.M. Lieber, *Nanoimprint lithography for hybrid plastic electronics.* Nano Letters, 2003. 3(4): p. 443-445.

21. Castro, T., et al., *Size-Dependent Melting Temperature of Individual Nanometer-Sized Metallic Clusters.* Physical Review B, 1990. 42(13): p. 8548-8556.

22. Pardo-Yissar, V., et al., *Acetylcholine esterase-labeled US nanoparticles on electrodes: Photoelectrochemical sensing of the enzyme inhibitors.* Journal of the American Chemical Society, 2003. 125(3): p. 622-623.

23. Schubert, M.M., et al., *CO oxidation over supported gold catalysts-"inert" and "active" support materials and their role for the oxygen supply during reaction.* Journal of Catalysis, 2001. 197(1): p. 113-122.

24. Hannon, J.B., et al., *The influence of the surface migration of gold on the growth of silicon nanowires.* Nature, 2006. 440(7080): p. 69-71.

25. Mendes, P.M., et al., *Nanostructures from nanoparticles.* Journal of Physics-Condensed Matter, 2003. 15(42): p. S3047-S3063.

26. Niwa, D., et al., *Formation of micro and nanoscale patterns of monolayer templates for position selective immobilization of oligonucleotide using ultraviolet and electron beam lithography.* Chemistry Letters, 2004. 33(2): p. 176-177.

27. Angelopoulos, M., *Conducting polymers in microelectronics.* Ibm Journal of Research and Development, 2001. 45(1): p. 57-75.

28. Broers, A.N.H., A. C. F.; Ryan, J. M., *Electron beam lithography-Resolution limits.* Microelectronic Engineering, 1996. 32: p. 1-4.

29. Dobisz, E.A., et al., *Electroless metal discharge layers for electron beam lithography.* Applied Physics Letters, 2003. 82(3): p. 478-480.

30. Medeiros, D.R., et al., *Recent progress in electron-beam a resists for advanced mask-making.* Ibm Journal of Research and Development, 2001. 45(5): p. 639-650.

31. **Xia, Y.N., et al., *Unconventional methods for fabricating and patterning nanostructures.* Chemical Reviews, 1999. 99(7): p. 1823-1848.**

32. **Lammertink, R.G.H., et al., *Nanostructured thin films of organic-organometallic block copolymers: One-step lithography with poly(ferrocenylsilanes) by reactive ion etching.* Advanced Materials, 2000. 12(2): p. 98-103.**

33. **Zhang, H., et al., *Biofunctionalized nanoarrays of inorganic structures prepared by dip-pen nanolithography.* Nanotechnology, 2003. 14(10): p. 1113-1117.**

34. **Polymers on nano periodic, h.s., *Polymers on nano periodic, heterogeneous surfaces.* Phys. Rev. Lett., 1999. 82: p. 2602.**

35. **Morkved, T.L., et al., *Local control of microdomain orientation in diblock copolymer thin films with electric fields.* Science, 1996. 273(5277): p. 931-933.**

36. **Boltau M, W.S., Mlynek J, Krausch G and and S. U, *Surface-inducedstructure formationof polymer blends onpatternedsubstrates.* Nature, 1998. 391: p. 877.**

37. **Spatz, J.P., *Nano- and micropatterning by organic - Inorganic templating of hierarchical self-assembled structures.* Angewandte Chemie-International Edition, 2002. 41(18): p. 3359-3362.**

38. **Alivisatos, P., *Self-assembly of nanoparticles into structured spherical and network aggregates.* Adv. Mater., 1998. 10: p. 131.**

39. **Ryan, J.M., *Invited Review Nanoscale devices fabricated by dynamic ploughing with an atomic force microscope.* Microelectron. Eng., 1996. 32: p. 131.**

40. **Glass, R., et al., *Micro-nanostructured interfaces fabricated by the use of inorganic block copolymer micellar monolayers as negative resist for electron-beam lithography.* Advanced Functional Materials, 2003. 13(7): p. 569-575.**

41. **Cavalcanti-Adam, E.A., et al., *Lateral spacing of integrin ligands influences cell spreading and focal adhesion assembly.* European Journal of Cell Biology, 2006. 85(3-4): p. 219-224.**

42. **Walter, N., et al., *Cellular unbinding forces of initial adhesion processes on nanopatterned surfaces probed with magnetic tweezers.* Nano Letters, 2006. 6(3): p. 398-402.**

43. **Glass, R., M. Moller, and J.P. Spatz, *Block copolymer micelle nanolithography.* Nanotechnology, 2003. 14(10): p. 1153-1160.**

44. **S. V. Gräter, J.H., N. Perschmann, M. Lopez-Garcia, H. Kessler, J. Ding, J. P. Spatz, *Mimicking Cellular Environments by Nanostructured Soft Interfaces.* Nano Lett., in press., 2007. 7(5): p. 14413.**

45. **R.(Riichiro) Saito, G.D., MS Dresselhaus, *Physical properties of carbon nanotubes***

-. 1998: Imperial College Press.

46. Davis, R.J., *All that Glitters is not Au°.* Science. 301(no. 5635): p. 926 - 927.

47. http://www.geo.ucalgary.ca/~tmenard/crystal/metalstatic.html.

48. http://hyperphysics.phy-astr.gsu.edu/hbase/solids/sili2.html.

49. H., O. and M. T.B., *Binary Alloy Phase Diagrams, Second Edition, Ed. T.B. Massalski, ASM.* 1990: p. 428-431.

50. Roduner, E., *Nanoscopic Materials: Size Dependent Phenomena.* 2006.

51. Last, I. and J. Jortner, *Nuclear fusion induced by Coulomb explosion of heteronuclear clusters.* Physical Review Letters, 2001. 8703(3): p. -.

52. Berry, R.S., *Phase transitions of small systems, in Theory of Atomic and molecular clusters, ed. J. Jellinek.* 1999.

53. Buffat, P. and J.P. Borel, *Size Effect on Melting Temperature of Gold Particles.* Physical Review A, 1976. 13(6): p. 2287-2298.

54. Hammer, B. and J.K. Norskov, *Why Gold Is the Noblest of All the Metals.* Nature, 1995. 376(6537): p. 238-240.

55. Lopez, N., et al., *On the origin of the catalytic activity of gold nanoparticles for low-temperature CO oxidation.* Journal of Catalysis, 2004. 223(1): p. 232-235.

56. Schmidt, V., S. Senz, and U. Gosele, *Diameter-dependent growth direction of epitaxial silicon nanowires.* Nano Letters, 2005. 5(5): p. 931-935.

57. Wang, C.X., M. Hirano, and H. Hosono, *Origin of diameter-dependent growth direction of silicon nanowires.* Nano Letters, 2006. 6(7): p. 1552-1555.

58. Delley, B. and E.F. Steigmeier, *Size Dependence of Band-Gaps in Silicon Nanostructures.* Applied Physics Letters, 1995. 67(16): p. 2370-2372.

59. Sergeev, G.B., *Nanochemistry.* Vol. 2006 Elsevier B. V. All rights reserved.

60. Glass, R., et al., *Block copolymer micelle nanolithography on non-conductive substrates.* New Journal of Physics, 2004. 6: p. -.

61. Spatz, J.P., et al., *Micellar inorganic-polymer hybrid systems - A tool for nanolithography.* Advanced Materials, 1999. 11(2): p. 149-153.

62. http://www.unl.edu/CMRAcfem/interact.htm.

63. http://www.chem.qmul.ac.uk/surfaces/scc/scat5_3.htm.

64. http://en.wikipedia.org/wiki/X-ray_photoelectron_spectroscopy.

65. **D Briggs, M.S., *Surface Analysis*. 1990.**

66. **Strecker, A., et al., *Progress in the preparation of cross-sectional TEM specimens by ion-beam thinning.* Zeitschrift Fur Metallkunde, 2003. 94(3): p. 290-297.**

67. ***IUPAC Compendium of Chemical Terminology*. 1997.**

68. **Girard, P.c.D.P.**

69. **Soh, M.T.K., J.H. Thomas, and J.J. TaIghader, *Thermally induced structural changes in nanoporous silicon dioxide from x-ray photoelectron spectroscopy.* Journal of Vacuum Science & Technology A, 2006. 24(6): p. 2147-2150.**

70. **Sarkar, D.K., et al., *XPS studies on silicide formation in ion beam irradiated Au/Si system.* Applied Surface Science, 1997. 120(1-2): p. 159-164.**

71. **Paparazzo, E., *The XPS analysis of Si-OH groups at the surface of silica.* Surface and Interface Analysis, 1996. 24(10): p. 729-730.**

72. **Mason, M.G., *Electronic-Structure of Supported Small Metal-Clusters.* Physical Review B, 1983. 27(2): p. 748-762.**

73. **Citrin, P.H., G.K. Wertheim, and Y. Baer, *Core-Level Binding-Energy and Density of States from Surface Atoms of Gold.* Physical Review Letters, 1978. 41(20): p. 1425-1428.**

74. **Fisher, D.J., *Diffusion in Silicon - A Seven Year Retrospective.* Defect and Diffusion Forum, 2005. 241: p. 218.**

75. **Schubert, L., et al., *Silicon nanowhiskers grown on < 111 > Si substrates by molecular-beam epitaxy.* Applied Physics Letters, 2004. 84(24): p. 4968-4970.**

76. **Fuhrmann, B., et al., *Ordered arrays of silicon nanowires produced by nanosphere lithography and molecular beam epitaxy.* Nano Letters, 2005. 5(12): p. 2524-2527.**

77. **Westwater, J., et al., *Growth of silicon nanowires via gold/silane vapor-liquid-solid reaction.* Journal of Vacuum Science & Technology B, 1997. 15(3): p. 554-557.**

78. **Lee, S.T., N. Wang, and C.S. Lee, *Semiconductor nanowires: synthesis, structure and properties.* Materials Science and Engineering a-Structural Materials Properties Microstructure and Processing, 2000. 286(1): p. 16-23.**

79. **Yao, Y., F.H. Li, and S.T. Lee, *Oriented silicon nanowires on silicon substrates from oxide-assisted growth and gold catalysts.* Chemical Physics Letters, 2005. 406(4-6): p. 381-385.**

80. **Tilke, A.T., et al., *Quantum interference in a one-dimensional silicon nanowire.* Physical Review B, 2003. 68(7): p. -.**

81. **BenChorin, M., et al., *Influence of quantum confinement on the critical points of the band structure of Si.* Physical Review Letters, 1996. 77(4): p. 763-766.**

82. Xing, Y.J., et al., *Growth of silicon nanowires by heating Si substrate.* Chinese Physics Letters, 2002. 19(2): p. 240-242.

83. Lu, J.Q. and S.S. Yi, *Uniformly sized gold nanoparticles derived from PS-b-P2VP block copolymer templates for the controllable synthesis of Si nanowires.* Langmuir, 2006. 22(9): p. 3951-3954.

84. Kikkawa, J., Y. Ohno, and S. Takeda, *Growth rate of silicon nanowires.* Applied Physics Letters, 2005. 86(12): p. -.

85. Cammarata, R.C., *Surface and interface stress effects on the growth of thin films.* Journal of Electronic Materials, 1997. 26(9): p. 966-968.

86. Cammarata, R.C., *Surface and Interface Stress Effects in Thin-Films.* Progress in Surface Science, 1994. 46(1): p. 1-38.

87. Floro, J.A., *Physical origins of intrinsic stress in volumer-weber thin films.* MRS Bulletin. 27(1): p. 19.

88. Bochkarev, A. and P. Deforcrand, *Nonperturbative Evaluation of the Diffusion Rate in Field-Theory at High-Temperatures.* Physical Review D, 1993. 47(8): p. 3476-3486.

89. Boyen, H.G., et al., *Oxidation-resistant gold-55 clusters.* Science, 2002. 297(5586): p. 1533-1536.

90. Virojanadara, C. and L.I. Johansson, *Photoemission study of Si-rich 4H-SiC surfaces and initial SiO2/SiC interface formation.* Physical Review B, 2005. 71(19): p. -.

91. Wang, X.F. and L. Andrews, *Gold is noble but gold hydride anions are stable.* Angewandte Chemie-International Edition, 2003. 42(42): p. 5201-5206.

92. Haupt, M., et al., *Ultraviolet-emitting ZnO nanowhiskers prepared by a vapor transport process on prestructured surfaces with self-assembled polymers.* Journal of Applied Physics, 2003. 93(10): p. 6252-6257.

93. Seryogin, G., et al., *Catalytic hydride vapour phase epitaxy growth of GaN nanowires.* Nanotechnology, 2005. 16(10): p. 2342-2345.

94. Mattila, M., et al., *Crystal-structure-dependent photoluminescence from InP nanowires.* Nanotechnology, 2006. 17(6): p. 1580-1583.

95. Dimitrakopoulos, C.D. and P.R.L. Malenfant, *Organic thin film transistors for large area electronics.* Advanced Materials, 2002. 14(2): p. 99-+.

96. Forrest, S.R., *The path to ubiquitous and low-cost organic electronic appliances on plastic.* Nature, 2004. 428(6986): p. 911-918.

97. de Boer, R.W.I., et al., *Influence of the gate leakage current on the stability of organic single-crystal field-effect transistors.* Applied Physics Letters, 2005. 86(3): p. -.

98. Oteyza, D.G.d., *Controlled enhancement of the electron field-effect mobility of F16CuPc thin-film*

transistors by use of functionalized SiO2 substrate. Applied physics Letters, 2005. 87: p. 183504-183507.

99. Osso, J.O., et al., *Controlled molecular alignment in phthalocyanine thin films on stepped sapphire surfaces.* Advanced Functional Materials, 2002. 12(6-7): p. 455-460.

100. de Oteyza, D.G., et al., *Structural rearrangements during the initial growth stages of organic thin films of F16CuPc on SiO2.* Journal of Physical Chemistry B, 2006. 110(33): p. 16618-16623.

101. Tokito, S., J. Sakata, and Y. Taga, *The Molecular-Orientation in Copper Phthalocyanine Thin-Films Deposited on Metal-Film Surfaces.* Thin Solid Films, 1995. 256(1-2): p. 182-185.

102. Private communication by T. Lohmu¨ller & J. P. Spatz, *Private communication by T. Lohmüller & J. P. Spatz*: Max-Planck-

Institut fu¨r Metallforschung and University of Heidelberg, Biophysical

Chemistry, Institute for Physical Chemistry, Heidelberg, Germany.

103. Dresselhaus, M.S., et al., *Nanowires and nanotubes.* Materials Science & Engineering C-Biomimetic and Supramolecular Systems, 2003. 23(1-2): p. 129-140.

104. Meyyappan, M., et al., *Carbon nanotube growth by PECVD: a review.* Plasma Sources Science & Technology, 2003. 12(2): p. 205-216.

105. Christen, H.M., et al., *Rapid growth of long, vertically aligned carbon nanotubes through efficient catalyst optimization using metal film gradients.* Nano Letters, 2004. 4(10): p. 1939-1942.

106. Perepichka, D.F. and F. Rosei, *Silicon nanotubes.* Small, 2006. 2(1): p. 22-25.

ACKNOWLEDGEMENTS

I would first of all like to thank Prof Joachim P. Spatz for granting me the opportunity to explore the world of nanotechnology and all the experience and courage I acquried while working with him. I have gained a great deal of knowledge during this PhD era. My sincere gratitude.

Many thanks to those of the STEM centre: Dr. Peter A. Van Aken for always taking time off to attend to any problems I had and for all I learned from our conversations. Peter Kopold, Kersten Hahn, for performing most of the TEM measurements illustrated in this work. Marion Kelsch and Maria Sycha for their dedication and understanding my special requests as concerns Tem sample preperation. I thank all members of the STEM department for thier patience and understanding whenever I needed them to attend to my multiple requests. I am most grateful.

I want to thank Prof. S. Hofmann, Dr. Lars P. H. Jeurgens, Dr. Chariya Virojanadara and Dr. G Richter for all they have taught me in surface science and for taking time to introduc me to all I need to know. I am very grateful for the lengthy periods they took to run XPS and UPS measurements with and for me. Their patience and kindness showed no boundaries. I also thank Dr. G. Richter for his guidance during the early stages of my PhD as well as performing HRTEM measurements on some of my samples. I would also like to thank Dr. U. Welzel and G. Maier for thier assistance in XRD measurements as well as qualitative and quantitaive discussions.

At this juncture, I would like to thank Prof. H. Dosch, Dr. E. Barrena and Xuena Zhang for the knowledge exchanged during our collaboration. I would also like to thank Dr. Hefin Griffiths of Oxford Instruments Plasma Tech. for the Si 1-D material growth experiments he performed in my absence. It was a great pleasure working with him while I visited Yatton.

Coming to the Spatz group. I must say i never got to experience such diversity. Each member is special in their own way. Like the shoulder next to you just when you feel your strength is down. I thank all members of the Spatz group. Special thanks to Linda, Petra, Irina, Raquel, Nikki, Roberto, Simon, Ralf, Ralf, Alex, Sylvie, Magnus, Carlos, Iain, Tobias, francesca, Ada and Philippe for bieng there. You can never imagine how much your presence has given me strength physically and spiritually. Furthermore, I want to express my gratitude to Dr. G Majer for the time he always dedicated in discussing at length with me to seek solutions to experimental problems.

To Prof. Wilfred Ngwa and Lydia Ngwa for thier prayers, constant encouragement all along. To Wadinga, Tsi, Beckeny, Kenneth, Kathleen, Nike, Bei, Anyoh, and Jerry for bieng the patient and understanding friends they are.

I have recieved bountiful amounts of support from Yu. You offered a great deal of understanding, and unlimited support. I lack the words to express my gratitude. I thank you endlessly. ☺

I owe much gratitude to so many people. Certain things in life are made easier when shared. I thank my family (*Daddy, Mama, Tah, Obe, Papa, YU, boo baby Tata* :-D) My sisters-in-law *(Baba and Angel*), my entire family for bieng there and giving me strength in all I do. For thier love and prayers. My little nephew and nieces, whose smiles in pictures and on the webcam cheer me up from miles away. Most of all for believing in me. Thank you. I love you all.

APPENDIX

Table of Figures

Tables